



*Technical University of Crete*

*School of Production Engineering and Management*

---

# **Numerical simulation of the flow field inside a one and a half turbine stage**

---

By

**Georgios Manos**

A dissertation submitted in partial fulfilment of the  
requirements for the degree of

*Master of Science*

**Supervisor**

Prof. Ioannis K. Nikolos

**Chania, July 2019**

Copyright © Georgios Manos, 2019.

All rights reserved.



*Technical University of Crete*

*School of Production Engineering and Management*

---

# **Numerical simulation of the flow field inside a one and a half turbine stage**

---

**By**

**Georgios Manos**

Approved by:

Dr. Ioannis K. Nikolos

Professor

Technical University of Crete,  
School of Production Engineering  
& Management

---

Dr. Anargiros Delis

Associate Professor

Technical University of Crete,  
School of Production Engineering  
& Management

---

Dr. Michail Konsolakis

Associate Professor

Technical University of Crete,  
School of Production Engineering  
& Management

---

*Chania, July 2019*

***“Intentionally Left Blank”***



## Acknowledgements

*I would like to thank my family and my supervisor, Professor I.K. Nikolos for their continuous support throughout the completion of this work.*

*Georgios Manos*

***“Intentionally Left Blank”***

## Abstract

The goal of the present thesis is to simulate a one and a half stage of a modern gas turbine, calculate performance parameters and validate said simulation through a normality check of these parameters, with the use of existing literature. The simulated one and a half turbine stage can then serve as a testbed for further investigation of turbomachinery related phenomena, such as erosion. It can also be used as a starting point in order to investigate off-design situations, such as transient phenomena, chocking, etc.

To achieve said goal, the steps taken are the following:

- Geometry measurements of existing rotor blades and stator vanes, in order to achieve adequate data for the drawing process. Other known engine parameters (for existing engine) were used to aid in the understanding of the operating conditions of the examined turbine.
- Construction of 3D drawing of the blades with the use of a CAD software.
- Meshing and simulation of the corresponding geometry with the use of an engineering simulation software.
- Calculation of dimensionless performance parameters, based on the simulation results.
- Comparison of calculated dimensionless parameters with normal ranges established in the literature.

## Table of Contents

Acknowledgements .....	I
Abstract .....	3
Nomenclature .....	5
Chapter 1: Jet Engine Operation Principles .....	6
1.1 Jet Engine Types .....	6
1.1.1 Turbojet .....	6
1.1.2 Turbofan .....	7
1.1.3 Turboprop/Turboshaft .....	8
1.1.4 Ramjet/Scramjet .....	9
1.2 Operation Principles of a Jet Engine .....	11
1.3 Operation of an Axial Turbine .....	13
Chapter 2: 2D Airfoil Design .....	17
2.1 Introduction .....	17
2.2 Definition of the 2-D Airfoil .....	18
2.3 Design of the 2-D Airfoil with CATIA V5R20 .....	20
Chapter 3: 3D Blade/Vane Design .....	31
3.1 Introduction .....	31
3.2 3D Design of the Blades/Vanes Using CATIA V5R20 .....	34
3.3 3D Design of the Complete Turbine .....	48
Chapter 4: ANSYS 17.0 Geometry and Meshing Modules .....	59
4.1 Geometry Import and Handling .....	59
4.2 Model Meshing .....	63
Chapter 5: Problem Setup and Boundary Condition Specification .....	74
5.1 Boundary Conditions Calculation .....	74
5.2 Simulation Setup in ASYS 17.0 .....	77
Chapter 6: Results Analysis .....	81
6.1 Results Extraction .....	81
6.2 Results Evaluation .....	83
6.3 Performance Parameters Calculation .....	94
6.4 Stage Losses Calculation .....	98
6.5 Conclusion, Further Work Motivation .....	105
References .....	106

## Nomenclature

$P$	<i>Pressure</i>
$T$	<i>Temperature</i>
$\rho$	<i>Density</i>
$F$	<i>Force</i>
$A$	<i>Cross Section Area</i>
$D$	<i>Diameter</i>
$U$	<i>Blade Speed/Tangential Velocity</i>
$C$	<i>Absolute Velocity</i>
$V$	<i>Relative Velocity</i>
$A$	<i>Degree of Reaction</i>
$\phi$	<i>Flow Coefficient</i>
$\psi$	<i>Stage Loading Coefficient</i>
$h$	<i>Enthalpy</i>
$\dot{W}$	<i>Power</i>
$\dot{Q}$	<i>Heat Transfer Rate</i>
$\dot{m}$	<i>Mass Flow Rate</i>
$C_p$	<i>Specific Heat Constant Pressure</i>
$\pi$	<i>Pressure Ratio</i>
$\tau$	<i>Shear Stress</i>
$c$	<i>Chord</i>
$\eta$	<i>Efficiency</i>
$\alpha$	<i>Relative Velocity Angle</i>
$\beta$	<i>Absolute Velocity Angle</i>
$s$	<i>Pitch</i>
$t$	<i>Blading Thickness</i>
$\omega$	<i>Rotational Velocity</i>
$R$	<i>Radius</i>
$g$	<i>Gravity Constant</i>
$Y$	<i>Pressure Loss Coefficient</i>
$\gamma$	<i>Specific Heats Ratio</i>
$VR$	<i>Velocity Ratio</i>
$y^+$	<i>Dimensionless Wall Distance</i>
$u_t$	<i>Friction Velocity</i>

**Note:** An <sub>0</sub> subscript denotes a stagnation quantity, while no subscript denotes static quantity, wherever static and stagnation quantities apply.

# Chapter 1: Jet Engine Operation Principles

## 1.1 Jet Engine Types

Jet engines generally fall into the following categories:

- Turbojet
- Turbofan
- Turboprop/Turboshaft
- Ramjet/Scramjet

The common component in the first three categories is the gas generator. The gas generator is comprised of three major assemblies: the compressor, the combustor and the turbine. The purpose of the gas generator is to “generate” or supply high-temperature and high-pressure gases to the jet engine.

### 1.1.1 Turbojet

Turbojet engines were the first jet engines introduced to aircraft propulsion by von Ohein (first use August 1939). These engines are comprised of a gas generator, an inlet and a nozzle. Later versions of the turbojet incorporated an afterburner/augmenter (or re-heater, as used in the earlier stages of jet aviation). In essence the turbojet engine is the most stripped down version of the jet engine family.

Turbojet engines produce thrust by compressing ambient air through the inlet and compressor, then adding fuel to the compressed gas through combustion in a combustion chamber and then expanding the burnt gas through a turbine and a nozzle. The turbine extracts work from the hot gases, in order to provide power to the compressor, achieving sustained operation for the engine. The net thrust produced is the product of transforming internal gas energy into kinetic energy, and for the most part is being produced in the nozzle, by accelerating the subsonic exhaust gas to speed greater than the inlet gas speed [Mattingly, 1996].

One of the best known turbojets is the General Electric J79 that was used to power the F-4 Phantom fighter aircraft (among others).

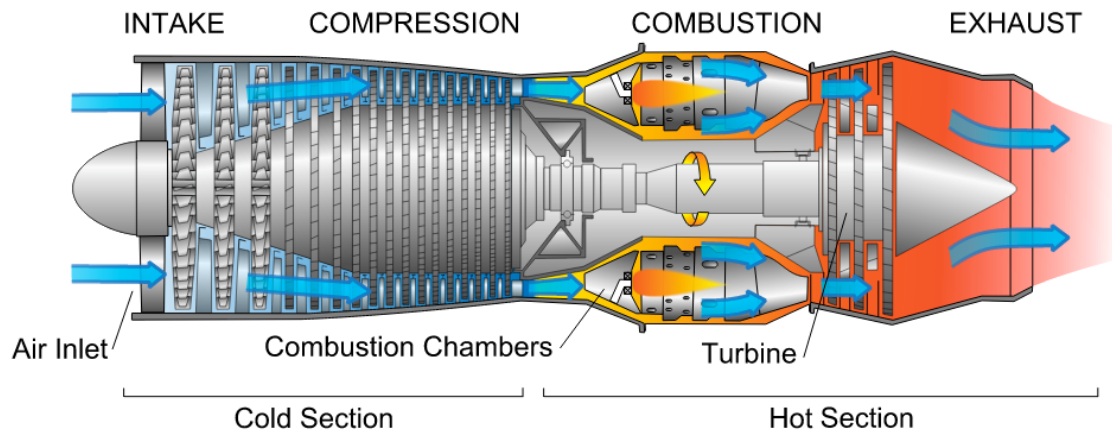


Figure 1.1.1: Turbojet engine [<https://aerospaceengineeringblog.com/jet-engine-design/>].

### 1.1.2 Turbofan

The turbofan engine consists of an inlet, a fan, or a Low Pressure Compressor (LPC), the gas generator, a Low Pressure Turbine (LPT) and a nozzle. As with the turbojet, an augmenter can also be included. What sets apart the turbofan from its predecessor, is the low pressure turbomachinery and the splitting of the flow into two sections: the core flow and the bypass flow. The core flow travels through the gas generator, as it would on a turbojet engine. On the other hand, the bypass flow travels around the gas generator, without undergoing any combustion whatsoever. The two flows are being mixed after the LPT, in the engine's exhaust nozzle.

Since the turbofan produces gases at a lower exhaust speed, its propulsive efficiency is greater than that of the turbojet, making it ideal for airliners and civil aviation. Furthermore, the TSFC, or Thrust Specific Fuel Consumption, is lower for the turbofan when compared to the turbojet. [Mattingly, 1996].

The drawback of such engines is that the frontal area of the engine is increased in comparison to the turbojet, resulting in increased drag. To tackle the issue, and allow for turbofans to be used in the military aviation, this engine family can be further divided into two subcategories: the high- and low-bypass turbofans. High-bypass turbofans are usually used in civil aviation, due to their high efficiency, while low-bypass turbofans are favored by military aviation, being a compromise between the turbojet and the high bypass turbofan.

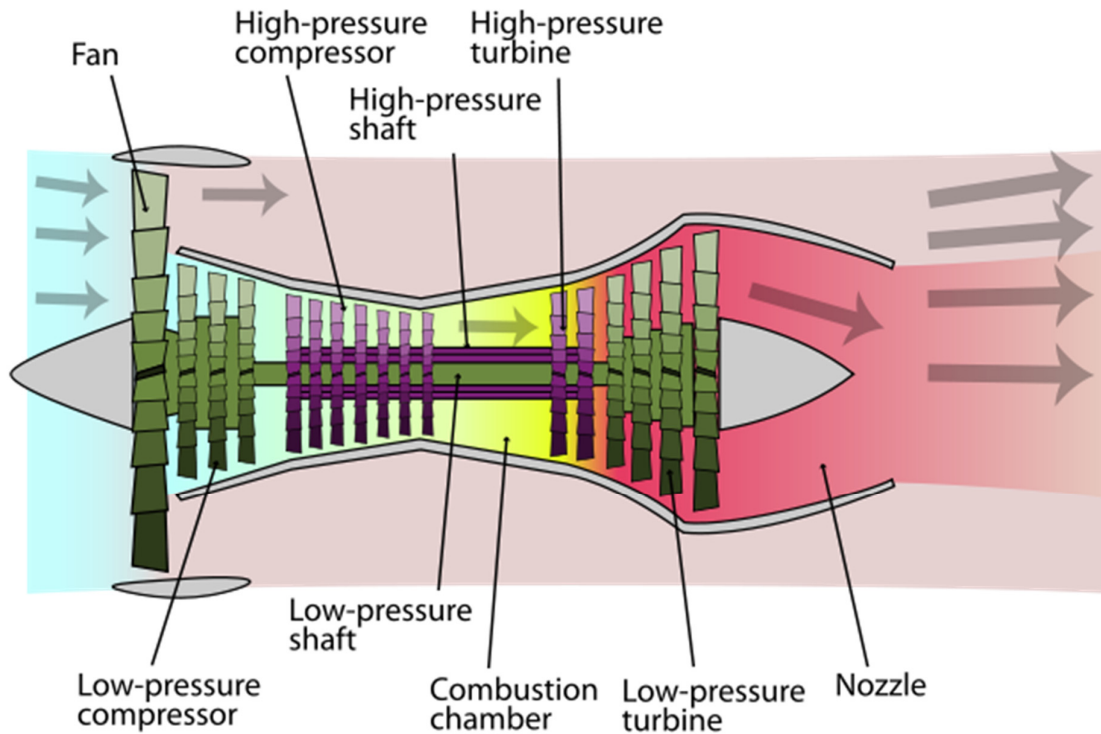


Figure 1.1.2: Turbofan engine [<https://aerospaceengineeringblog.com/jet-engine-design/>].

Well known engines of this family are the PW JT9D, the PW4000, all being high-bypass engines, and the PW-F100-200 series, when it comes to their low-bypass counterparts.

### 1.1.3 Turboprop/Turboshaft

The turboprop engine uses the gas generator and a power turbine downstream, to power a propeller, at the front of the engine. Rotational speed reduction is achieved via a gearbox, hence the increased weight of the turboprop. Put plainly, the turboprop has no actual nozzle (as no acceleration of the exhaust gas occurs). Instead, the remaining internal energy of the gases that exit the gas generator is used to power the power turbine (which in turn rotates the thrust producing propeller) and then are expelled through a “generic” exhaust. The shortcomings and advantages of the turboprop engine stem from the shortcomings and advantages of the propeller it drives. In low subsonic speeds the turboprop has a high performance advantage, but when high subsonic speeds are approached, compressibility effects arise, resulting in a serious loss of the aerodynamic efficiency of the propeller [Mattingly, 1996].

The turboshaft engine operates in pretty much the same way, but instead of driving a propeller, the gas generator drives a shaft. Turboshaft engines are used mainly by helicopters when it comes to aviation. Turboshaft engines are also enjoying a wide range of ground applications in industry and power production.

Notable examples of turboprop/turboshaft engines are the Alison T-56, powering the C-130 and the P-3 aircrafts, and the PW PT6 engines.



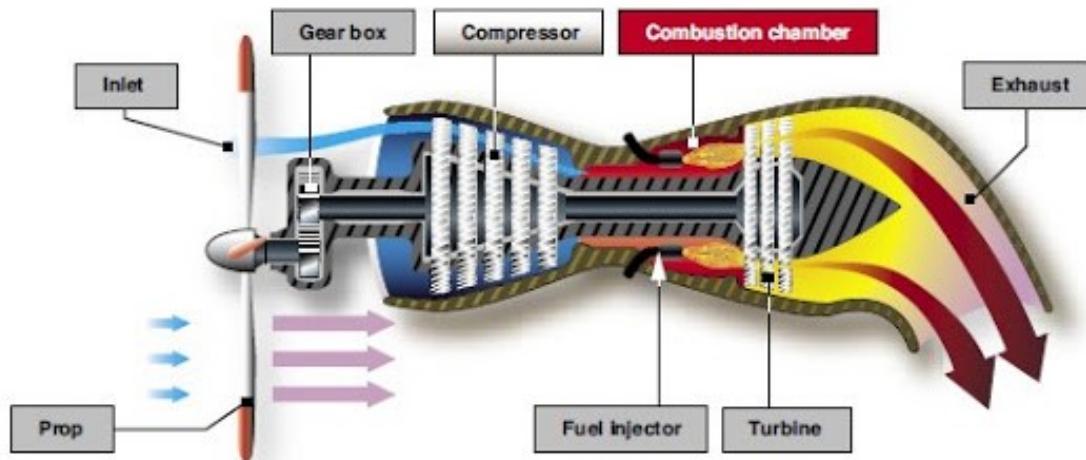


Figure 1.1.3 Turboprop engine [[http://knowtothis.blogspot.com/2009/12/turboprop.html#.W\\_xf2ugzZjE](http://knowtothis.blogspot.com/2009/12/turboprop.html#.W_xf2ugzZjE)].

#### 1.1.4 Ramjet/Scramjet

This family of engines does not have any rotating parts. The compressor is replaced by a variable geometry inlet that produces a series of shock waves, thus compressing the incoming air to the desired pressure. The inlet's variable geometry regulates the compression and at the same time assures subsonic combustion in the combustion zone upstream. After combustion the hot gases are ejected through the nozzle, producing thrust.

Due to the peculiar nature of the ramjets' compression, adequate speed of intake air is required. The greater the intake speed the greater the compression ratio. For this reason, ramjet engines need to operate in the high supersonic spectrum. When operating in subsonic or even low supersonic speeds the ramjet is woefully inefficient and in some cases cannot even be started.

To overcome the above, ramjet engines are often paired with turbojet engines that are responsible for the acceleration of the aircraft up to a certain speed, before the ramjet is suitable for operation. Scramjet engines (supersonic combustion ramjet) are engines where supersonic combustion takes place, designed for hypersonic aircraft.

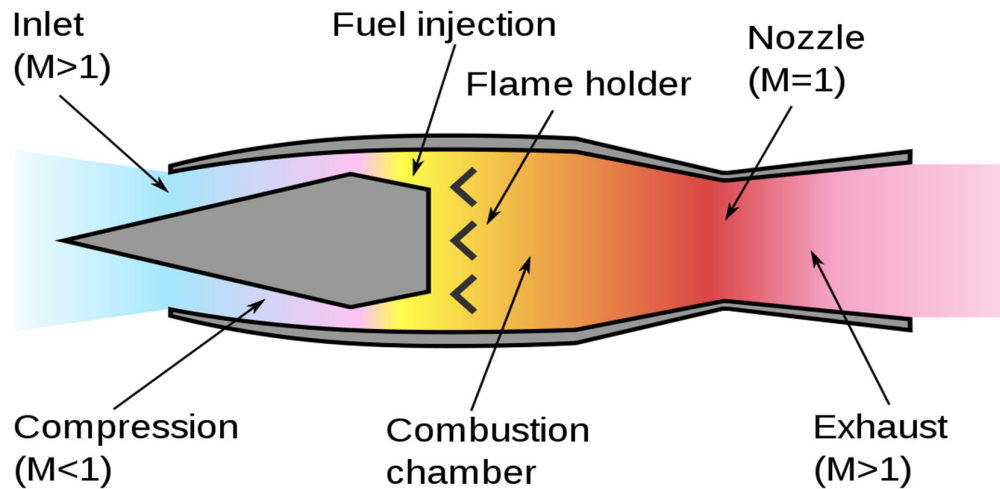


Figure 1.1.4: Ramjet engine [<https://en.wikipedia.org/wiki/Ramjet>].

A legendary example of a turbojet/ramjet pair is the PW J58 engine that was used to power the SR-71 Blackbird. The blackbird is fairly known for holding (to this day) the crown for the fastest aircraft ever produced (Mach 3+). The J58 operates as an afterburning turbofan up to a certain high Mach number. After that critical Mach number six tubes located on the engine's duct are bypassing the air completely from the gas generator and directing it into the engine's afterburner that now acts as the combustion zone for the ramjet.

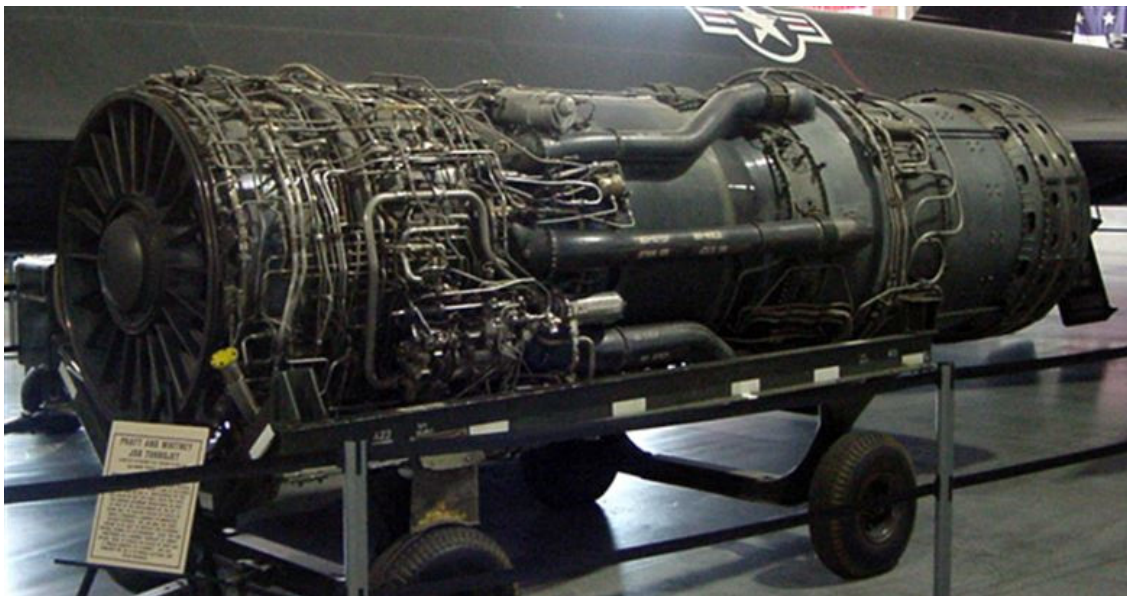


Figure 1.1.5: The J58 engine [<https://www.hill.af.mil/About-Us/Fact-Sheets/Display/Article/397503/j58-turbojet-engine/>].



Figure 1.1.6: The SR-71 aircraft performing a ground run [<https://taskandpurpose.com/sr-71-blackbird-afterburners-photos/>].

As stated above, the combustion process in a ramjet engine needs to take place in the low subsonic area. Recent research and development has made possible that combustion in ramjet engines can take place in the supersonic spectrum. If a ramjet engine realizes its combustion in the supersonic spectrum it is called a scramjet (supersonic combustion ramjet) [Mattingly, 1996].

## 1.2 Operation Principles of a Jet Engine

All jet engine families operate on the same thermodynamic principle: the Brayton Cycle. The Ideal Brayton Cycle consists of the following processes:

- Isentropic compression.
- Constant pressure heat addition.
- Isentropic expansion.
- Constant pressure heat rejection.

The basic components in charge of the Brayton cycle are the gas generator (compressor, turbine combustor/heater) with the addition of a cooler. The components and the corresponding cycle can be seen in Figure 1.2.1.

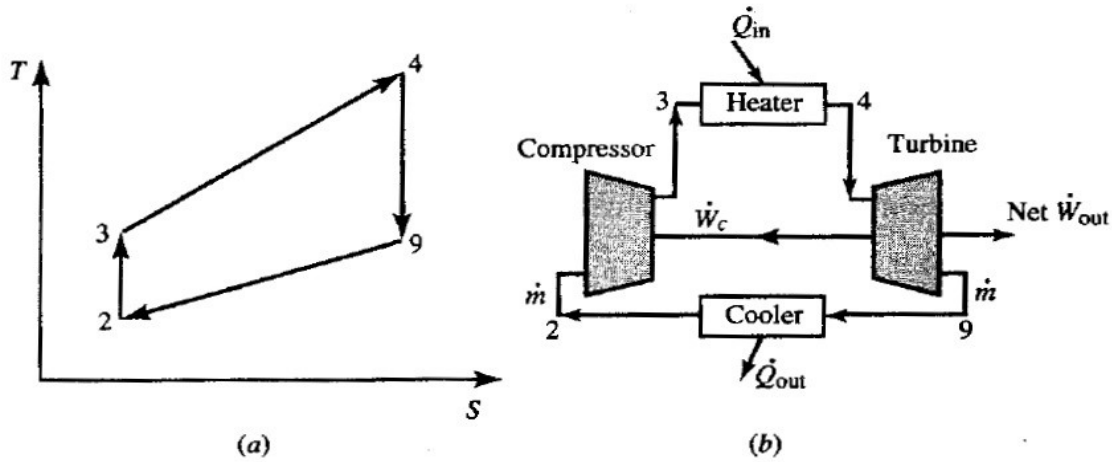


Figure 1.2.1: (a) Brayton cycle; (b) Brayton cycle components [Mattingly, 1996].

Considering a calorically perfect gas, the following equations, derived from the thermodynamic analysis of the cycle, depict the rate of energy transfer for each of the above components [Mattingly, 1996].

$$\dot{W}_c = \dot{m}c_p(T_3 - T_2) \quad (1.2.1)$$

$$\dot{W}_t = \dot{m}c_p(T_4 - T_9) \quad (1.2.2)$$

$$\dot{Q}_{in} = \dot{m}c_p(T_4 - T_3) \quad (1.2.3)$$

$$\dot{Q}_{out} = \dot{m}c_p(T_9 - T_2) \quad (1.2.4)$$

$$\dot{W}_t = \dot{W}_c \quad (1.2.5)$$

As one can conclude from the above, ambient air is compressed through the compressor. The compression of the gas is a power consuming process, so in many occasions  $\dot{W}_c$  can be denoted as  $|\dot{W}_c|$ , since strictly speaking  $\dot{W}_c < 0$ . Then, the compressed air's internal energy is increased via the combustion process, where heat is transferred to the gas, by means of harnessing the LHV (Lower Heating Value) of the injected fuel. The gas is then expanded in the turbine, which extracts works from the flow, driving the compressor. It should be noted that Eq. 1.2.5 holds true with the assumption that no mechanical losses occur on the shaft and that the turbine drives only a single compressor. The gas is then expelled at the exit of the turbine, cooling down while ejected through a nozzle.

The ejection of the gas through the nozzle is not without purpose. The nozzle accelerates the burnt gas to high subsonic speeds (or supersonic speeds for convergent-divergent nozzles) producing thrust in the process. The thrust equation is as follows

$$F = \frac{(\dot{m}_o + \dot{m}_f)V_e - \dot{m}_o V_o}{g_c} + (P_e - P_o)A_e. \quad (1.2.6)$$

Eq. 1.2.6 derives the *uninstalled* thrust of the engine. *Installed* thrust can be derived from the following equation

$$T = F - D_{inlet} - D_{nozzle}. \quad (1.2.7)$$

Another thing worth noting is that it is generally desirable to expand the gas to ambient pressure ( $P_e = P_o$ ), thus eliminating the thrust's pressure component. Eliminating said component increases the thrust's velocity component by a change greater than the resulting loss of the "pressure thrust", yielding a net gain in overall thrust. A nozzle that does not expand the exhaust gas to ambient pressure is called a **choked nozzle**. A nozzle capable of the latter is called an **adaptive nozzle** [Hünecke, 1997].

As a final note, the reader is presented with the following turbojet schematic (Fig. 1.2.2), depicting the fluctuation of operation parameters for the turbojet engine).

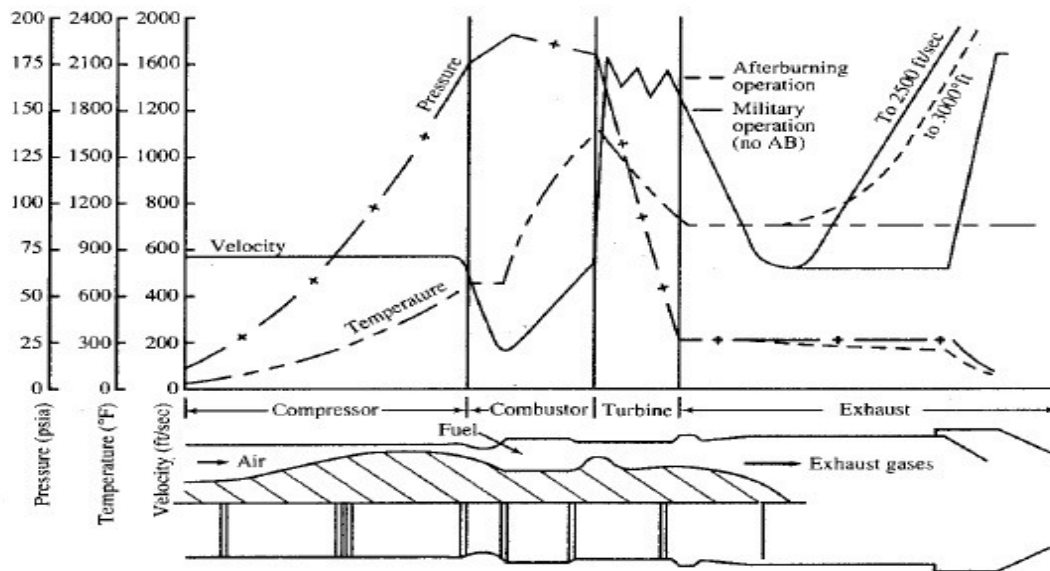


Figure 1.2.2: Parameter fluctuation for the J-79 turbojet engine [Mattingly, 1996].

### 1.3 Operation of an Axial Turbine

As stated above, the turbine is a pivotal component of any jet engine consisting of rotating turbomachinery. In this section a brief overview of turbine operation will be given, since the main scope of the current thesis is the simulation of one such component.



Axial flow turbines are the most common when high power turbomachinery is considered. Historically, axial flow turbines are an outgrowth of the traditional steam turbine, that being said, its design is significantly different from its predecessor. An axial turbine can be considered to be the inverse of its counterpart, the axial compressor. The turbine, in contrast to the compressor, is outlined as a stator-rotor configuration, instead of the rotor-stator configuration of the latter.

Axial turbines can be divided into two categories: the impulse and the reaction turbines. The gas travelling through the impulse turbine has its designated enthalpy drop done entirely in the nozzle (stator), resulting in high fluid velocities at the entrance of the rotor. On the other hand, the reaction turbine splits its enthalpy reduction between the rotor and the stator within the same stage. The following Figure 1.3.1 depicts roughly the variation of temperature, pressure and absolute velocity within the turbine.

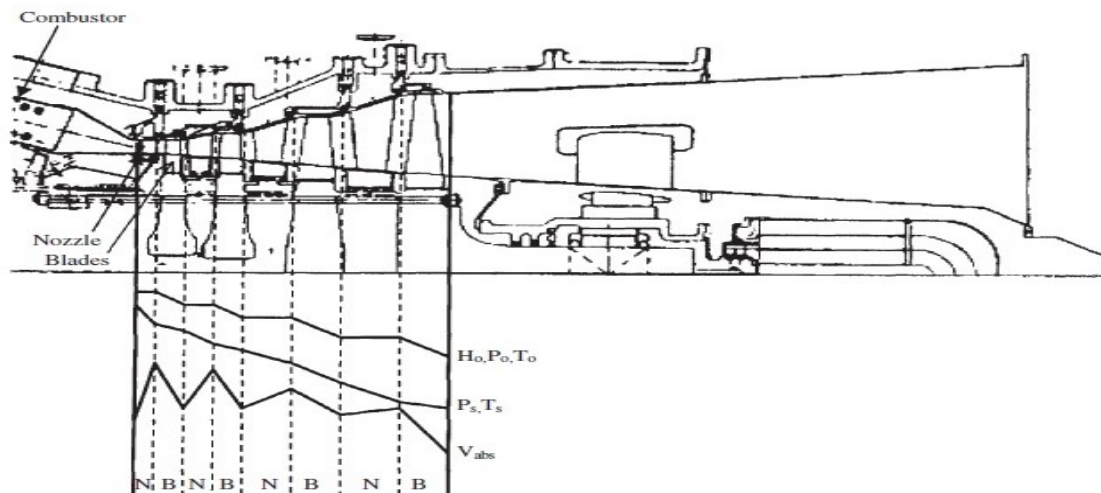


Figure 1.3.1: Temperature, pressure and absolute velocity variation in an axial turbine [Boyce, 2002].

The high temperatures achieved in modern turbines are possible due to new developments in metallurgy, coating applications and cooling solutions. It is not uncommon for modern turbines to operate at 1600 °C TIT (Turbine Inlet Temperature) [Boyce, 2002].

Probing a little deeper into turbine operation, one cannot delegate the importance of velocity triangles, defining turbine operation and performance characteristics. Velocity triangles are consisted of three velocities: the absolute velocity, the relative velocity and the tangential rotational velocity. Those three velocities can vectorially be expressed as follows:

$$\vec{C} = \vec{V} + \vec{U} \quad (1.3.1)$$

The following Figure 1.3.2 shows how flow develops through a one stage cascade, with the use of velocity triangles.

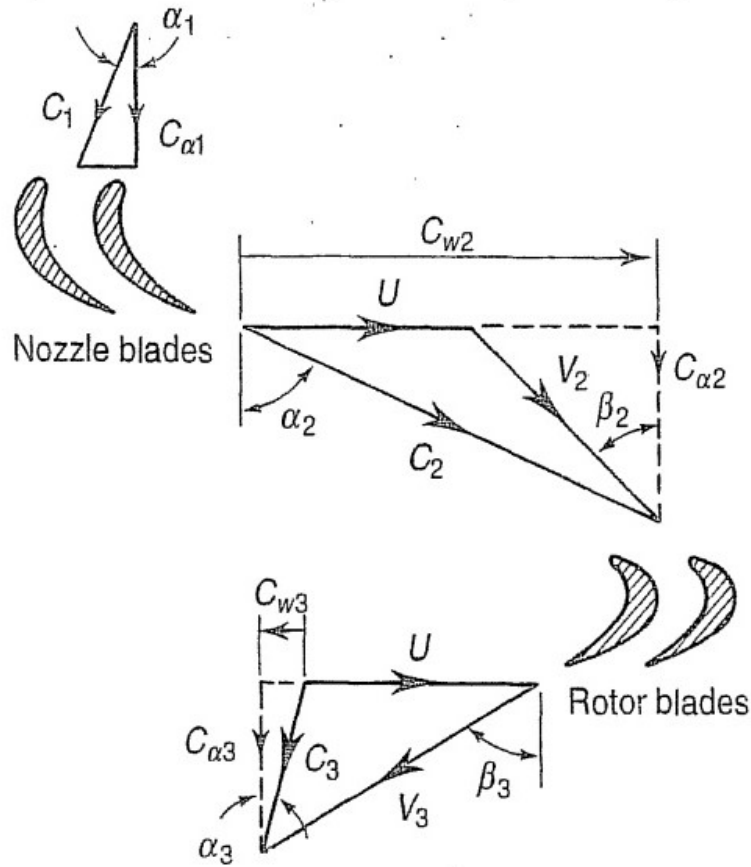


Figure 1.3.2: Velocity triangles for a turbine stage [Cohen et al., 1996].

Fundamental information can be extracted from the velocity triangles. Some of the most important coefficients defining turbine performance are the work coefficient  $\psi$ , the flow coefficient  $\varphi$  and the degree of reaction  $\Lambda$ .

The work coefficient, or stage loading, is defined as

$$\psi = \frac{C_p \Delta T_o^{stage}}{U^2}. \quad (1.3.2)$$

The flow coefficient is defined as

$$\varphi = \frac{C_a}{u}. \quad (1.3.3)$$

The degree of reaction is defined as

$$\Lambda = \frac{T_2 - T_3}{T_1 - T_3}. \quad (1.3.4)$$

Having the above coefficients, one can calculate the stage total-to-total isentropic efficiency and in extend the turbine's isentropic efficiency [Dick, 2015]

$$\eta_{tt} = \frac{\psi}{\psi + \frac{1}{2\xi_s} \left[ \varphi^2 + \left( 1 - \Lambda + \frac{\psi}{2} \right)^2 \right] + \frac{1}{2\xi_r} \left[ \varphi^2 + \left( 1 + \Lambda + \frac{\psi}{2} \right)^2 \right]} \quad (1.3.5)$$

Another important aspect of an axial turbine is its' work output capacity. The above can be calculated by making use of the Euler equation for turbomachines [Wiberg et al., 2013]

$$w = \frac{\dot{W}}{\dot{m}} = U_2 C_{U2} - U_1 C_{U1}. \quad (1.3.6)$$

A more in depth look on said coefficients will be conducted further below, alongside their value calculation for the subsequent simulated axial turbine.



## Chapter 2: 2D Airfoil Design

### 2.1 Introduction

After the preliminary turbine design, the next step to be taken is the definition of the blades' (rotary, stationary) geometry. The design process commences with the 2-D definition of the airfoil profile.

2-D airfoil design can be implemented in a variety of ways. The two most prevalent are the following:

Pressure side and suction side are considered to be high order polynomials or are being represented by the general conic-section equation. After the definition of both pressure and suction sides of the 2-D airfoil, the leading and trailing edges are to be defined. A common practice is to define both of them as circles, with their radii being equal to half of the desired trailing and leading edge thickness [Augnier, 2006]. It is worth noting that in some cases the trailing edge can be represented by a line segment connecting the aft points of the pressure and suction side of the airfoil [Dusa et al., 1964].

Pressure and suction sides are not explicitly defined, rather designed implicitly, by first defining the equation of the mean camber line and then creating a thickness distribution off of it. The leading and trailing edges are similarly implicitly defined by the thickness distribution polynomial.

The first method utilizes certain physical parameters, such as the throat width, leading and trailing edge thickness, and blade and gas inlet/outlet angles. The above parameters are then used as input to the polynomial or conic equations in order to determine the unknown constants [Dusa et al., 1964].

Similarly, the second method uses physical parameters for the definition of the mean camber line, such as inlet/outlet blade section angle and blade stagger angle. Then, the thickness distribution is defined by imposing points on both sides of the mean camber at certain fractions of the cambers length and normal distances from it. The above points can then be used as control points for a NURBS or Bezier curve or as interpolation points [Koini et al., 2009].

The first method was used for the definition of the blades' and vanes' airfoils studied herein. More specifically, the method described in [Dusa et. al., 1964] was preferred, thus the pressure and suction sides were defined through the use of conic sections and elliptical equations, while the leading and trailing edges were considered to be circles, with radii corresponding to the airfoil's leading and trailing edge half thickness.

## 2.2 Definition of the 2-D Airfoil

As stated above, the design of the airfoils was conducted according to [Dusa et. al., 1964]. The suction side is considered to be best represented by the characteristic equation of a general second degree conic section, shown below

$$x^2 + Bxy + Cy^2 + Dx + Ey + F = 0. \quad (2.2.1)$$

The equation for the pressure side of the airfoil is generated by a second order elliptical equation, as follows

$$x^2 + By^2 + Cx + Dy + E = 0. \quad (2.2.2)$$

Implicit differentiation of Eq. (1.2.1) and (1.2.2) yields the following form

$$2x + \left(y + x \frac{dy}{dx}\right)B + \left(2y \frac{dy}{dx}\right)C + D + \left(\frac{dy}{dx}\right)E = 0, \quad (2.2.3)$$

and

$$2x + \left(2y \frac{dy}{dx}\right)B + C + \left(\frac{dy}{dx}\right)D = 0. \quad (2.2.4)$$

The term  $\frac{dy}{dx}$  in Eq. (2.2.3) and (2.2.4) denotes the slope of the curve represented by Eq. (2.2.1) and (2.2.2) and therefore it can be rewritten as follows

$$\frac{dy}{dx} = \tan \theta. \quad (2.2.5)$$

Substitution of Eq. (1.2.5) in Eq. (1.2.3) and (1.2.4) yields the following:

$$2x + (y + x \tan \theta)B + (2y \tan \theta)C + D + E \tan \theta = 0, \quad (2.2.6)$$

$$2x + (2y \tan \theta)B + C + (\tan \theta)D = 0. \quad (2.2.7)$$

In order to calculate the constant coefficients  $A, B, C, D, E, F$ , a set of boundary conditions is needed, that when applied to Eq. (2.2.1), (2.2.2), (2.2.6), (2.2.7), will yield a set of six equations. The set of the generated equations will in turn be used to calculate the corresponding unknown coefficients.

The boundary conditions that are to be used, are depicted in Fig.1.2.1 and are as follows:

- Suction Side Boundary Conditions.
  1.  $x$  and  $y$  at point (1).
  2.  $x$  and  $y$  at point (2).
  3.  $x$  and  $y$  at point (3).
  4. Slope at point (2).
  5. Slope at point (3).
- Pressure Side Boundary Conditions.

1. x and y at point (4).
2. x and y at point (5).
3. Slope at point (4).
4. Slope at point (5).

For the above conditions to be defined, a number of physical characteristics of the blade passage must be known. For the test case at hand, Table 1.2.1 contains all necessary data.

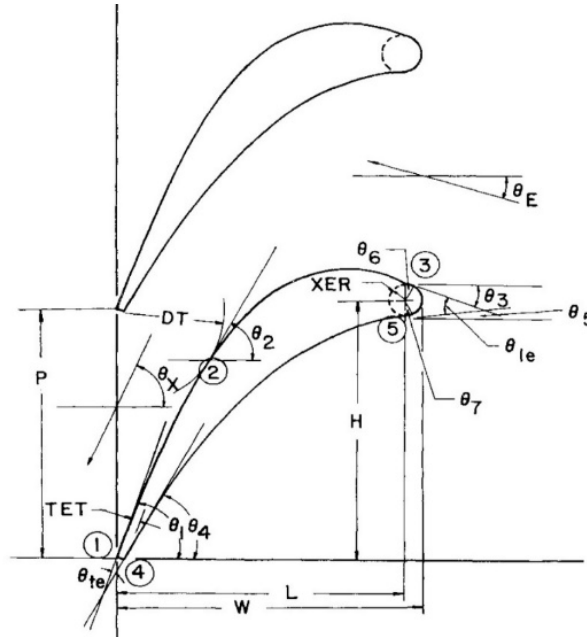


Figure 2.2.1: Blade passage physical characteristics [Dusa et. al., 1964].

TET	Trailing Edge Thickness
XER	Leading Edge Radius
DT	Throat Width
P	Pitch
W	Blade Width
H	Blade Height
$\theta_E$	Inlet Angle
$\theta_x$	Exit Angle

Table 2.2.1: Blade Passage Nomenclature.

After the calculation of the boundary conditions, the generated set of six equations yields the corresponding coefficients, necessary for the definition of the pressure and suction sides of the rotor and two stators blades. The equations for the rotor blade are the following:

- Suction side:

$$x^2 + 1.104xy - 0.746y^2 - 59.941x + 30.145y = 0 \quad (2.2.7)$$

- Pressure side:

$$x^2 + 0.557y^2 - 57.546x + 34.981y + 49.699 = 0 \quad (2.2.8)$$

The equations for the first stage stator blade are the following:

- Suction side:

$$x^2 + 0.321y^2 - 75.344x^2 - 44.914y + 154.277 = 0 \quad (2.2.9)$$

- Pressure side:

$$x^2 + 2.266xy - 1.594y^2 - 109.625x + 62.172y = 0 \quad (2.2.10)$$

The equations for the second stage stator blade are the following:

- Suction Side:

$$x^2 + 1.144xy - 0.539y^2 - 63.171x + 25.647y = 0 \quad (2.2.11)$$

- Pressure side:

$$x^2 + 0.501y^2 - 61.782x + 38.794y + 71.608 = 0 \quad (2.2.12)$$

## 2.3 Design of the 2-D Airfoil with CATIA V5R20

After the analytical definition of the conics and elliptic equations, representing the pressure and suction sides of the blade partitions, the explicit form  $y(x)$  should be defined for each curve in order to be suitable for Excel processing.

In order to achieve the above, [quickmath.com, 2018] was implemented and thus the following equations were derived (note that the following equations are written in an Excel acceptable format)

**Rotor** is defined by:

- Pressure Side:

$$y(x) = \left( (361 * 184111^2 - 222752 * 100000 * x^2 + 222752 * 5754637 * x - 222752 * 4969980)^{\frac{1}{2}} - 3498109 \right) * \left( \frac{1}{111376} \right). \quad (2.3.1)$$

- Suction Side:

$$y(x) = - \left( (42079724036 * x^2 - 1124315560724 * x + 9087469498849)^{\frac{1}{2}} - 110494 * x - 3014543 \right) * \left( \frac{1}{149354} \right). \quad (2.3.2)$$

**First stage stator** is defined by:

- Pressure Side:

$$y(x) = \left( (361 * 184111^2 - 222400 * 100000 * x^2 + 222400 * 5754600 * x - 222400 * 4969900)^{\frac{1}{2}} - 3498109 \right) * \left( \frac{1}{111200} \right). \quad (2.3.3)$$

- Suction Side:

$$y(x) = - \left( (42079724036 * x^2 - 1124315560724 * x + 9087469498849)^{\frac{1}{2}} - 110494 * x - 3014543 \right) * \left( \frac{1}{149354} \right). \quad (2.3.4)$$

**Second stage stator** is defined by:

- Pressure Side:

$$y(x) = \frac{1}{501} * \left( (-501000 * x^2 + 30952782 * x + 340368001)^{\frac{1}{2}} - 19397 \right). \quad (2.3.4)$$

- Suction Side:

$$y(x) = - \frac{1}{1078} * \left( 1.732 * (1154912 * x^2 - 25838780 * x + 219256203)^{\frac{1}{2}} - 1144 * x - 25647 \right). \quad (2.3.5)$$

The equations above are inserted into an Excel spreadsheet and points 1 *mm* apart are used as input. The output is calculated and then the  $x$  and  $y(x)$  values are collected and copied to a second Excel Sheet, suitable for point insertion into CATIA V5R20. The above sheet can be found in CATIA installation path under the name “GSD\_PointSplineLoftFromExcel”. The aforementioned spreadsheet contains the macros suitable for the operation of Cartesian points insertion into CATIA V5R20.

The top and bottom commands are to be kept (“Start Loft”/“Start Curve” and “End Loft”/“End Curve”/“End”), while the data in-between must be erased. The freed up cells will accommodate the previously calculated Cartesian coordinates. It should be noted that more cells can be inserted, in order to apply a larger number of points, if so desired.

The airfoils at hand were constructed using fifty points for each curve of pressure and suction sides, respectively. Below, the process of point implementation in CATIA is shown step-by-step, each step being accompanied by relevant figures.

To calculate the Cartesian coordinates we insert Eq. (2.3.1) through (2.3.6) to an Excel spreadsheet, by modifying them accordingly.

	A	B	C	D	E	F
1	x var press	y var press	y var press alt root	x var suction	y var suction	y var suction alt root
2	-4	-10.07404256		-4	-8.057438468	
3	-3	-7.51146573		-3	-6.026706286	
4	-2	-5.266852584		-2	-4.005661389	
5	-1	-3.264023048		-1	-1.996040545	
6	0	-1.454437753	1.454437753	0		-40.36775714
7	1	0.195115974	-0.195115974	1	1.979758406	-39.86762432
8	2	1.708560473	-1.708560473	2	3.939817058	-39.38719126
9	3	3.10380671	-3.10380671	3	5.875812009	-38.93082189
10	4	4.394676031	-4.394676031	4	7.782120613	-38.50413888

Figure 2.3.1: Cartesian points' calculation.

Figure 2.3.1 applies for the first stage rotor. Similar action has to be taken for the curves of the first and second stage stators.

The  $(x, y(x))$  sets shall now be collected and copied to the second spreadsheet, under the name "GSD\_PointSplineLoftFromExcel". An overview of this new spreadsheet should have the following form (Fig. 2.3.2):

	A	B	C	D	E
1	StartLoft				
2	StartCurve				
3	-4	-10.07404256			
4	-3	-7.51146573			
5	-2	-5.266852584			
6	-1	-3.264023048			
7	0	-1.454437753			
8	1	0.195115974			
9	2	1.708560473			
10	3	3.10380671			
11	4	4.394676031			
12	5	5.592094608			
13	6	6.704871456			
14	7	7.740224971			
15	8	8.704150814			
16	9	9.60168597			
17	10	10.43710268			
18	11	11.21405378			
19	12	11.93568341			
20	13	12.60471279			
21	14	13.22350743			
22	15	13.79413043			
23	16	14.31838525			
24	17	14.79785018			
25	18	15.23390554			
26	19	15.62776161			
27	20	15.98046765			
28	21	16.29293744			
29	22	16.56595719			
30	23	16.80019718			
31	24	16.99622039			
32	25	17.15448961			
33	26	17.27537307			
34	27	17.35914876			
35	28	17.40600776			
36	29	17.41605635			
37	30	17.38931728			
38	31	17.32572998			
39	32	17.22514992			
40	33	17.08734694			
41	34	16.91200257			
42	35	16.69870631			
43	36	16.44695069			
44	37	16.15612502			
45	38	15.82550762			
46	39	15.45425631			
47	40	15.04139679			
48	41	14.58580857			
49	42	14.08620802			
50	43	13.5411276			
51	44	12.9488907			
52	45	12.3075808			
53	EndCurve				
54	EndLoft				
55	End				
56					

Figure 2.3.2: Layout of the points.

It should be noted that the numbers in the left column represent the  $x$  coordinate, while the numbers in the right column represent the  $y$  coordinate of each point.

After the correct positioning of the coordinates, the built-in macros are to be used. To achieve that, the command “Macros” must be selected, under the “VIEW” tab. The following windows should be adjusted, according to the following figures.

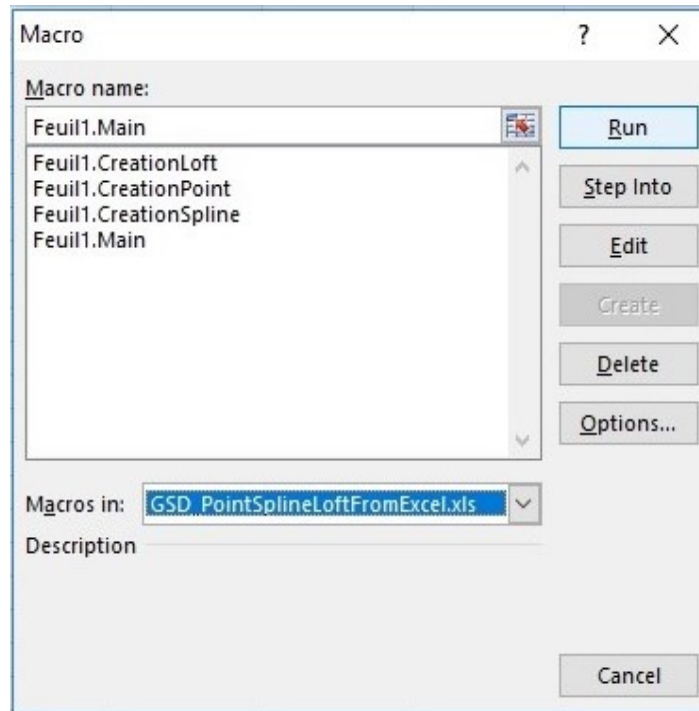


Figure 2.3.3: Macros window adjustment.

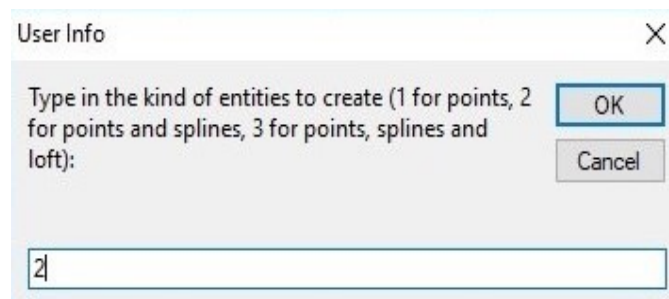


Figure 2.3.4: Point and spline selection.

Before the macro is run, it must be made sure that the CATIA V5R20 is running in the background and “Part” process is selected. More precisely, the Generative Shape Design (GSD) module of CATIA V5R20, should be active, since the design work will take place therein.

Clicking the OK button in the window of Fig. 1.3.4 will initiate the imposing of the points contained in “GSD\_PointSplineLoftFromExcel”, onto CATIA V5R20 interface. Since “2” is selected in the aforementioned window, the imposed points will be accompanied by a spline defined by them.

After the concealment of the inserted points, CATIA V5R20 Part Design environment should now look like the following Figure 2.3.5.

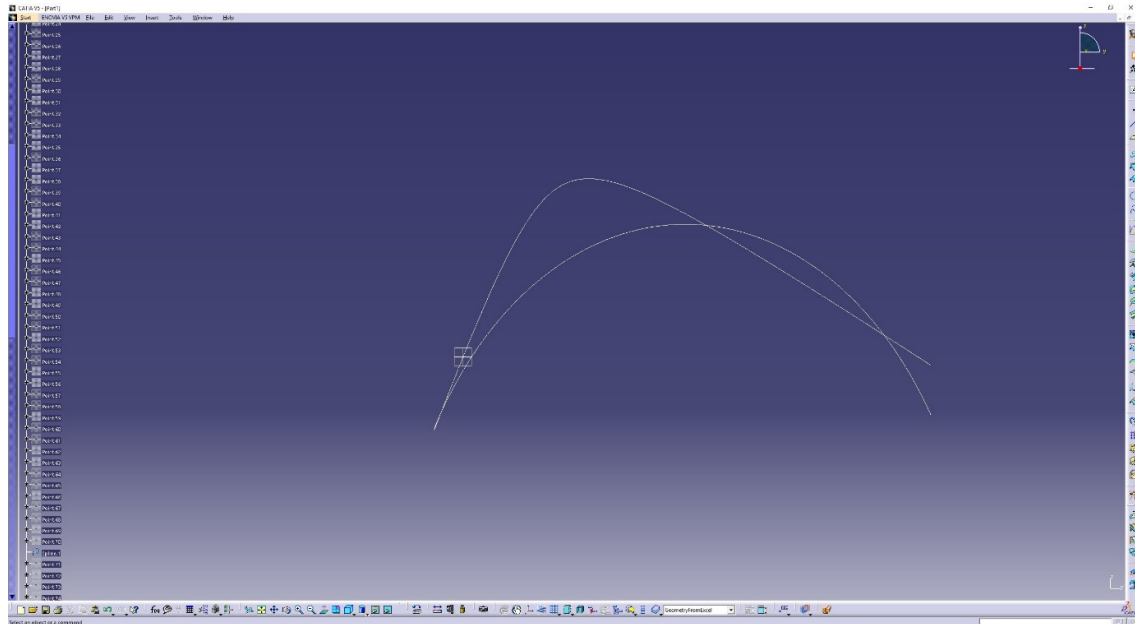


Figure 2.3.5: Pressure and suction sides import.

As shown in Fig. 2.3.5, pressure and suction sides are having longer than desired lengths and that's because their respective “domains” are containing more elements than required. A need to trim both curves arises and that is possible with the implementation of the leading and trailing edges.

In order to define the leading edge of the airfoil, a circle needs to be added that is tangent to both pressure and suction sides. Therefore, the “Circle Definition” command should be selected. A window containing details for the circle definition pops-up should be set up, as shown in Fig. 2.3.6.



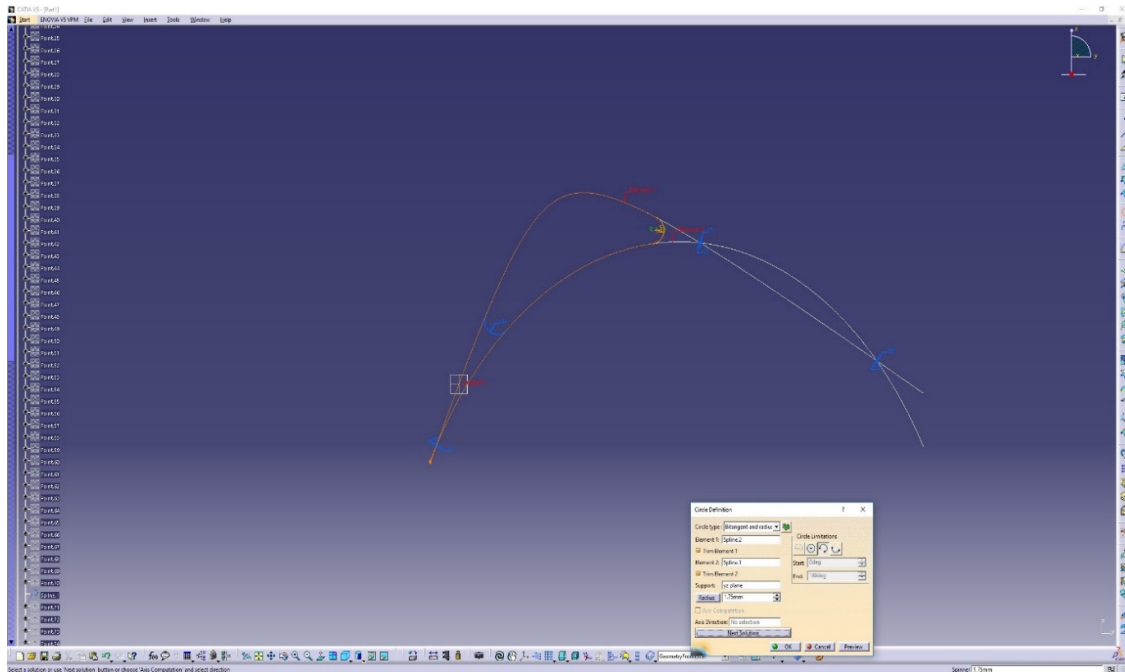


Figure 2.3.6: Leading edge circle definition.

The circle should be defined by “Bitangent and radius”, the two tangents being the pressure and suction sides and the radius should be equal to the desired leading edge thickness. Also the “Trim Element 1/2” should be chosen.

After the definition of the leading edge, the trailing edge needs to be added, in order to achieve a complete airfoil. First, the existing airfoil needs to be dismantled, in order to separate pressure side, suction side, and the leading edge, since CATIA V5R20 now recognizes all three of the above as the previously defined circle, making it impossible to choose two tangents needed for the trailing edge circle design.

The above is achieved with the “Dismantle” command, and is shown in more detail in Figure 2.3.7. After the disassembly, the line is broken down in three parts: two splines (that represent the trimmed pressure and suction sides) and a circle (that represents the merged leading edge circle with the rest of the airfoil). The three parts can now be selected individually, thus making it possible to select the two generated splines as the two tangents of the trailing edge circle.

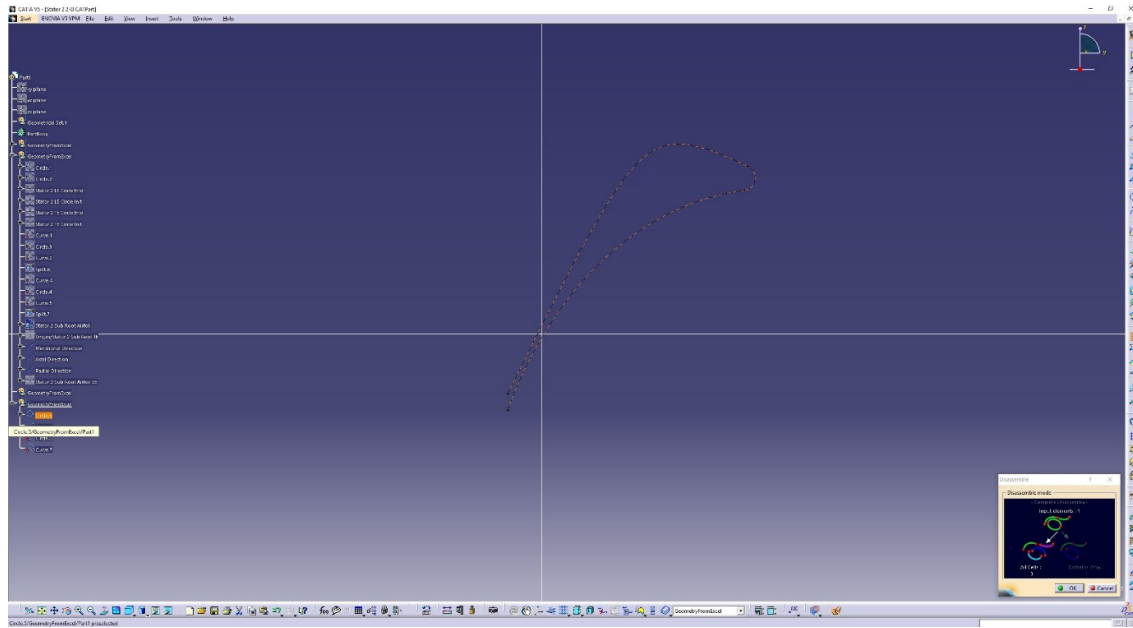


Figure 2.3.7: Disassemble command.

Similarly with the leading edge circle, the trailing edge circle is created, by choosing the “Circle Definition” command and, while in the set-up window, by choosing “bitangent and radius”, the two newly formed splines as tangents and the desired radius. Identically to the leading edge circle, the choice “Trim Element1/2” should be checked.

The airfoil, yet complete, is still not well defined. The airfoil now consists of two circles, one being the leading edge circle (left untouched after the “disassemble” command) and the other being the late formed circle of the trailing edge that now contains the trailing edge and the two splines generated from the previous disassembly. Those two “circles” should now be joined into one single closed airfoil.

To achieve that, the “Join” command should be used, acting upon the two separate parts of the airfoil. Figure 2.3.8 shows the set-up of the “Join” command in more detail.

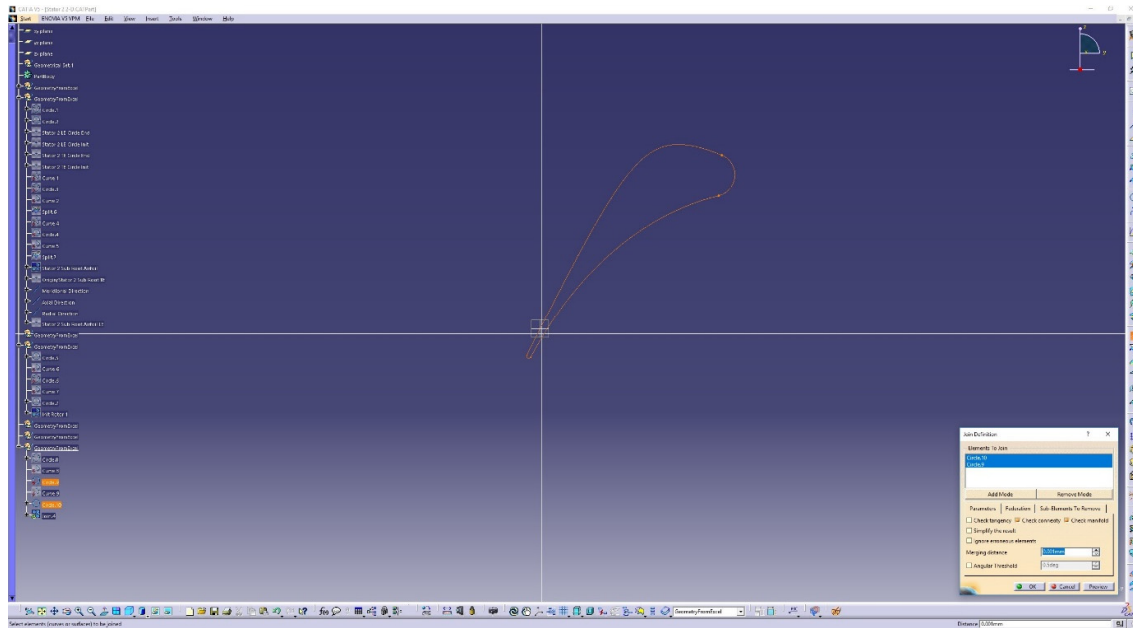


Figure 2.3.8: Airfoil join command.

The airfoil is now complete and well defined. The same process should now be repeated for the other two airfoils, in order to get the complete 2D design. It would be wise to hide the previous completed airfoils, before inserting the new points from Excel, defining a new airfoil.

In order to complete the 2D design, airfoils should now be properly positioned, in accordance to the axial and meridional direction, to achieve proper spacing between the rotor and the two stators. A new axis system is set up, by changing the origin and replacing it with the trailing edge of the second stator airfoil and by maintaining the general direction of the new axis identical to what CATIA V5R20 has as default.

This is made possible by defining three lines intersecting at the second stator airfoil trailing edge and being perpendicular to the default planes set up by CATIA V5R20. The third line corresponds to the radial direction, which will be needed later, during the 3-D phase of design. The final outcome is depicted in Figure 2.3.9. It should be noted, that it is possible to keep the origin intact and maintain the default orientation of the axis system. A point to point translation of the initial, completed airfoil is then needed, so that its trailing edge coincides with the origin of the axis system.

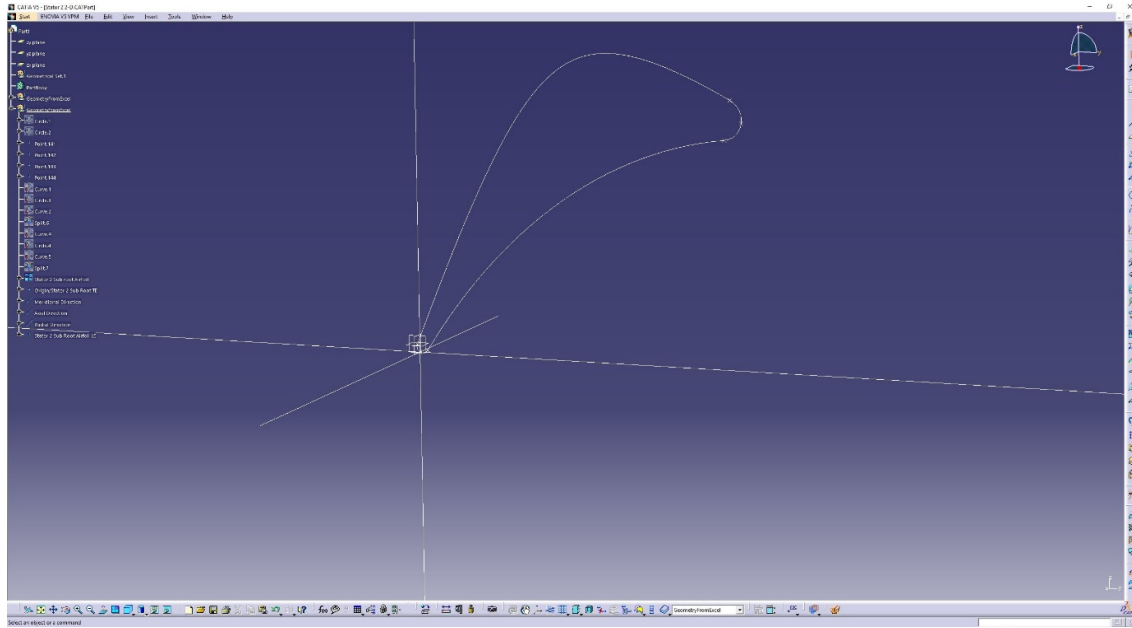


Figure 2.3.9: Axis system.

To achieve proper axial spacing between the airfoils, the leading edge of the second stator (which was generated first) is being projected onto the previously defined axial direction. From there, an axial distance must be set, for the definition of the spacing between second stator airfoil and rotor airfoil. Thus, a point is set on the axial direction axis, using the projected point as reference, at a distance equal to the required axial spacing of the second stator and the rotor. The same pattern should be repeated between the rotor and first stator, to achieve their respective axial spacing.

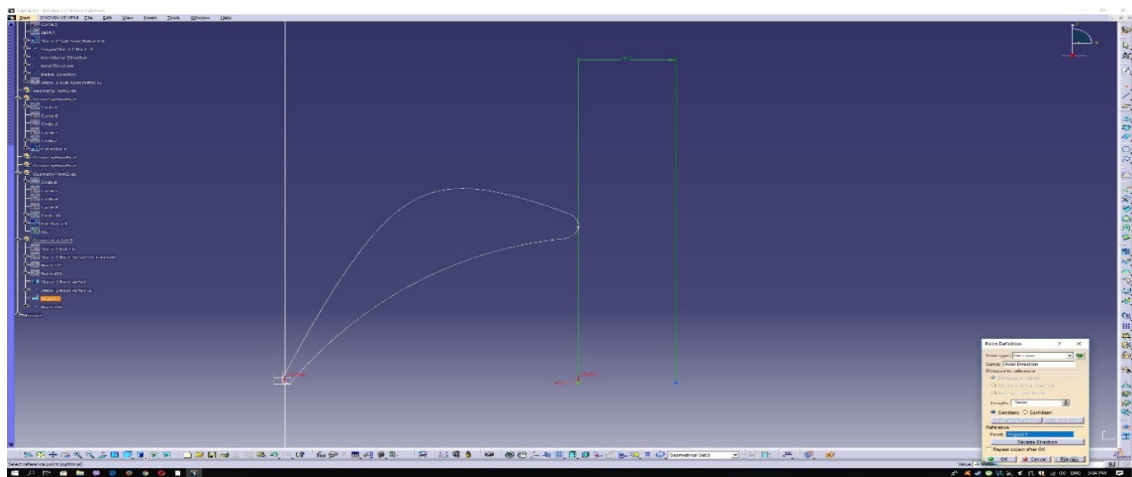


Figure 2.3.10: Rotor trailing edge positioning.

The point that was set at distance from the projected point (Fig 2.3.10), now represents the trailing edge of the rotor airfoil. This means that the rotor airfoil should now be translated axially, so that its actual trailing edge coincides with the newly formed point on the axial axis.

At this point, the rotor airfoil rests at the same general position as the stator airfoil (in Figure 2.3.10 the rotor airfoil is hidden). The rotor airfoil should now be axially translated. Figure 2.3.11 shows the translation operation enacted upon the airfoil, to set it at the correct axial position.

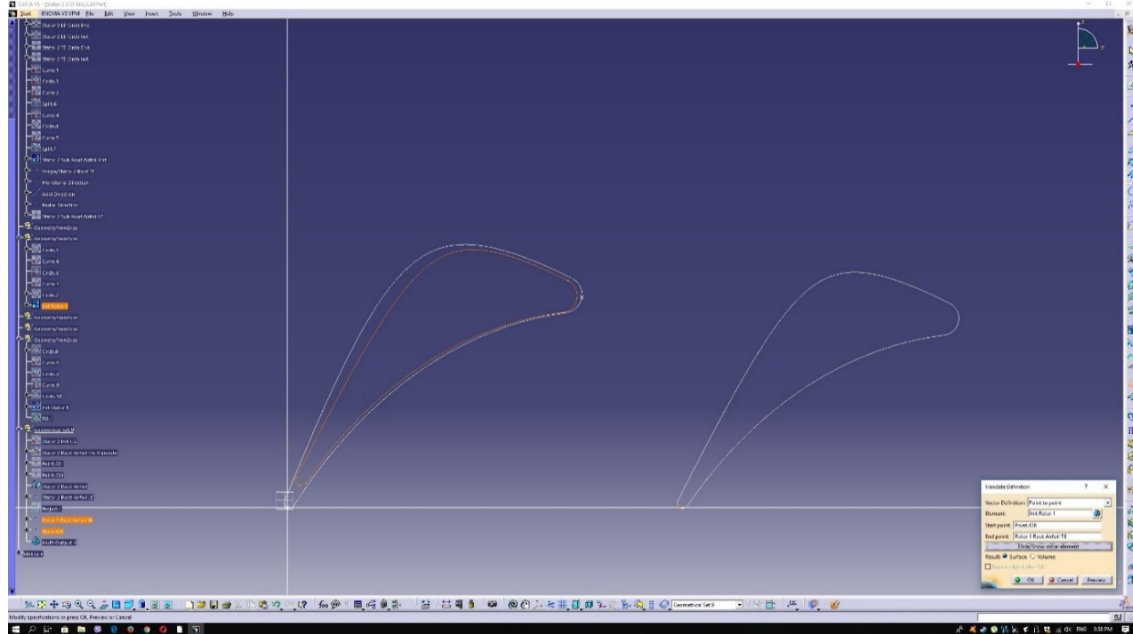


Figure 2.3.11: Rotor airfoil positioning.

As shown in Figure 2.3.11, the “Translate Definition” command has to be used. More precisely, the “Point to point” option should be chosen, the initial point being the trailing edge of the rotor airfoil at it’s present (colored orange) state and the final point being the point distanced axially in the previous step.

Obviously, the current rotors positioning is wrong, since the pitch angle ( $p$ ) is negative. The rotor airfoil, while remaining unmoved axially, should now have its orientation changed. To preserve the absolute value of the pitch angle (the same pitch angle is needed, only reversed) the “Symmetry” command is used. Figure 2.3.13 shows the set-up and the result that the above command yields. The symmetry axis should, obviously, be the axial direction.

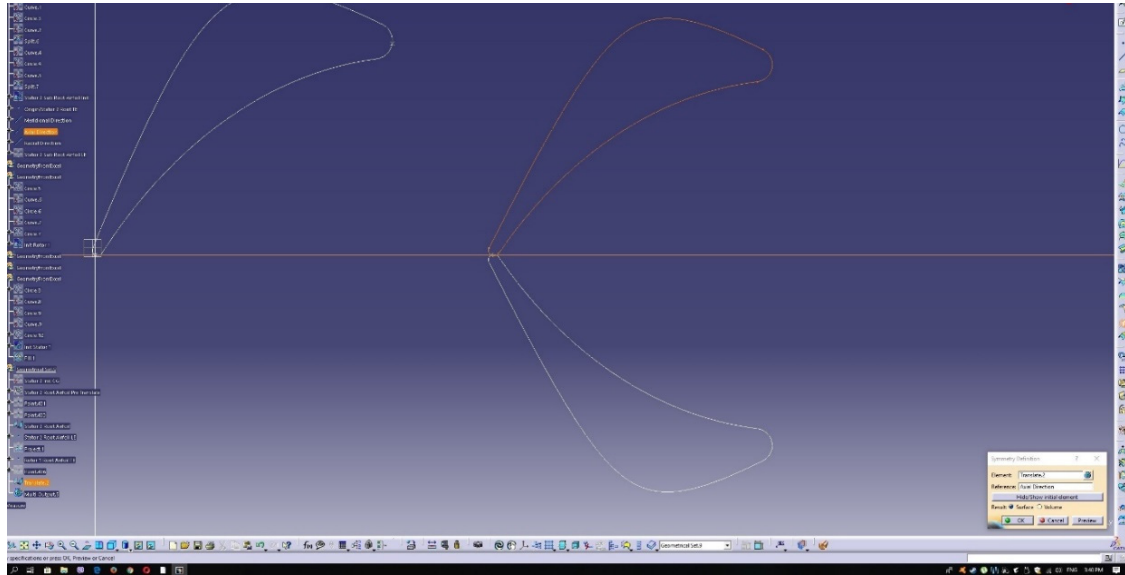


Figure 2.3.12: Rotor airfoil symmetry.

The rotor airfoil is now correctly positioned. The same process should be followed for the positioning of the stator, without the “Symmetry” command, since the stator’s initial orientation and pitch angle is the correct one. After the completion of the first stage stator positioning, the 2D airfoil design of the turbine is complete. The figure below shows how the final depiction of the 2D turbine profiles look like.

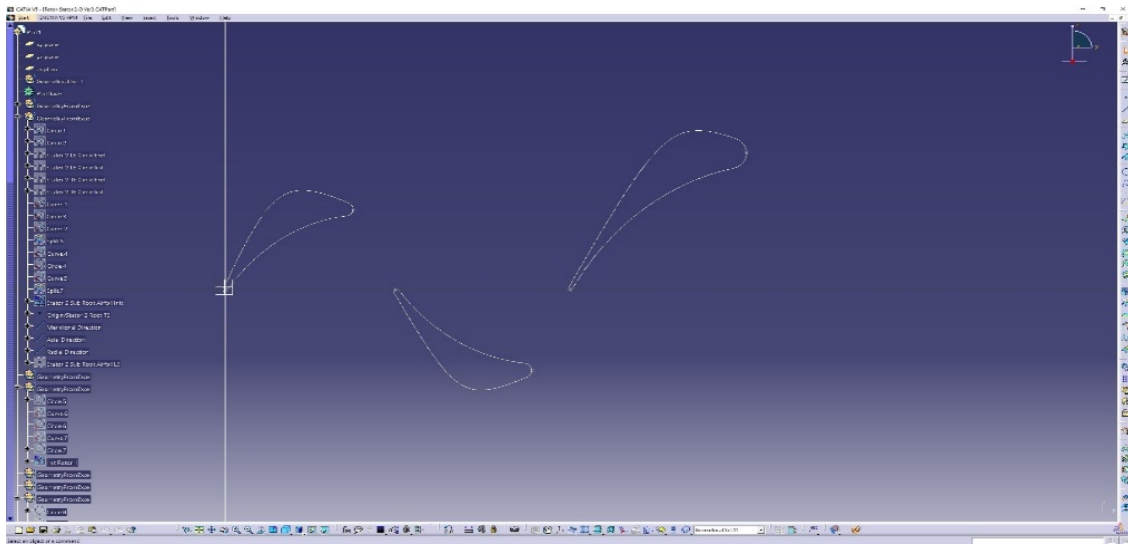


Figure 2.3.13: Final positioning of the blade profiles.

## Chapter 3: 3D Blade/Vane Design

### 3.1 Introduction

In order to design the 3D aspect of the turbine's blades and vanes the following physical characteristics should be taken into account:

- Blade taper.
- Blade twist angle.
- Blade skewness.

The term blade taper refers to the radial-wise variation of the airfoils' chord and overall area. It can be described by a linear or non-linear relationship between the chord and the radius, i.e.  $c=f(r)$ .

Blade taper is used mainly to reduce centrifugal stresses to the rotating blades. Turbine blades are usually tapered both in chord and cross sectional area with a taper ratio between 1/4 and 1/3, that is:

$$\frac{A_{tip}}{A_{hub}} \approx 1/4 - 1/3 \quad (3.1.1)$$

The centrifugal stresses that are applied to the rotor can be approximated by the following formula:

$$\sigma_b = 2\pi\rho_b N^2 A \quad (3.1.2)$$

The same stresses, when applied to a tapered blade, are approximated by the following:

$$\sigma_b = (4/3)\pi\rho_b N^2 A \quad (3.1.3)$$

Thus, we conclude that the stresses applied to a tapered blade, when compared to an untapered one, are reduced to almost 2/3 of the initial stress [El-Sayed, 2017].

Blade twist angle is the angle between the hub airfoil and the tip airfoil. The hub airfoil travels at a lower speed when compared to the tip airfoil. In order to keep the axial velocity constant radial-wise the relative velocity and angle change from root to tip [El-Sayed, 2017]. Furthermore, twist angle alleviates the fact that the velocity triangles differ from root to tip due to the blade speed variation ( $U$ ). The change in the blade metal angle tends to eliminate the angle of deviation, thus minimizing losses. Twisted blades are often called vortex blades [Cohen et al., 1996].

Lastly, skewness (or blade curve) is used to achieve a more uniform static pressure distribution span-wise. When it comes to conventional straight or even twisted blades, the radial component of the blades acting force on the flow is negligible and usually does not affect any of its parameters. Skewed blades take advantage of the radial component force to

even out static pressure and to mitigate radial secondary flows across the blade's surface boundary layer, thus decreasing energy losses. The radial equilibrium equation is given as:

$$\frac{1}{Q} \frac{\partial p}{\partial r} = \frac{V_u^2}{r} + \frac{w_m^2}{r_m} \cos(\sigma) - \frac{dw_m^2}{dm} \frac{\sin \sigma}{2} + F_r. \quad (3.1.4)$$

It can be seen that the radial variation of pressure is defined by four terms. The first term is the inertial centrifugal force of the fluid element, which is always a positive contributor. The second term is the radial component of the inertial centrifugal force due to the curvilinear motion of the fluid element in the meridional plane. The third term is the radial component of the meridional acceleration inertia force due to the motion of the fluid element on the stream surface. The final term is the radial component on the blade's acting force on the flow. This term can be either positive or negative, depending on the skewness of the blade. By controlling the fourth term, via the skewness of the blade, it is possible to affect the radial pressure gradient [Zou et. al., 2018].

The following figures show examples of tapered, twisted and skewed (curved) blades.

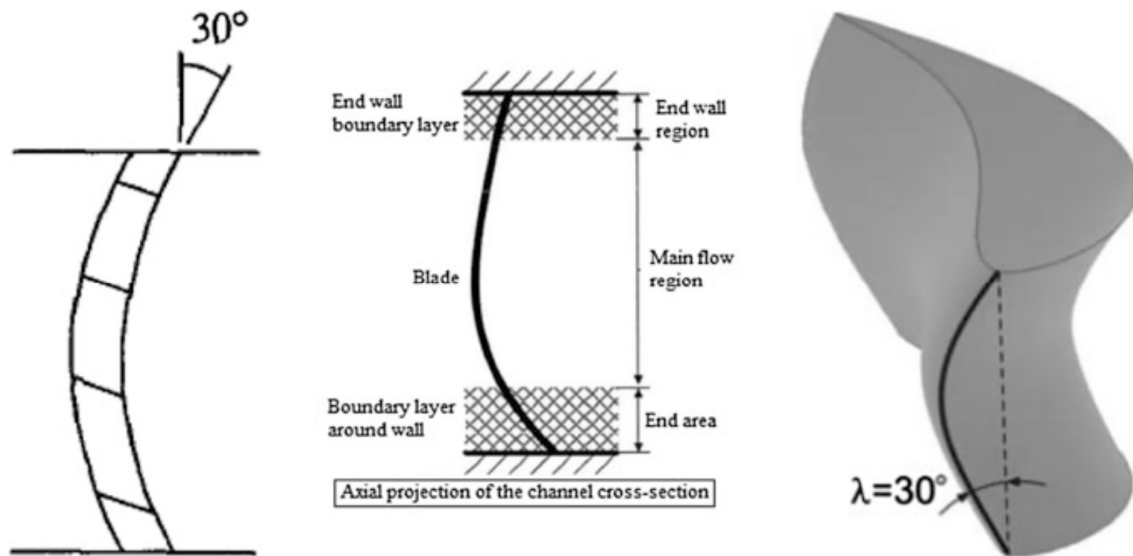


Figure 3.1.1: Skewed blade [Zou et. al., 2018].



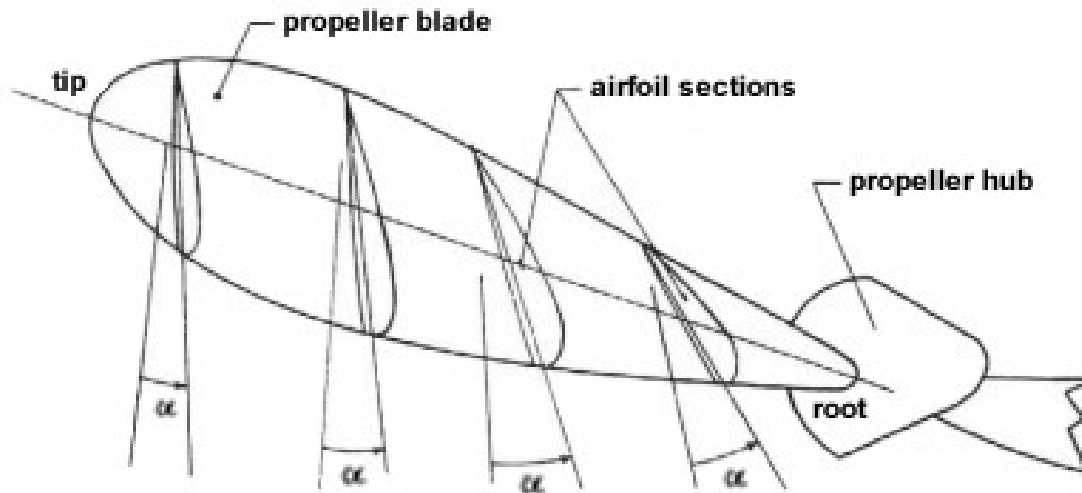


Figure 3.1.2: Twisted blade [<https://aviation.stackexchange.com/questions/43498/how-to-design-the-blade-twist-angle-in-propeller-design>].

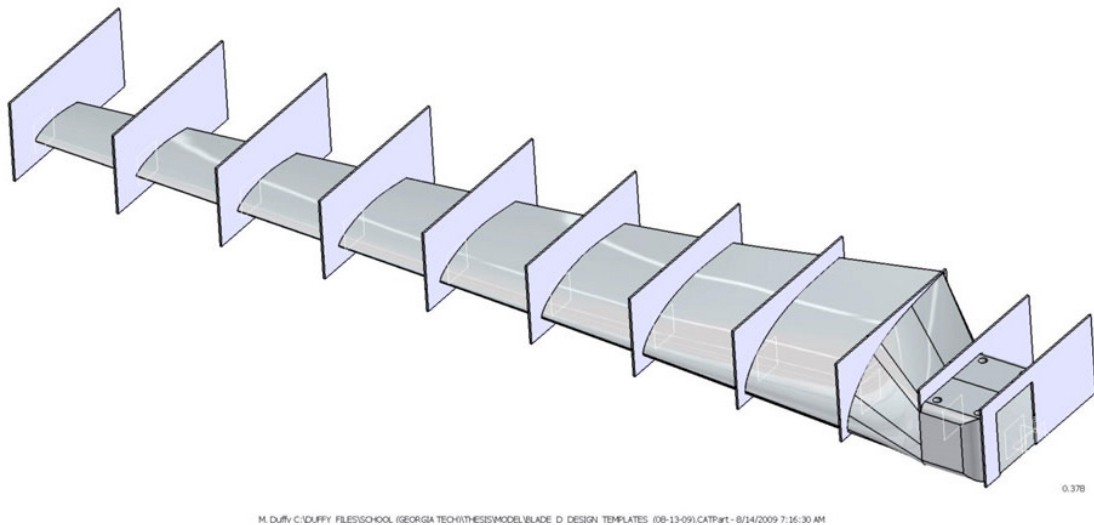


Figure 3.1.3: Tapered blade [<http://www.infobit.co/wind-turbine-blades-shape.html>].

In order to realize the above blade characteristics, a stacking line must be defined. In the previous section the 2D design of the blade was achieved, meaning that the 2D airfoil of the blade on an arbitrary plane was designed. In order to achieve a complete 3D blade several airfoils must be stacked one upon another in order to outline a 3D shape. This process requires the selection of a stacking line. The stacking line can be straight or it can be curved, especially if skewed blading is desired. The stacking line can be derived from the geometrical centers of each stacked airfoil, their leading or trailing edges or any other concrete point. [El-Sayed, 2017].

After the definition of the stacking line airfoils can be translated, rotated, and scaled accordingly, in order to achieve the desired span, taper, twist, and skewness.

In the confines of the current study a straight line spanning from the hub and tip airfoils' centers of gravity was constructed for the design of the 1<sup>st</sup> stage stator and the rotor, while a curved stacking line was used for the design of the 2<sup>nd</sup> stage stator.

Furthermore, the 1<sup>st</sup> stage stator is considered to have no taper, twist or skewness, the rotor is selected to have a uniformly linear twist angle and the 2<sup>nd</sup> stage stator has all three: taper, twist and skewness.

### 3.2 3D Design of the Blades/Vanes Using CATIA V5R20

Now the three corresponding airfoils must be turned into 3D blades. The first step is to define the stacking lines. As mentioned previously, the stacking lines for the 1<sup>st</sup> stage stator and the rotor are chosen to be straight lines and to span from centers of gravity (CG).

To realize the above, the CGs of the airfoils should be computed. In order to achieve that, the command “Fill” is used on each of the airfoils. It should be noted that for the “Fill” command to take place the boundary enclosing the area to be filled should be a closed contour. The “Join” commands that have been used in the previous chapters, achieve just that. As the airfoil is filled, a planar object is constructed, allowing the calculation of its gravity center. The figure below (Fig. 3.2.1) shows the command.

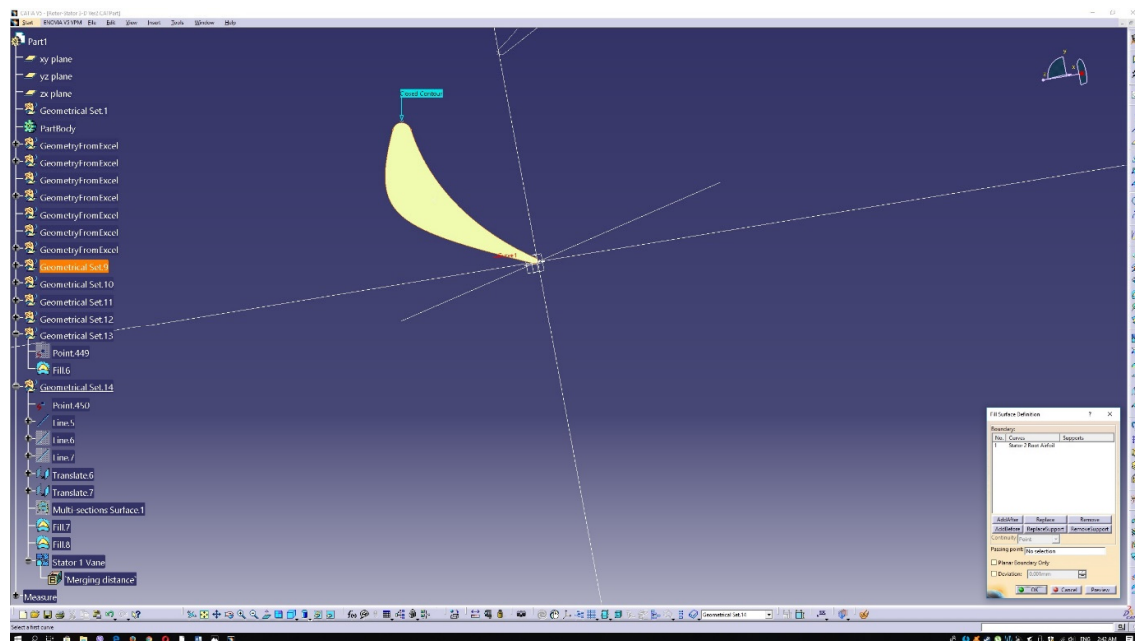


Figure 3.2.1: Fill command.

In order to calculate the coordinates of the airfoils' CG, the “Fill” object must be measured and the CG must be kept as an individual point. First the object is measured as depicted in the figure below. It should be mentioned that the Cartesian coordinates for the center of gravity

are already presented on the emerging window, yet it is faster and more secure to instantly create the CG rather than to create a new point by copying said coordinates.

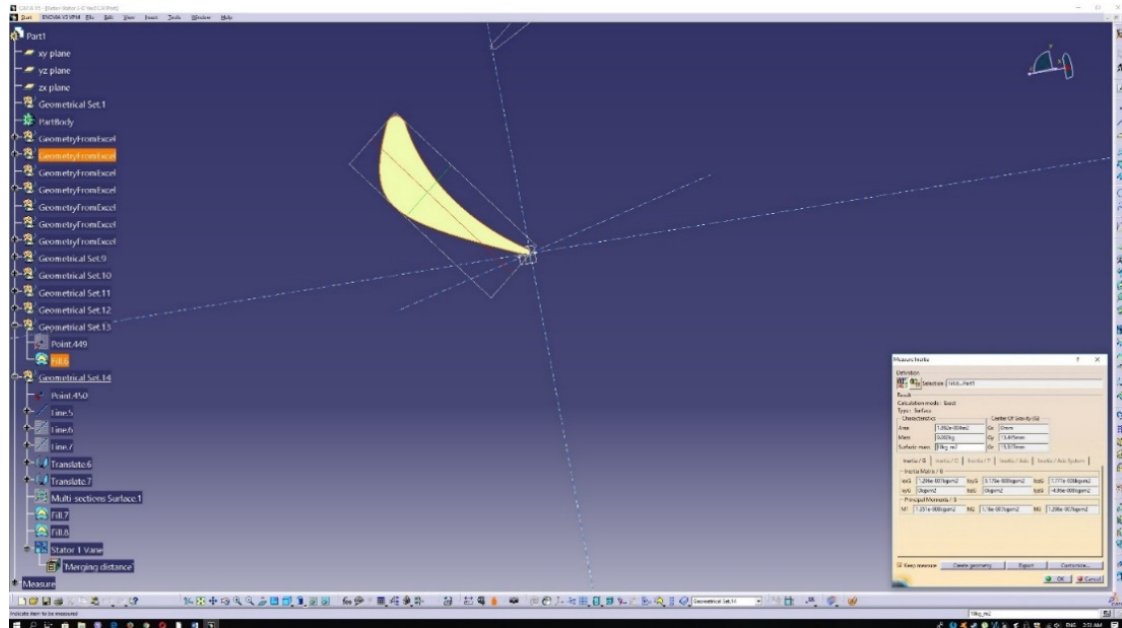


Figure 3.2.2: Airfoil center of gravity.

After that, the “Create Geometry” command should be selected, as well as the “Non-Associative Geometry” option on the emerged window. Finally, the “Center of Gravity” should be selected and a new point will be created representing the airfoil’s CG.

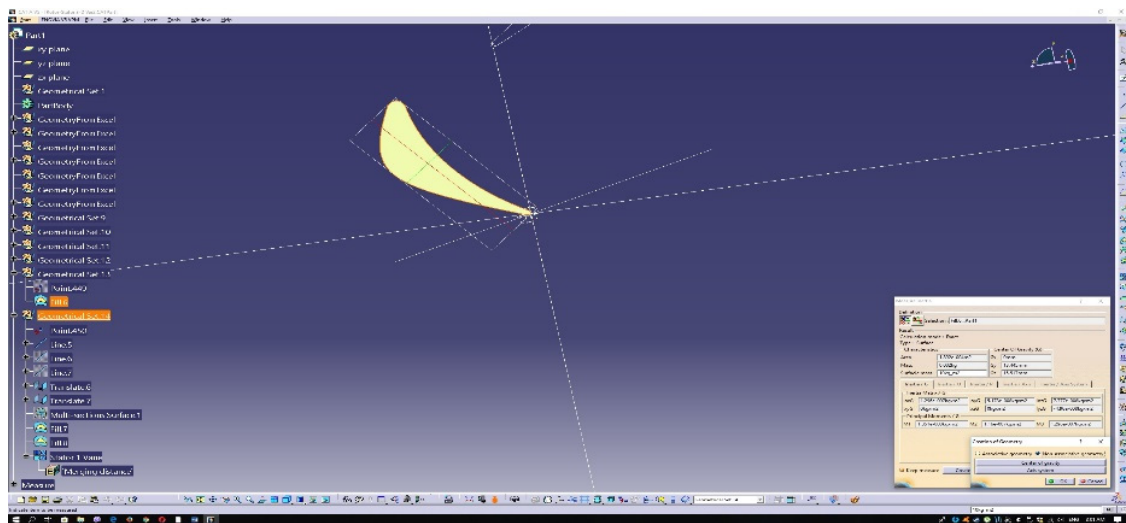


Figure 3.2.3: Create geometry.

For the stacking line to be created an axis perpendicular to the region defined by the airfoil and a point should suffice. Thus, the “Line” command must be used with the characteristics encompassed in the following Figure 3.2.4.

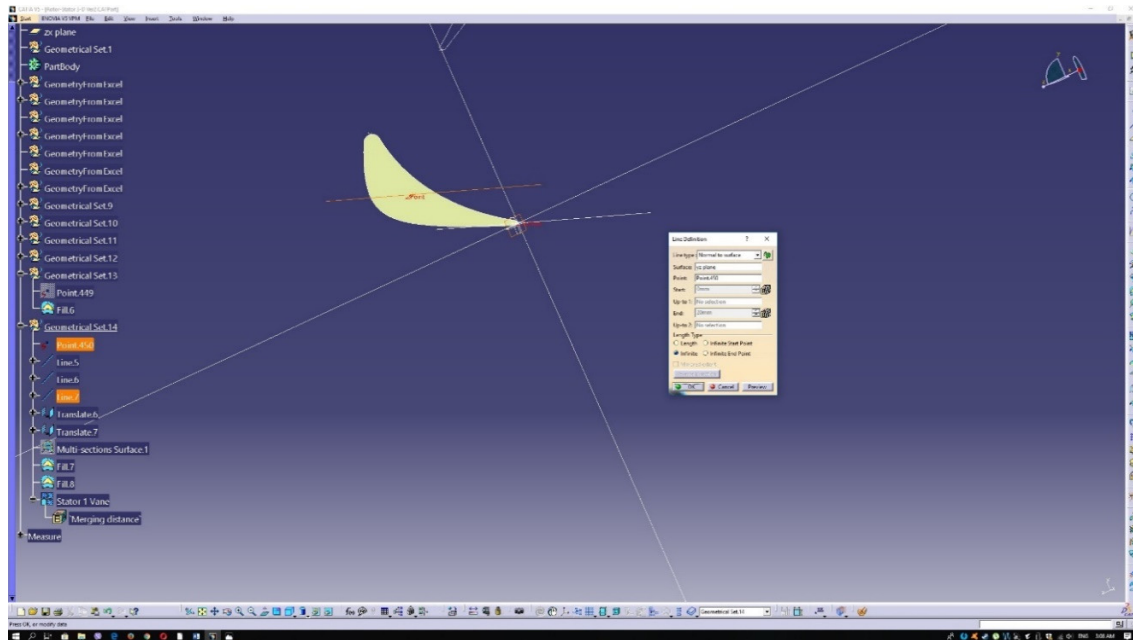


Figure 3.2.4: Stacking line definition.

The same process should be applied to the rotor airfoil. As for the 2<sup>nd</sup> stator airfoil a similar process will be followed that will be revisited shortly. Nevertheless, the 2<sup>nd</sup> stator must also have a straight stacking line. In summary, the airfoils and their stacking lines are presented in Figure 3.2.5.

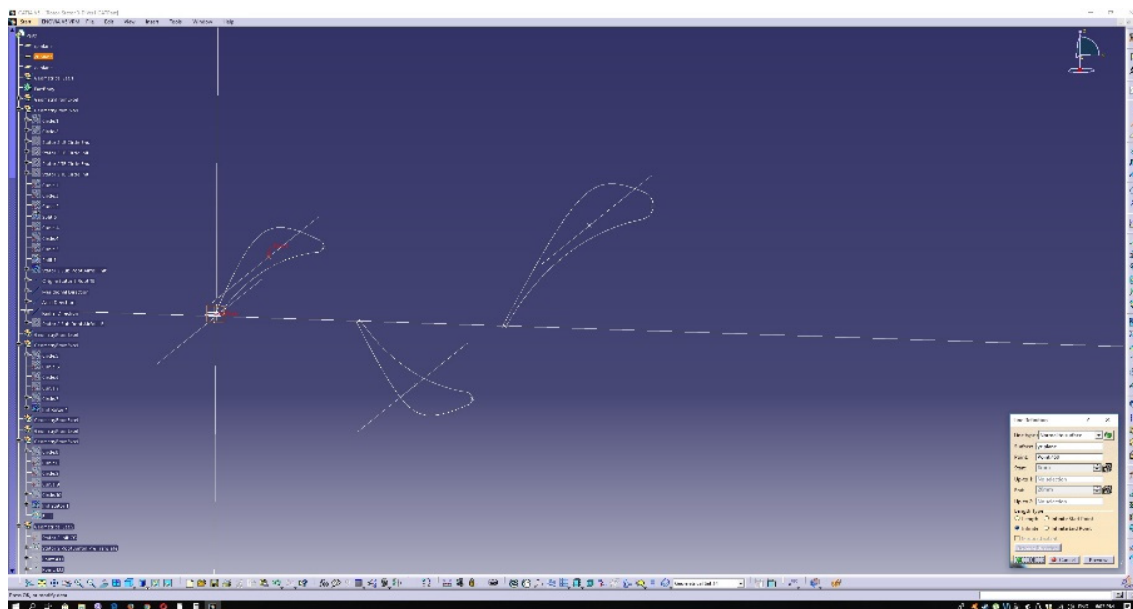


Figure 3.2.5: Airfoil stacking lines.

As previously stated, the 1<sup>st</sup> stage stator has no twist, taper or skew, so the only required step is to translate the existing airfoil in the direction of the stacking line far enough to achieve the desired blade height. At this point, it should be mentioned that the airfoils designed in the previous chapter are hub-height airfoils. Sub-hub airfoils must be created as well, so as the

design of the complete assembly is made easier. To achieve the initial airfoil's translation, the command "Translate" is used, as depicted below. This first translation is used to generate the tip airfoil.

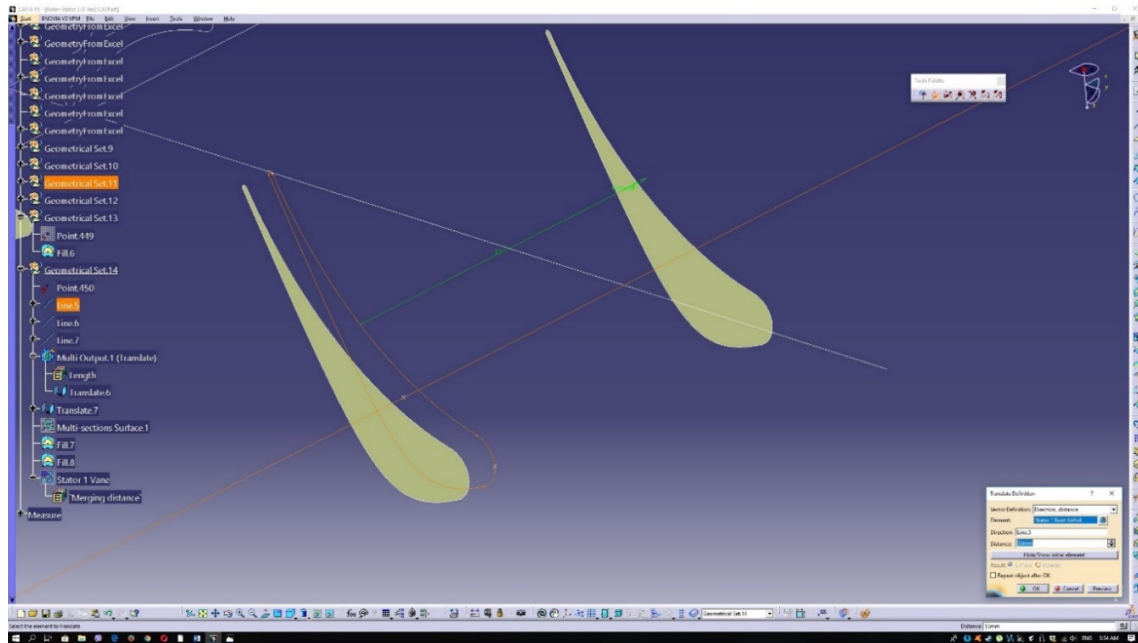


Figure 3.2.6: Airfoil translation.

The second translation is used to generate the sub-hub airfoil and is shown in Figure 3.2.7.

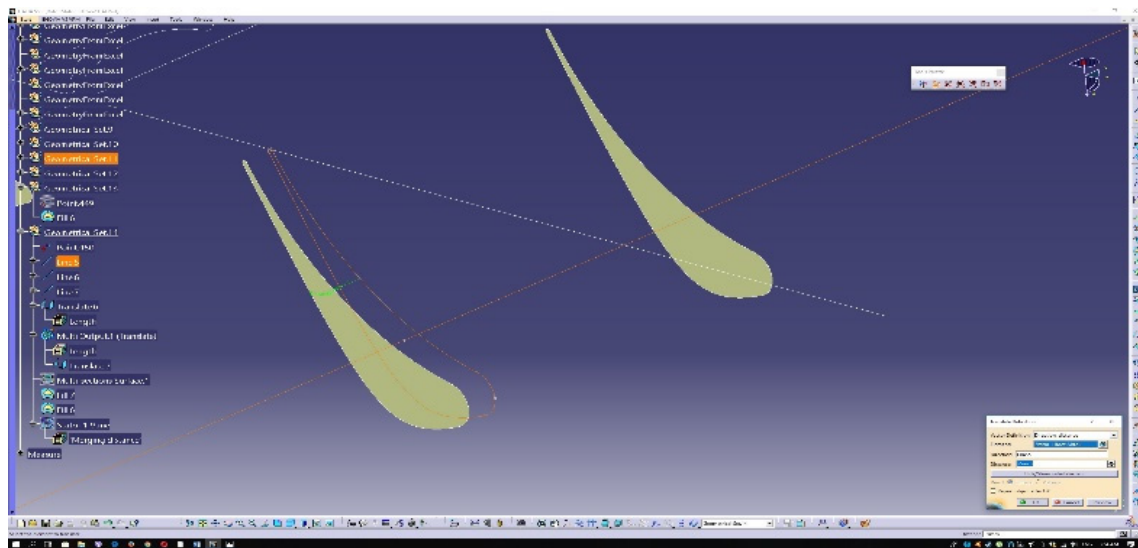


Figure 3.2.7: Airfoil translation below the hub.

To complete the first stage vane a volume representing it should be constructed. To achieve that the "Multi-Section Volume" command should be used from the "Insert" menu. After said selection the top and bottom airfoils should be chosen and a volume representing the vane will be generated. The above procedure is shown in Figure 3.2.8.

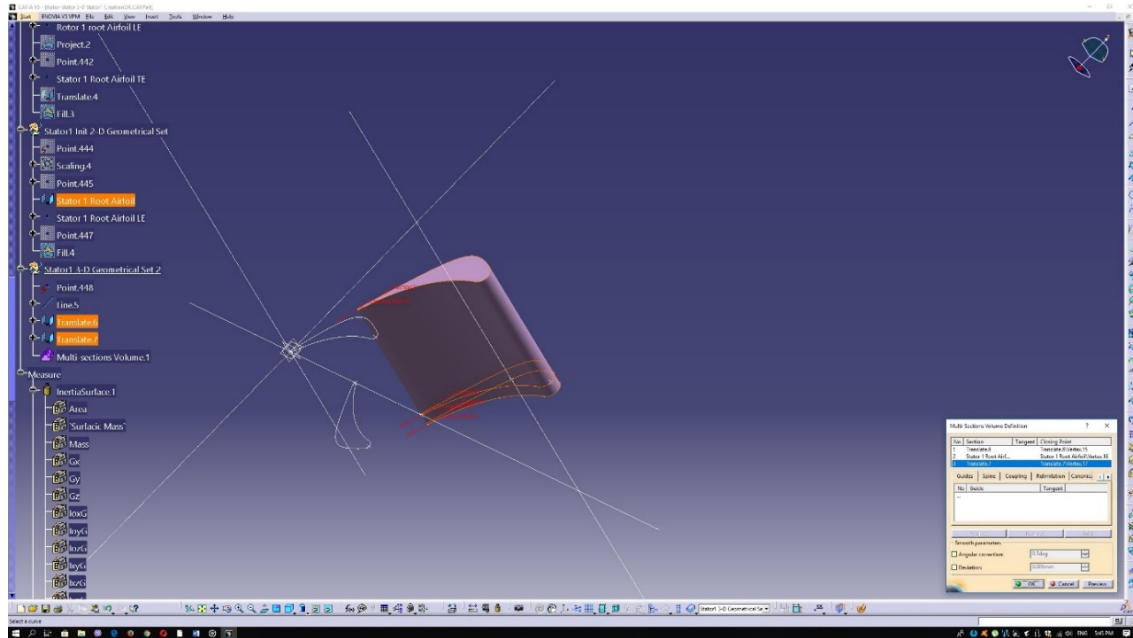


Figure 3.2.8: Creation of the 1st stg vane via multi sections volume.

A similar procedure is going to be followed for the creation of the rotor blade. The rotor airfoil, created in the previous section, is (similarly to the 1<sup>st</sup> stator) the root airfoil. A sub-root (sub-hub) and tip airfoils should be now generated. These two airfoils will be generated in the same manner as those for the 1<sup>st</sup> stator beforehand. So, the two airfoils are to be translated along the rotor's stacking line one towards the shroud (tip airfoil) and one below the hub (sub-hub airfoil).

Since, the rotor is chosen to have twisted blades, the two translated airfoils should now be rotated accordingly. The twist angle between the root airfoil and the tip airfoil is chosen to be  $11^\circ$  and linearly connected to the radial direction. The root airfoil is considered to be the reference ( $0^\circ$ ), hence the sub-root airfoil angle is to be defined. Considering the linear connection between the twist angle and the radial direction, the following relation is applied

$$\alpha = \frac{11}{45} r \quad (3.2.1)$$

where  $\alpha$  is the twist angle and  $r$  is the radial distance from the hub.

The distance of the sub-root airfoil from the hub is set to be  $5 \text{ mm}$  (or  $-5 \text{ mm}$  to be precise). Solving for  $\alpha$  we obtain  $\alpha = -1.2^\circ$ .

The figures below contain the complete set of information needed for the translations and rotations to take place.



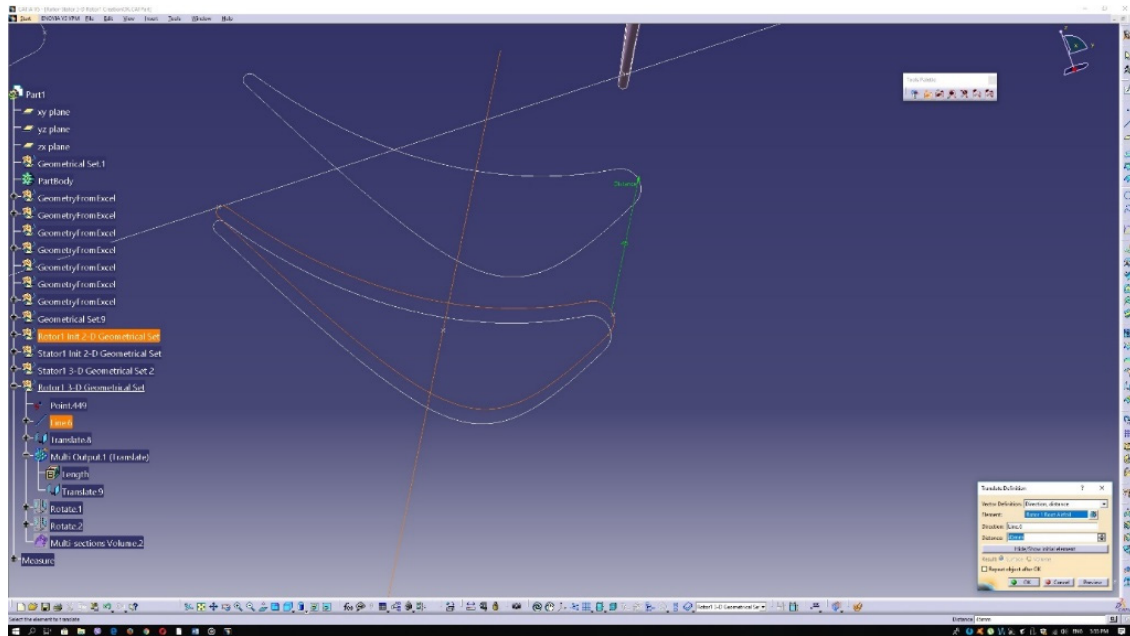


Figure 3.2.9: Rotor tip translation.

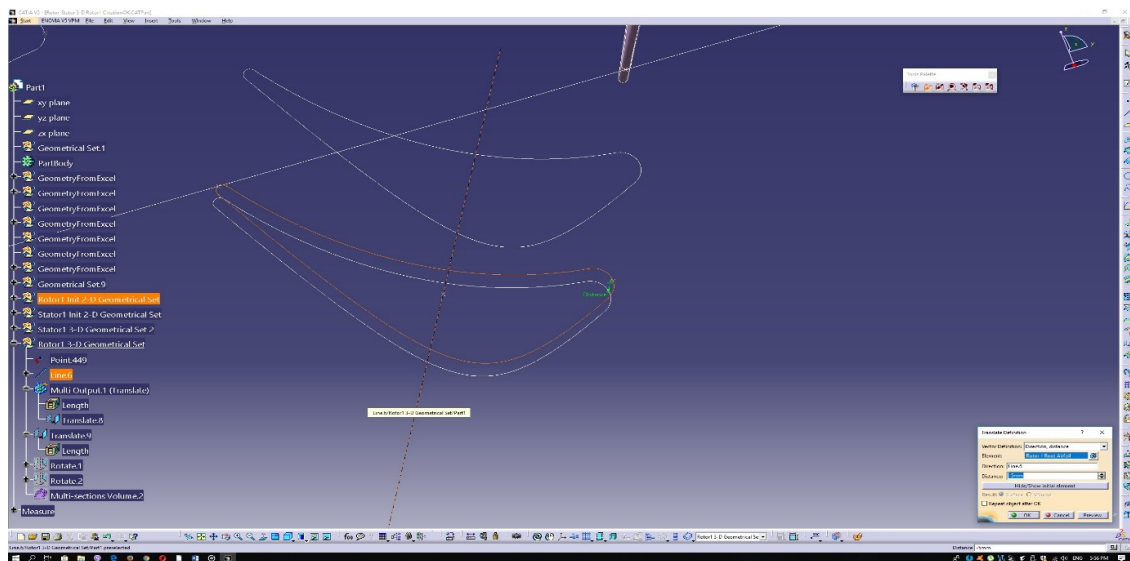


Figure 3.2.10: Sub-root airfoil translation.

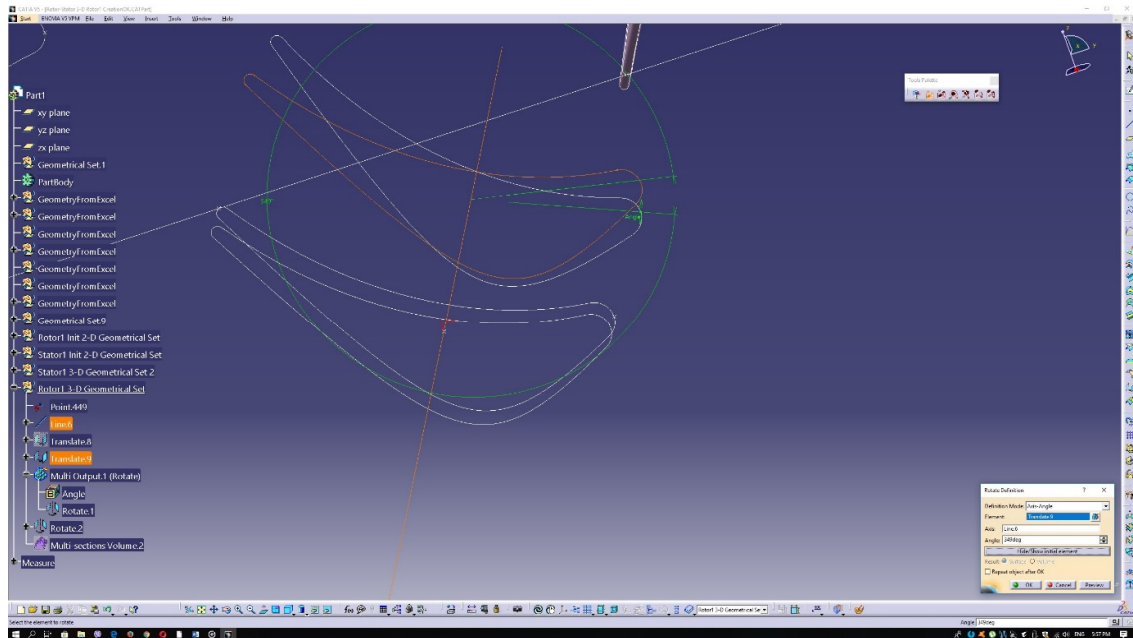


Figure 3.2.11: Rotor tip rotation.

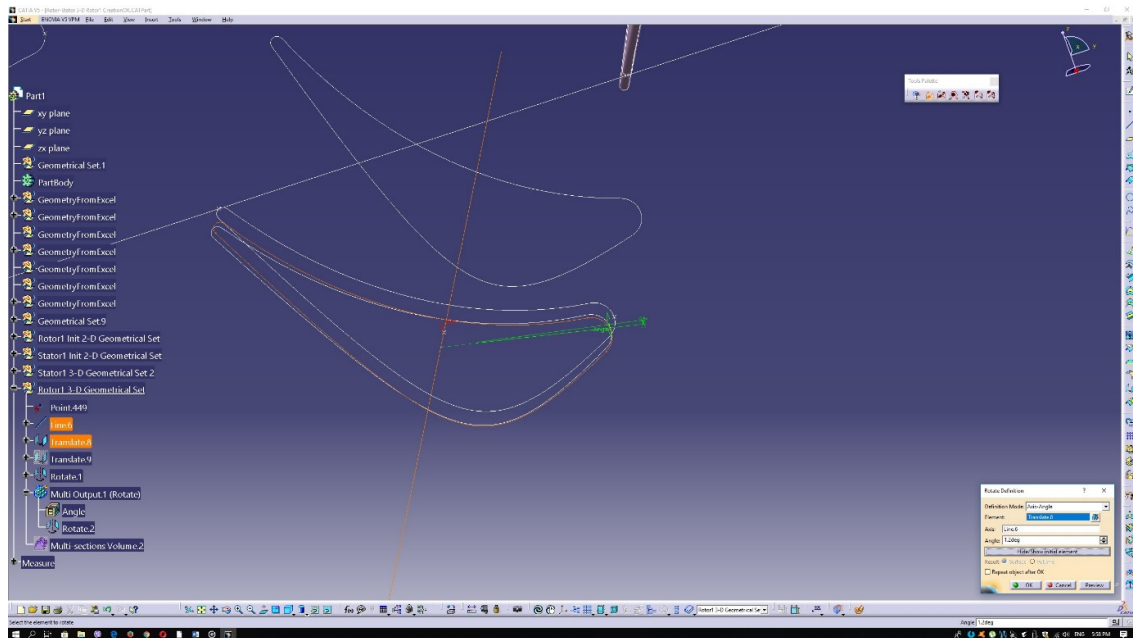


Figure 3.2.12: Rotor airfoil sub-root rotation.



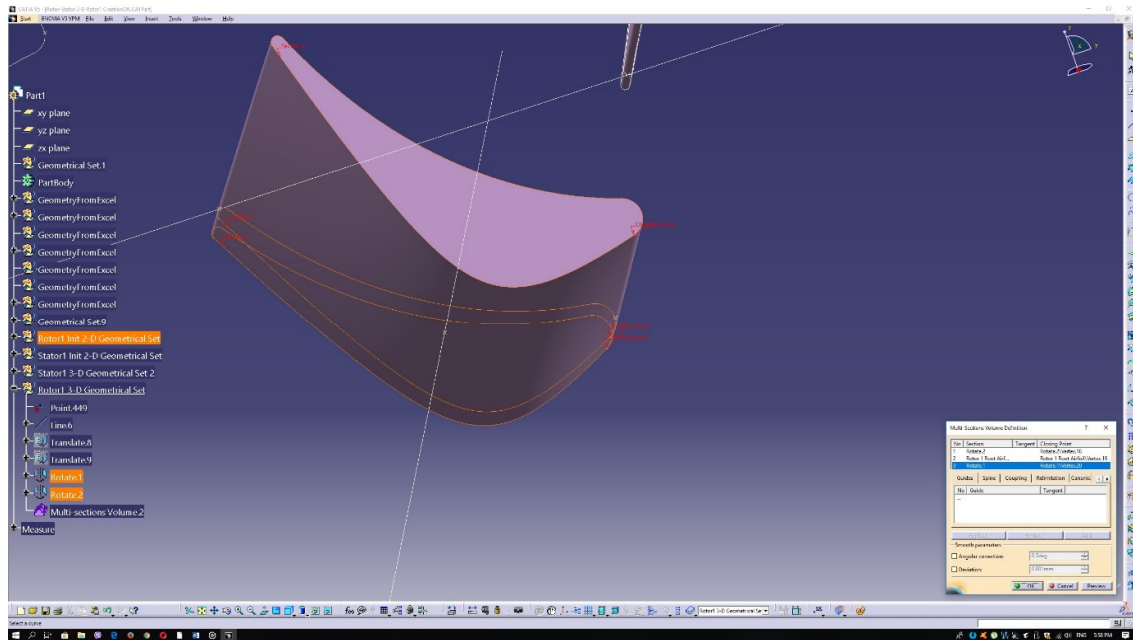


Figure 3.2.13: Multi section volume for the rotor.

The above concludes the rotor blade generation. What is left is the 2<sup>nd</sup> stator vane to be constructed further below. The 2<sup>nd</sup> stator vane is chosen to have taper, twist, and skewness as well. To achieve the vanes' twist, an identical to the rotor blades procedure will be followed. For the vane taper a scaling command will be used and for the skewness a conic will be used as a spine for the multi sections volume. First of all, the root airfoil should be translated to tip and sub-root radii.

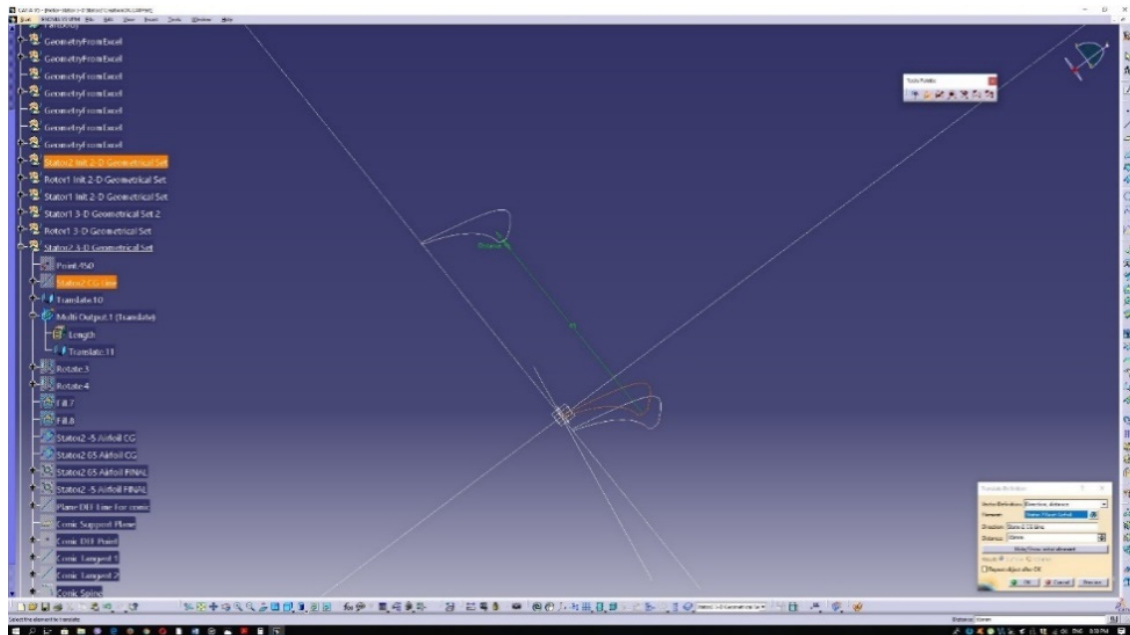


Figure 3.2.14: Second stage stator translate.

The same operation should be conducted for the sub-root airfoil. At this point the two airfoils are to be rotated accordingly. Same as the rotor, a linear, with regards to the radial distance from the hub, relation between blade height and chord is selected. Furthermore, the root to tip twist angle is set to be  $10^\circ$ . The new linear relation between the twist angle and the radial distance is

$$\alpha = \frac{10}{55}r. \quad (2.2.2)$$

Using Eq. (2.2.2), the sub-root twist angle should be  $-0.9^\circ$ . The “Rotate” command should be used on each of the translated airfoils. Said airfoils will be rotated around the previously defined stacking line of the 2<sup>nd</sup> stator. The figure below (Fig. 3.2.15) demonstrates the followed procedure.

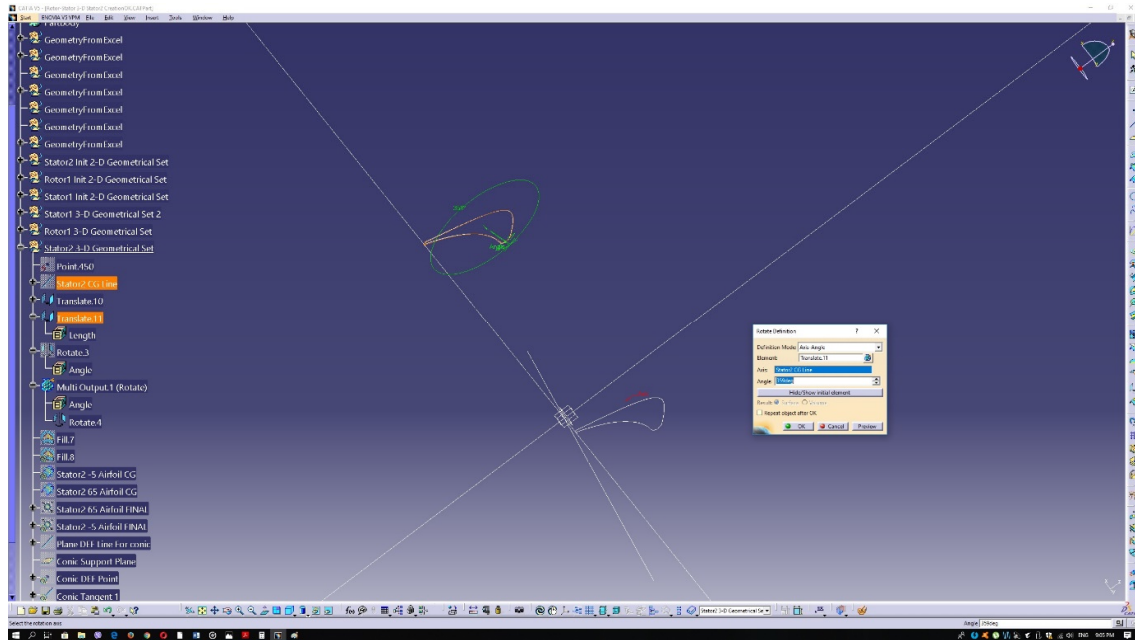


Figure 3.2.15: Second stator tip airfoil rotation.

The same should be followed for the sub-root airfoil. The now rotated airfoils should be scaled in order to achieve the desired taper of the 2<sup>nd</sup> stage vane. In order to scale the airfoils, the variation of their chord vs the radial distance is needed. The following formula represents the chord vs the radial height.

$$c = 0.216r + 33.247 \quad (2.2.3)$$

According to (2.2.3) the root, sub-root and the tip airfoil should have the following chords:

$$c_{sub-root} = 32.167 \text{ mm}$$

$$c_{tip} = 47.287 \text{ mm}$$

$$c_{root} = 33.247 \text{ mm}$$

In order to scale the airfoils, a scale factor is needed. The scale factor is defined to be the ratio of the chord of the airfoil to be scaled to the reference airfoil's chord (root airfoil). Thus, the two scale factors are as follows

$$\frac{c_{tip}}{c_{root}} = 1.422,$$

$$\frac{c_{sub-root}}{c_{root}} = 0.967.$$

Having the scale factor calculated, the “Scale” command is then used. At this stage the rotated airfoils have the same length with the root-reference airfoil so they can be used as the reference element for each scaling. The figure below (Fig. 3.2.16) demonstrates the selections that need to be made in order to have the airfoils scaled.

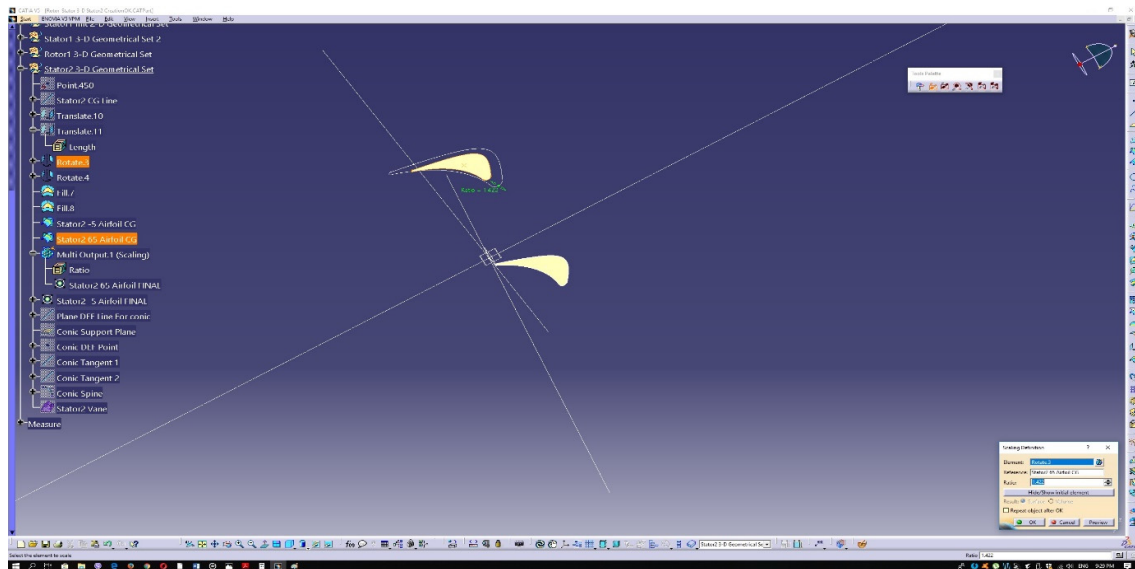


Figure 3.2.16: Stator tip airfoil scale.

The same process applies for the scaling of the sub-root airfoil. Now the vane skewness is left to be determined. To realize that, a conic should be created. First, a new plane should be defined. The new plane will be created using two lines. The first line is the stator stacking line, which is already defined, while the second one will be a line perpendicular to the  $xy$  plane that passes from the CG of the tip airfoil. Using the “Plane” command and selecting the “Through two lines” option- with the two lines being the ones defined above- the plane is generated. The figure below (Fig. 3.2.17) demonstrates the aforementioned procedure.

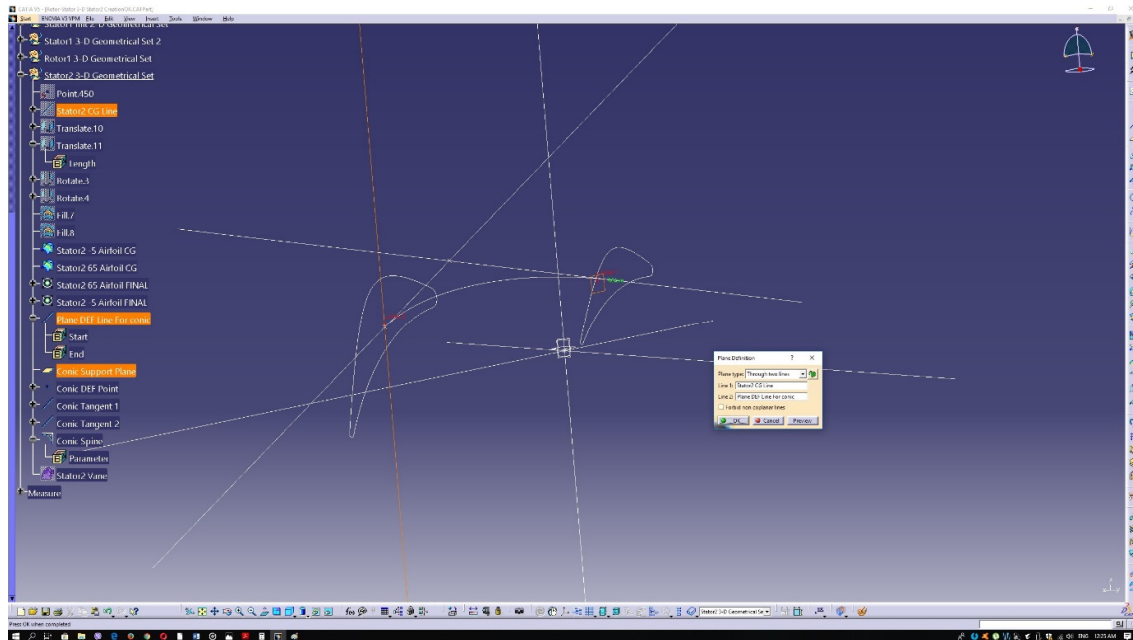


Figure 3.2.17: Plane for conic support.

The conic needs two tangents to be well-defined. First, we define a point on the plane, created beforehand. This point will define the tangents slope and as a result the conic's shape. After that, the two lines are generated, using as starting point the CG of each airfoil respectively, and as a common end point the conic definition point. As a result, those two lines will rest on the plane created previously.

Finally, the conic itself will be defined. The above lines will be used as tangents, the plane previously generated will act as the conic support and what remains to be defined is the conic parameter. A parameter of 0.45 was selected. The following figures depict the procedure.

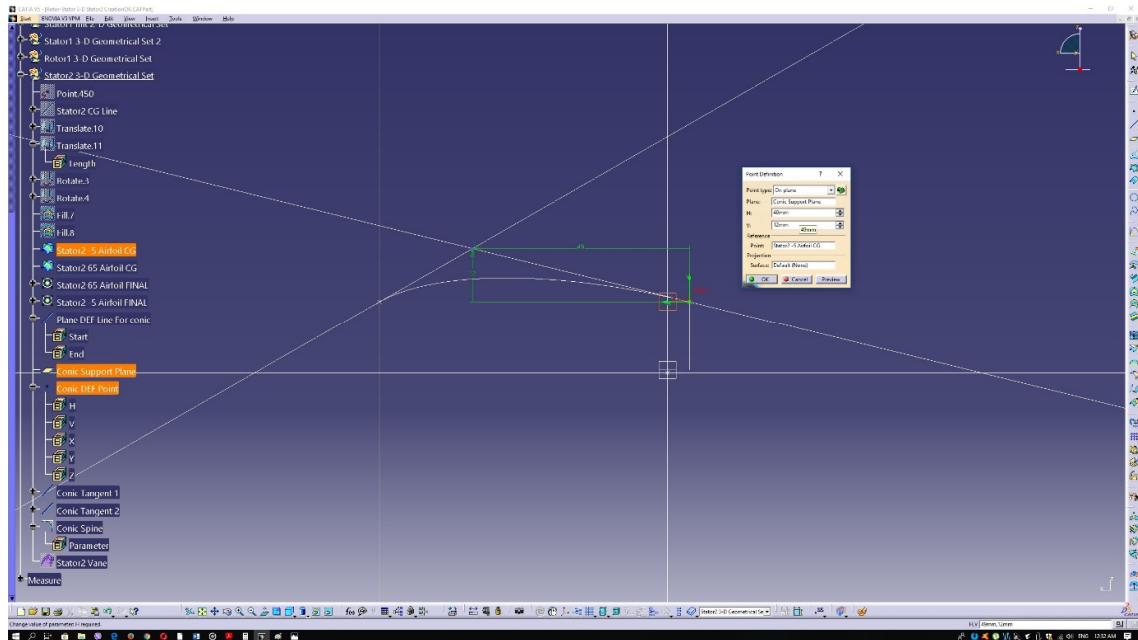


Figure 3.2.18: Conic definition point.

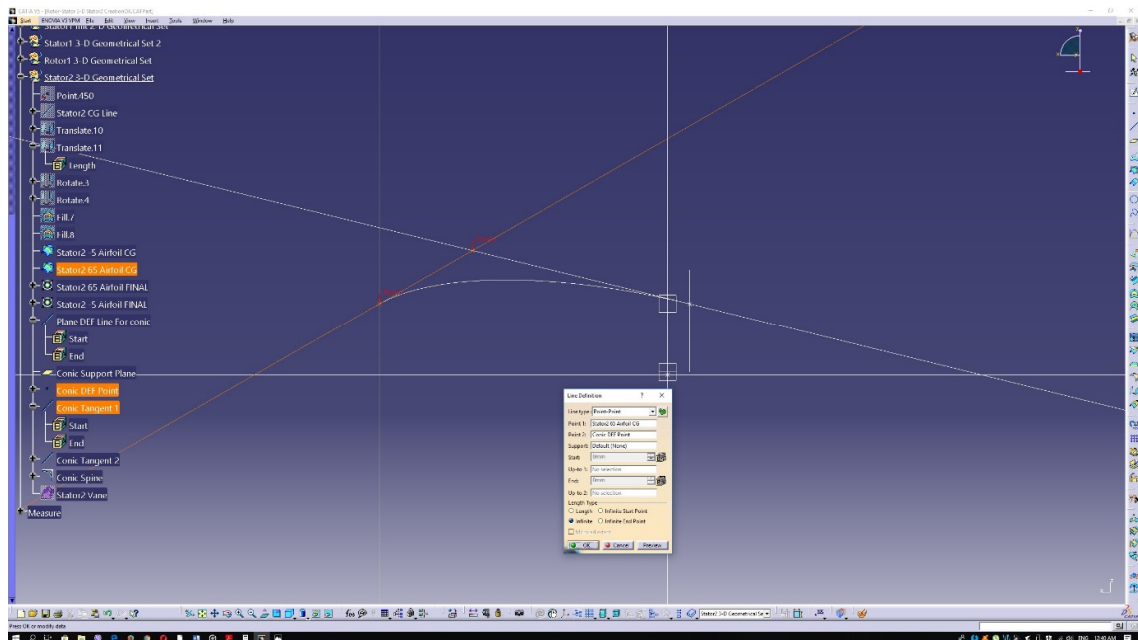


Figure 3.2.19: Conic tangent 1.

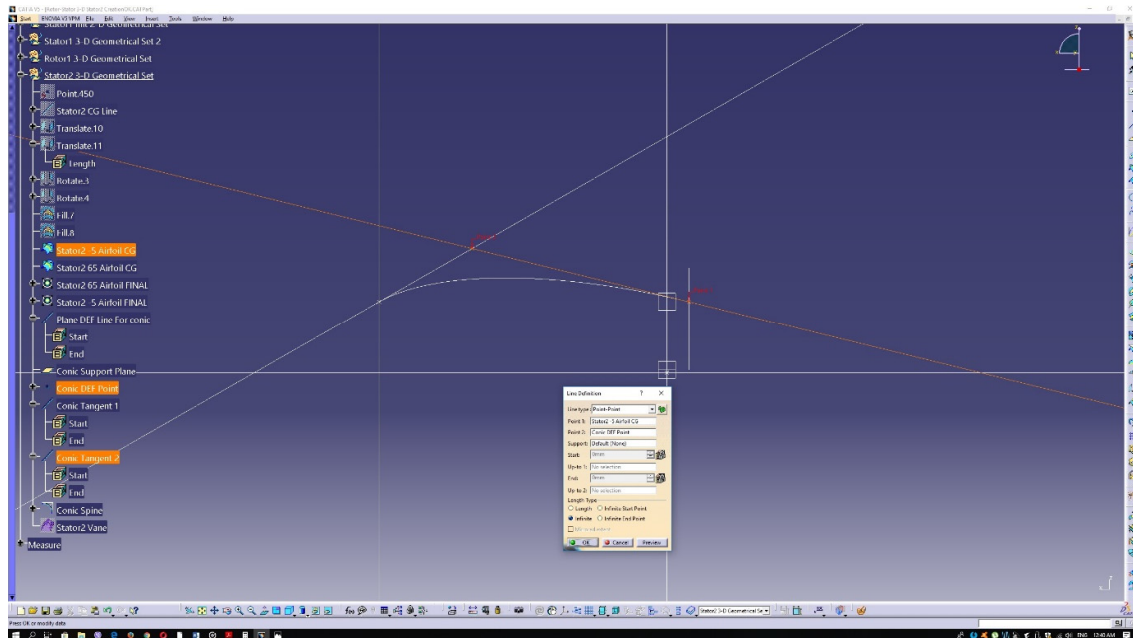


Figure 3.2.20: Conic tangent 2.

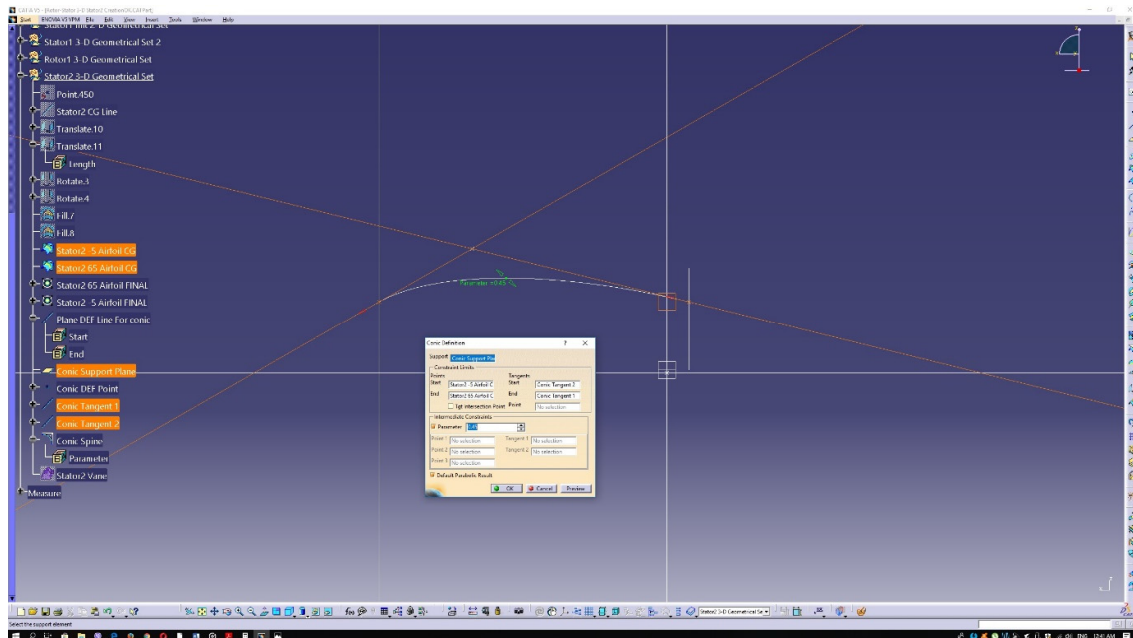


Figure 3.2.21: Conic definition.

As the spine is now available, the “Multi sections volume” command should be selected using the sub-root and tip airfoils, while the conic acts as a spine. Figure 3.2.22 below describes the procedure.



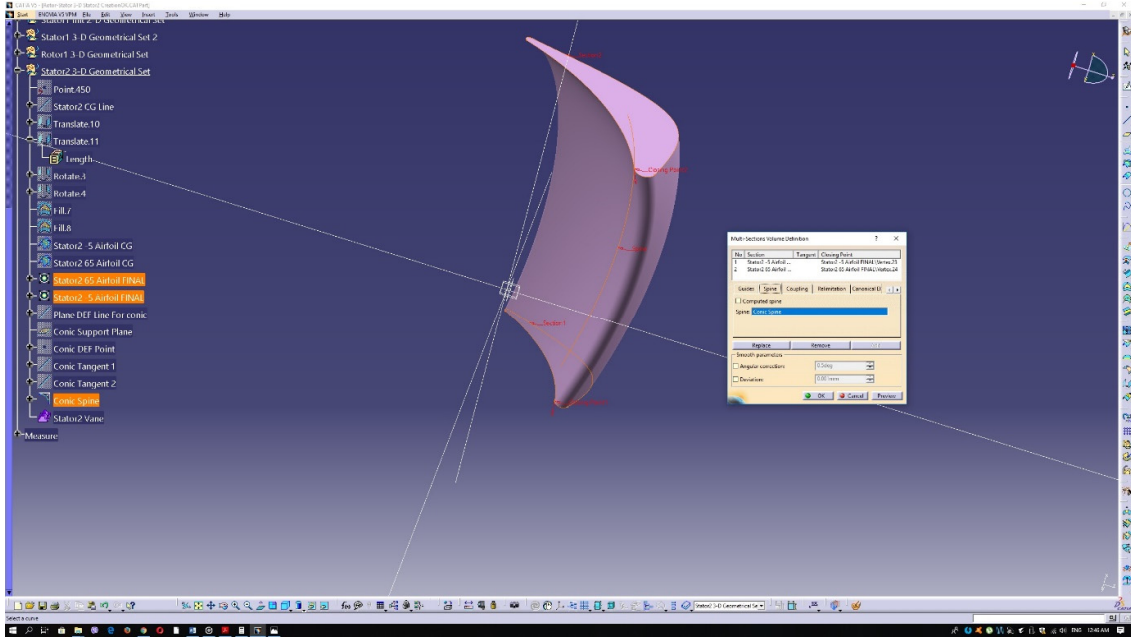


Figure 3.2.22: Second stator multi-sections volume.

At this point the 1<sup>st</sup> and 2<sup>nd</sup> stator vanes, as well as the rotor blade, are all represented complete as shown in Figure 3.2.23 below.

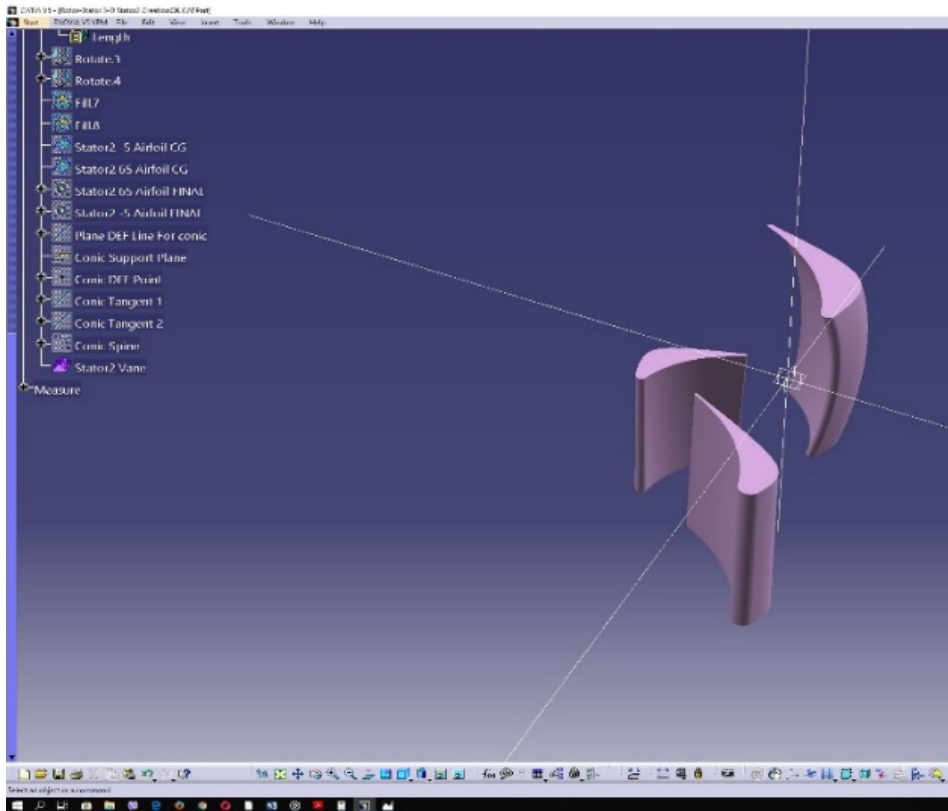


Figure 3.2.23: Rotor blade and stator vanes.

### 3.3 3D Design of the Complete Turbine

In order to create the complete turbine, the turbine hub and shroud should be generated. To create the hub and the shroud, two profiles should be defined and then revolved around a revolution axis (the axis of symmetry). The hub's profile will be a line segment spanning from the turbine inlet to the turbine outlet. The shroud's profile will be a polyline. The turbine inlet and outlet should be sufficiently far from the 1<sup>st</sup> stator and 2<sup>nd</sup> stator, respectively in order to allow for a safe application of the relevant boundary conditions. Figure 3.3.1 below contains the shroud and hub profiles, as well as the revolution axis, around which these will revolve.

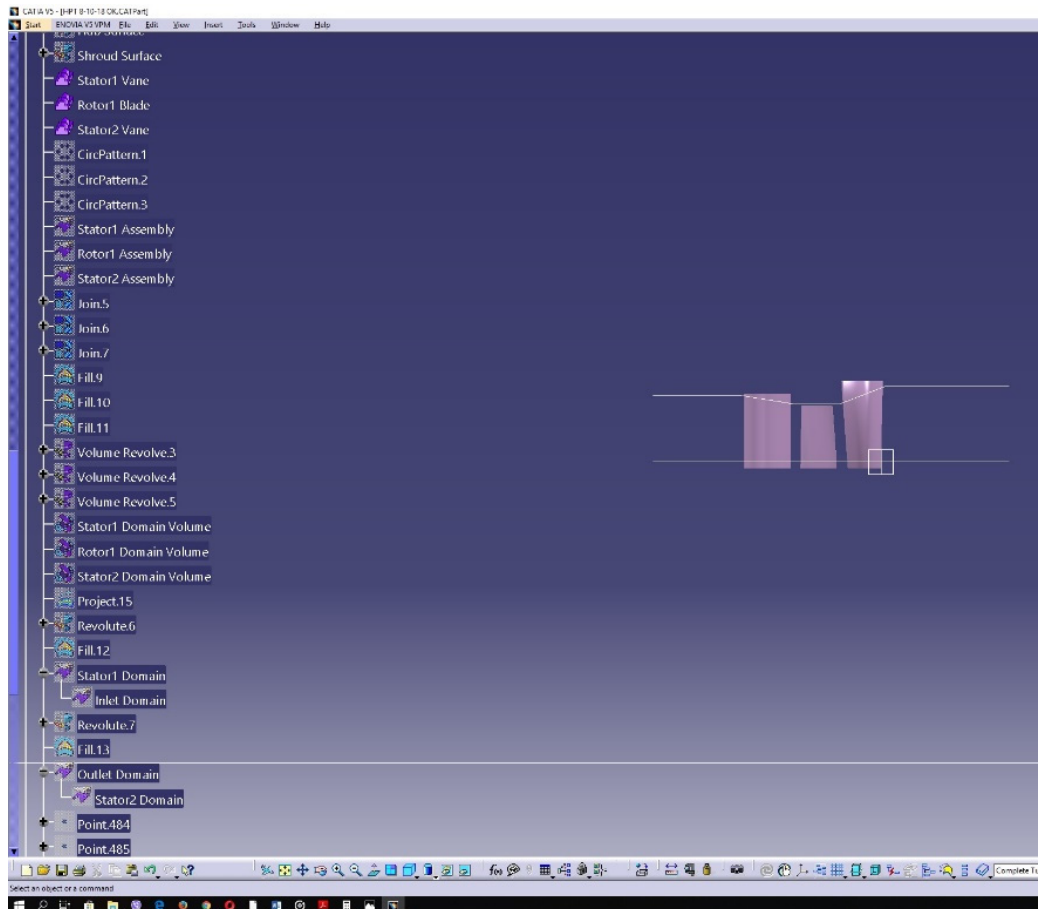


Figure 3.3.1: Hub/shroud profiles and the revolution axis.

In order to revolve the two profiles around the revolution axis the command “Revolve” will be used as shown in Figures 3.3.2 and 3.3.3 below.



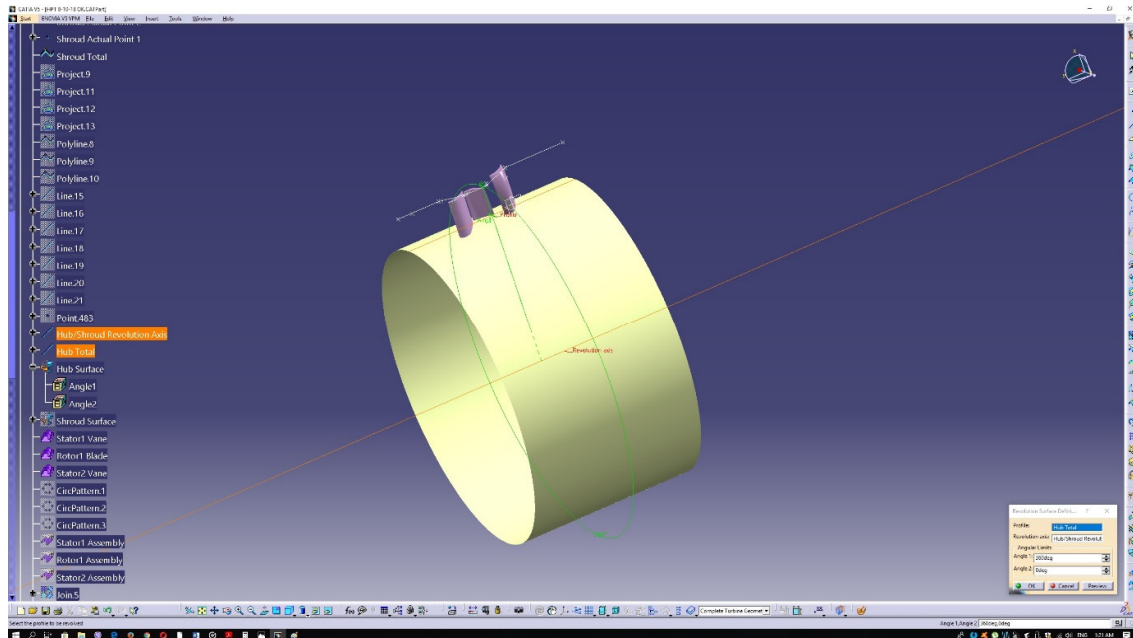


Figure 3.3.2: Hub revolution.

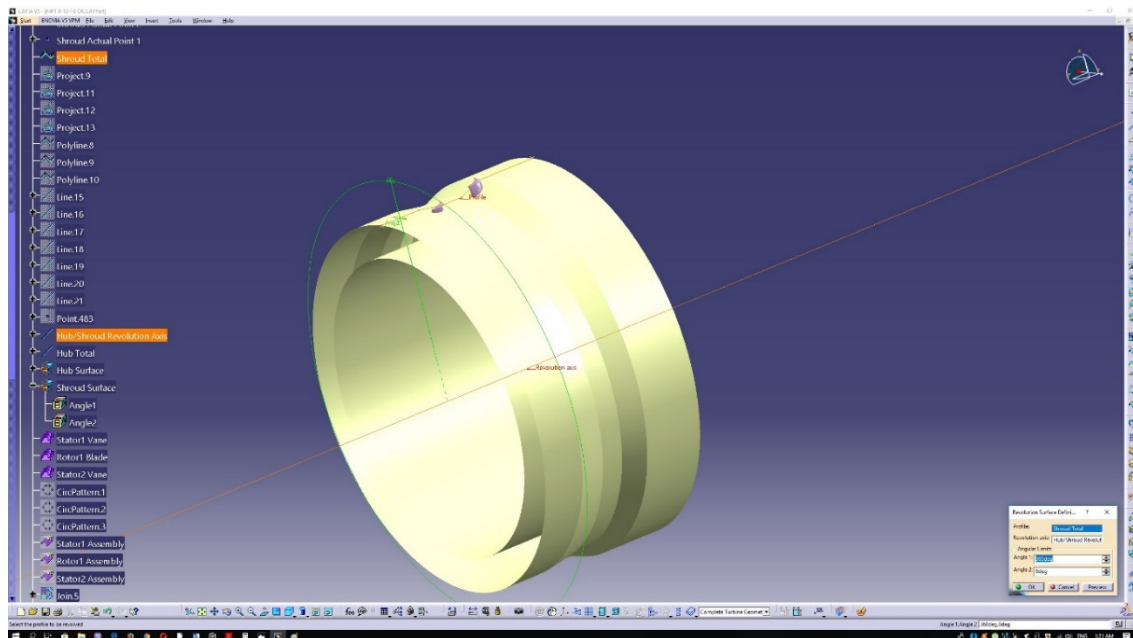


Figure 3.3.3: Shroud revolution.

Now the blade and vanes will be patterned around the hub to create complete assemblies. To achieve that, the blade and vanes, as objects, should be under the same Geometrical Set. This is done by right clicking on each of them on the selection tree. Then the "<object name> object" must be selected at the bottom of the drop menu and then the "Change Geometrical Set" command should be applied. Figure 3.3.4 describes the above procedure.

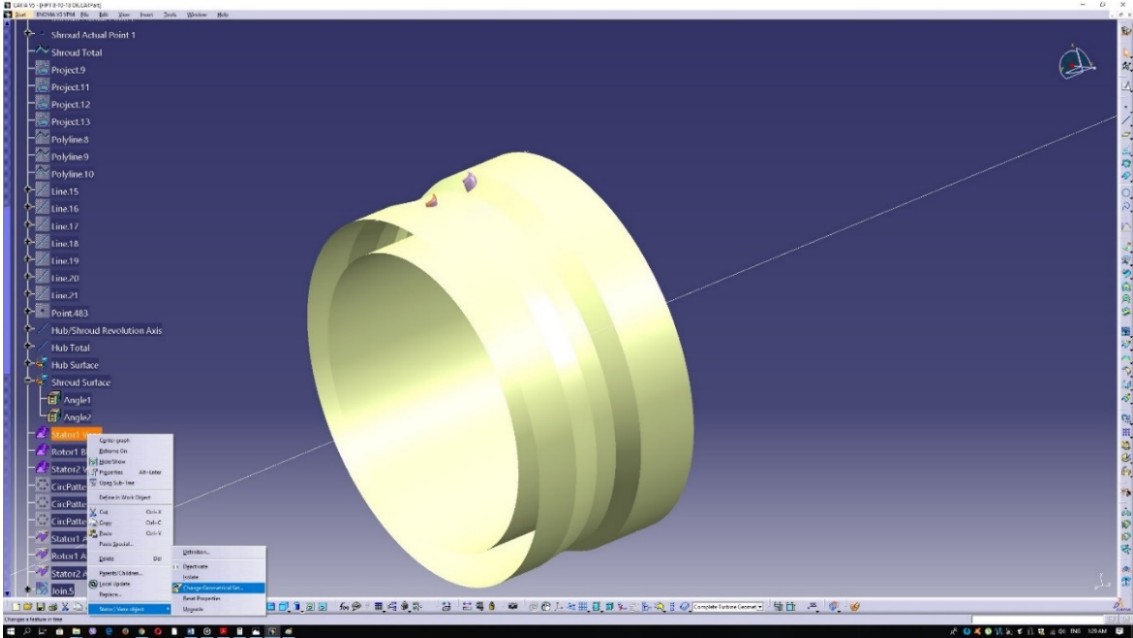


Figure 3.3.4: Changing the geometrical set.

Moving forward, the “Circular Pattern” command is to be used as in Figure 3.3.5.

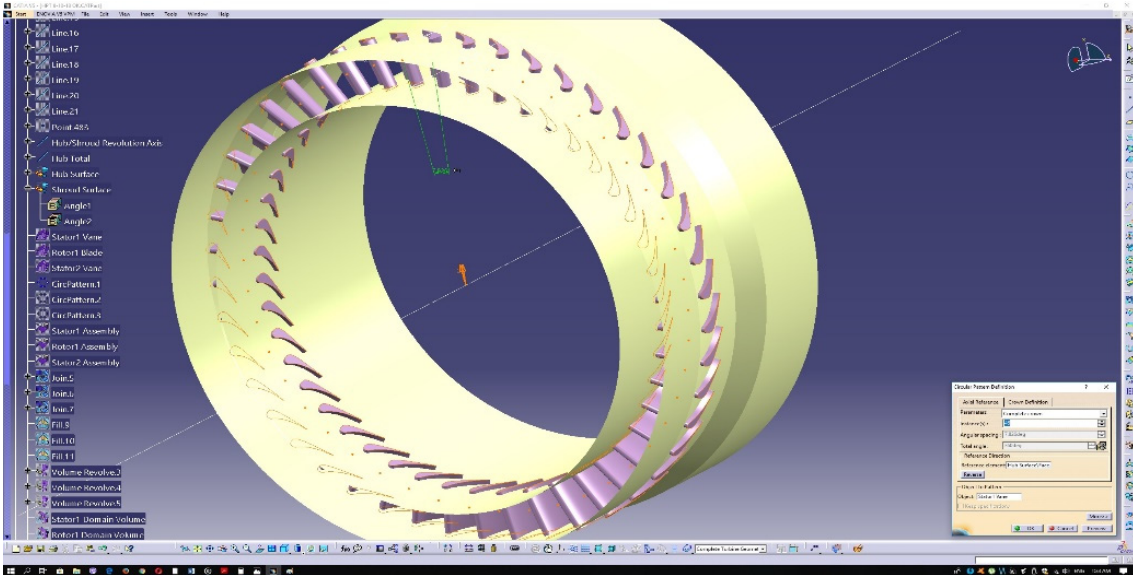


Figure 3.3.5: Circular pattern.

The same procedure should be applied for the rotor and the second stator. Now, the parts of the blades and vanes protruding from the shroud and hub surfaces should be trimmed. To do this, the “Split” command is used, as in Figure 3.3.6.

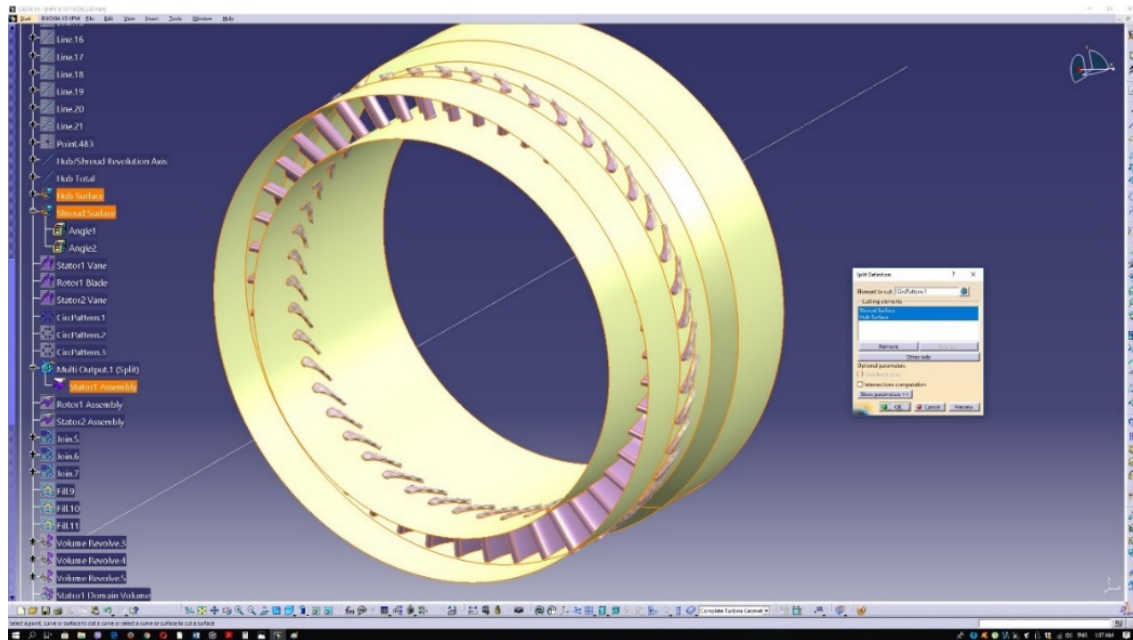


Figure 3.3.6: Split operation.

The same procedure is applied for the rotor and the second stator. At this point five volumes should be created via revolution, from whose domains the stages of blades and vanes will be removed via Boolean subtraction. To do that the hub and shroud profiles should be revisited and modified. The total hub-shroud profile will be divided into five parts that are to be filled in order to represent surfaces. Those surfaces will act as the profiles to be revolved, in order to generate the desired volumes.

First, the hub-shroud profile needs to be segmented. The points that were used to create the shroud polyline, will now be projected on the hub profile itself. Next, straight line segments will be drawn from the original points to their projections. The following figures depict the above procedure.

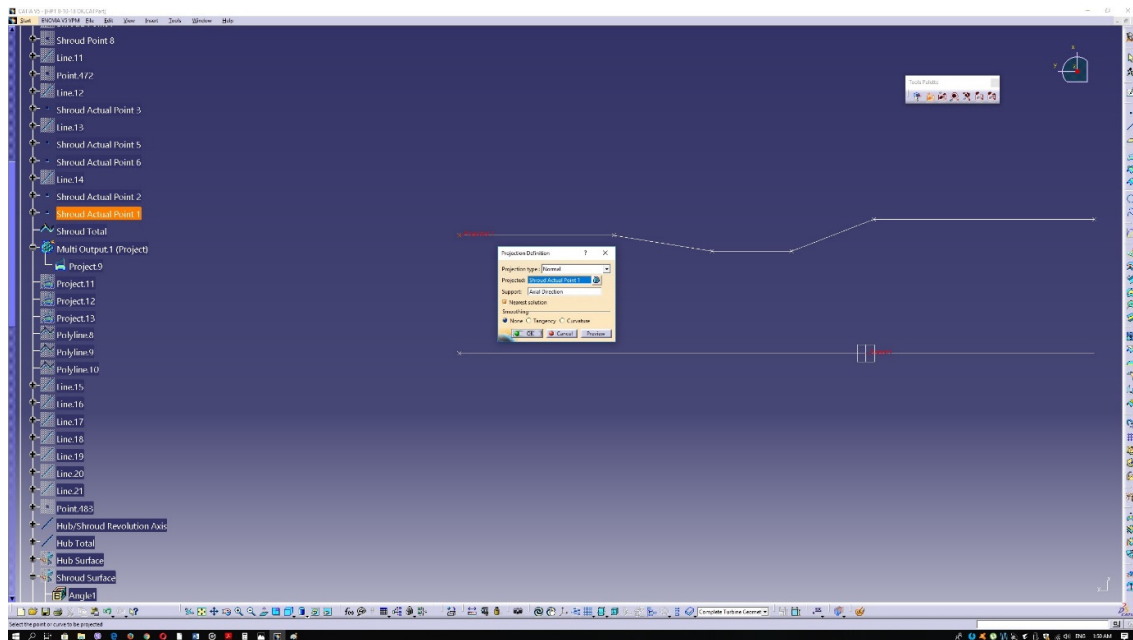


Figure 3.3.7: Point projection onto hub profile.

The same goes for the rest of the shroud profile points.

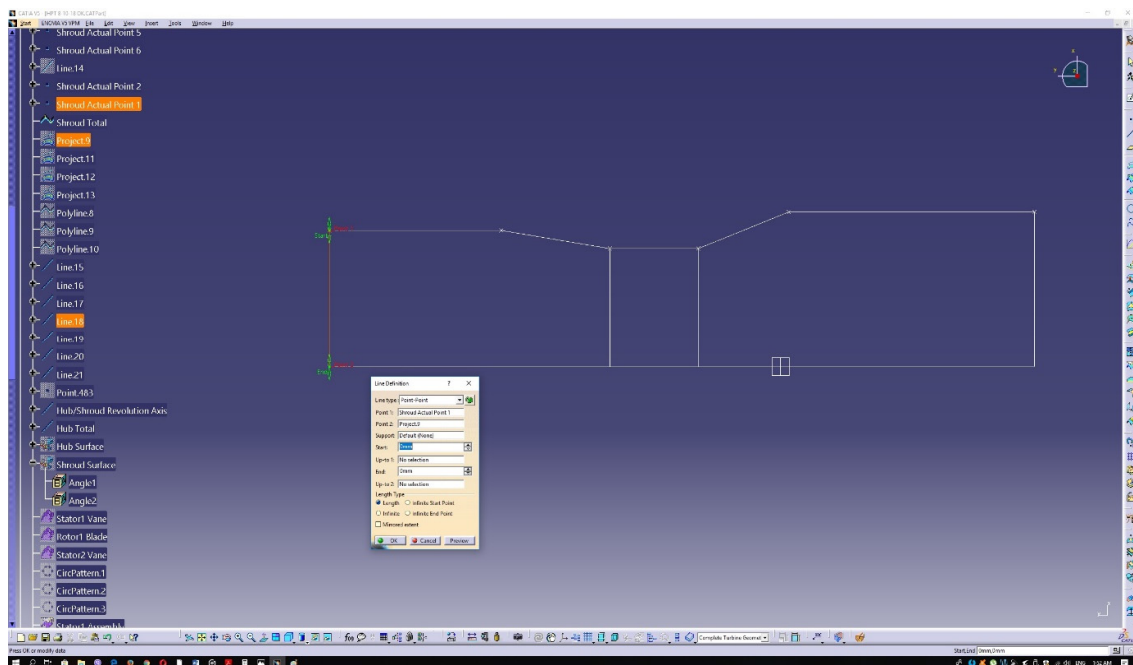


Figure 3.3.8: Hub shroud segments.

Now the separate line segments should be joined together in order to form closed contours. This is achieved via the “Join” command. After that, each separate segment is filled with the “Fill” command in order to represent a surface.

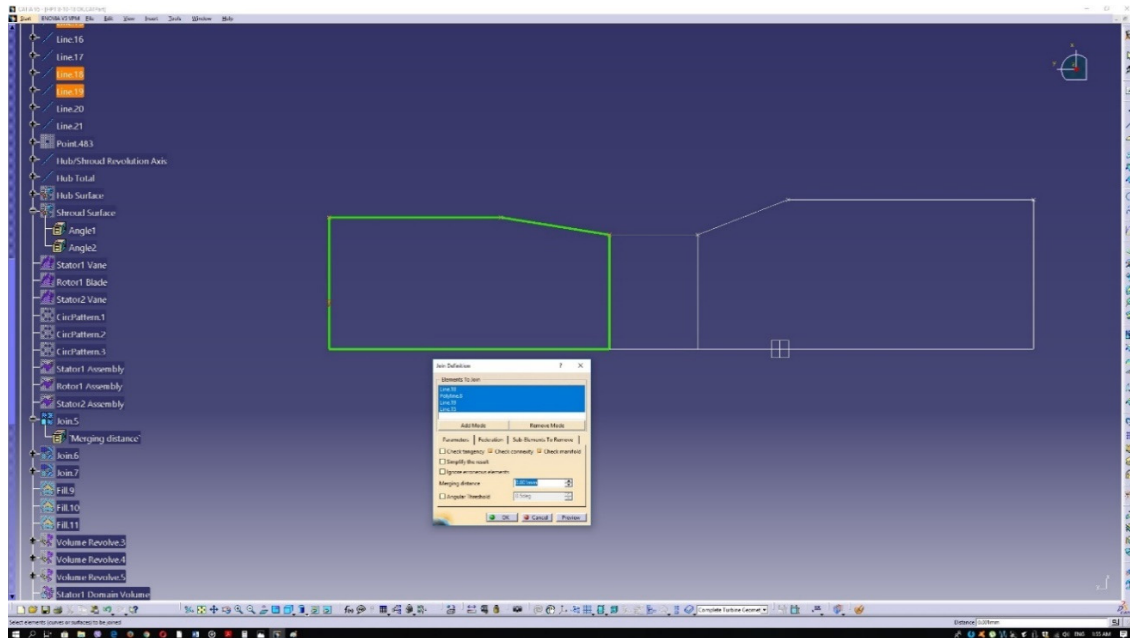


Figure 3.3.9: Hub shroud profile join.

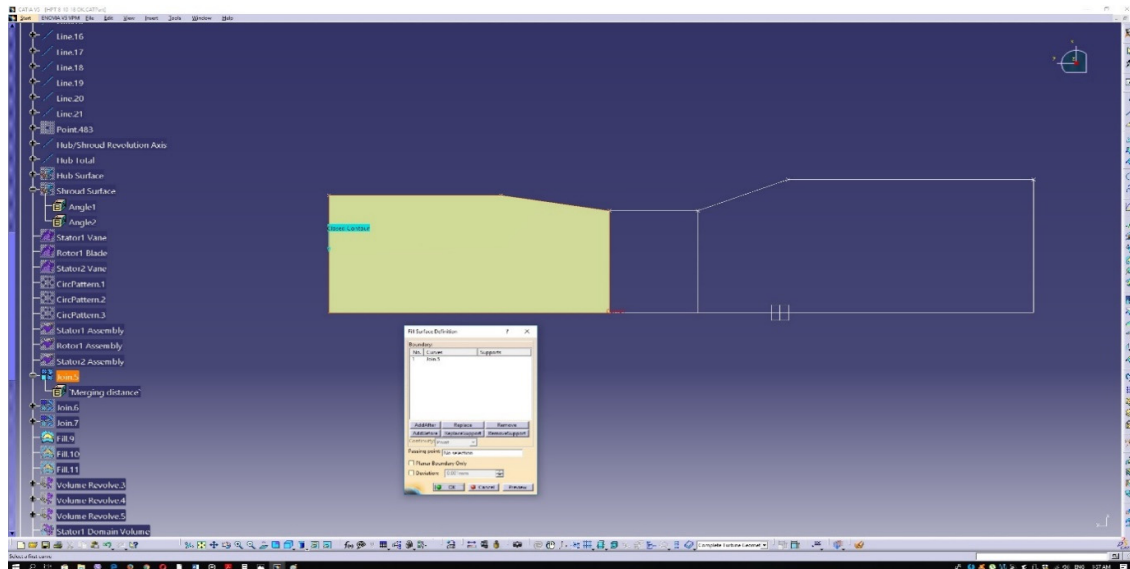


Figure 3.3.10: Segment fill.

Now, each surface profile should be revolved around the revolution axis in order to generate a volume of revolution.



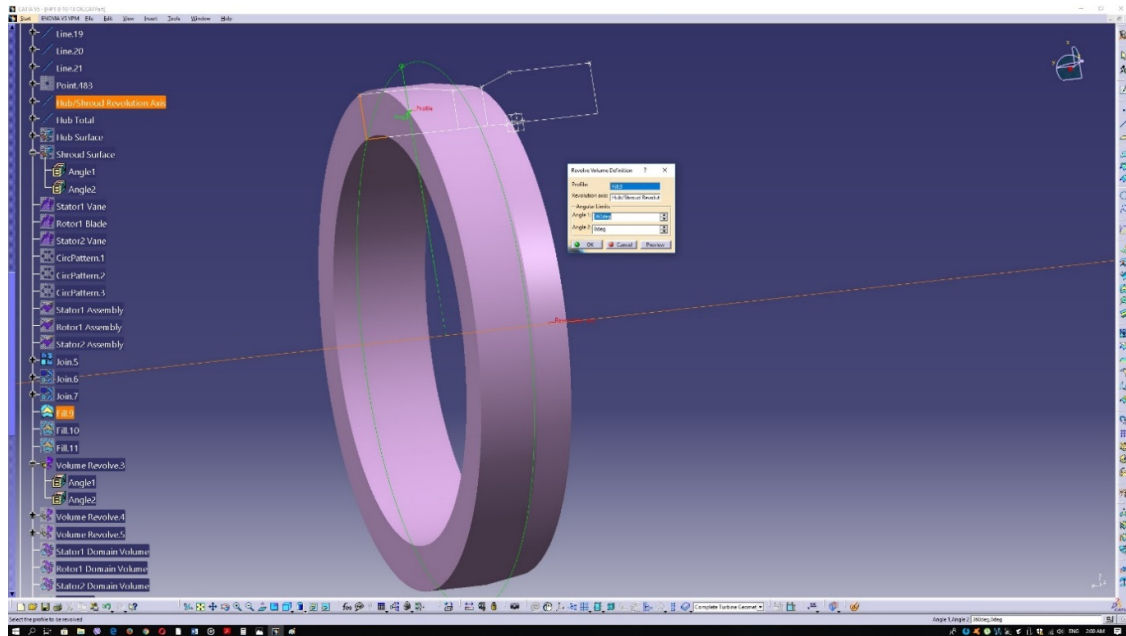


Figure 3.3.11: The resulting volume of revolution.

Having done that for every profile, we get the following volumes (Fig. 3.3.12).

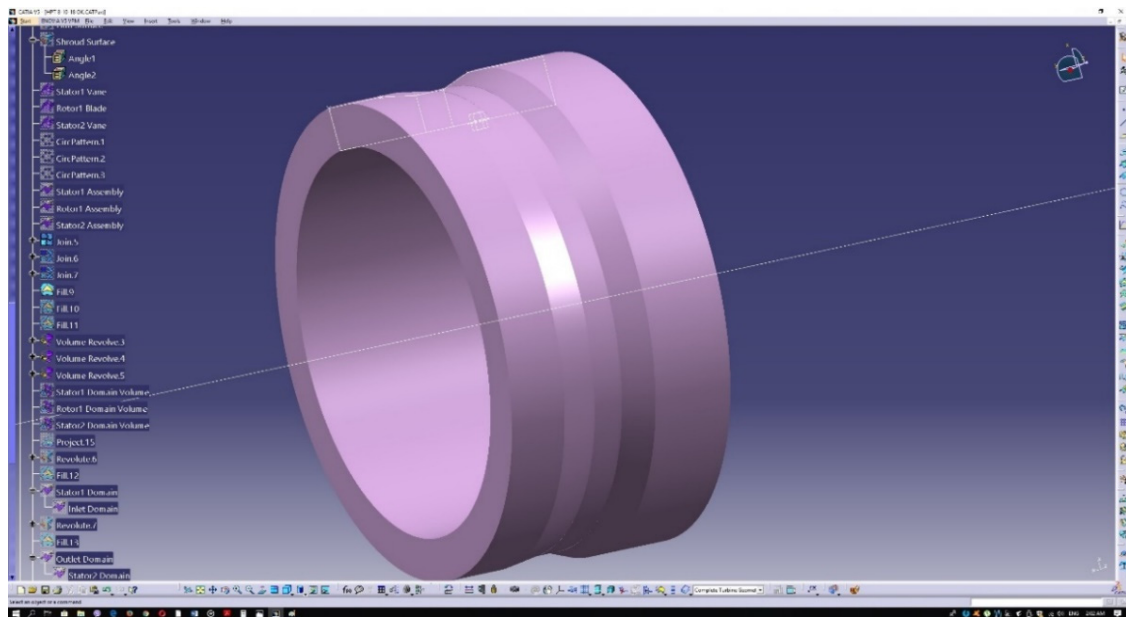


Figure 3.3.12: Revolution of all three segments.

Now the first and last volumes of revolution should be divided, in order to obtain a separate domain for the inlet and the outlet. A circle is created by revolving the second shroud point and then filled to create a surface. That surface is then used to split the initial domain into two separate ones.

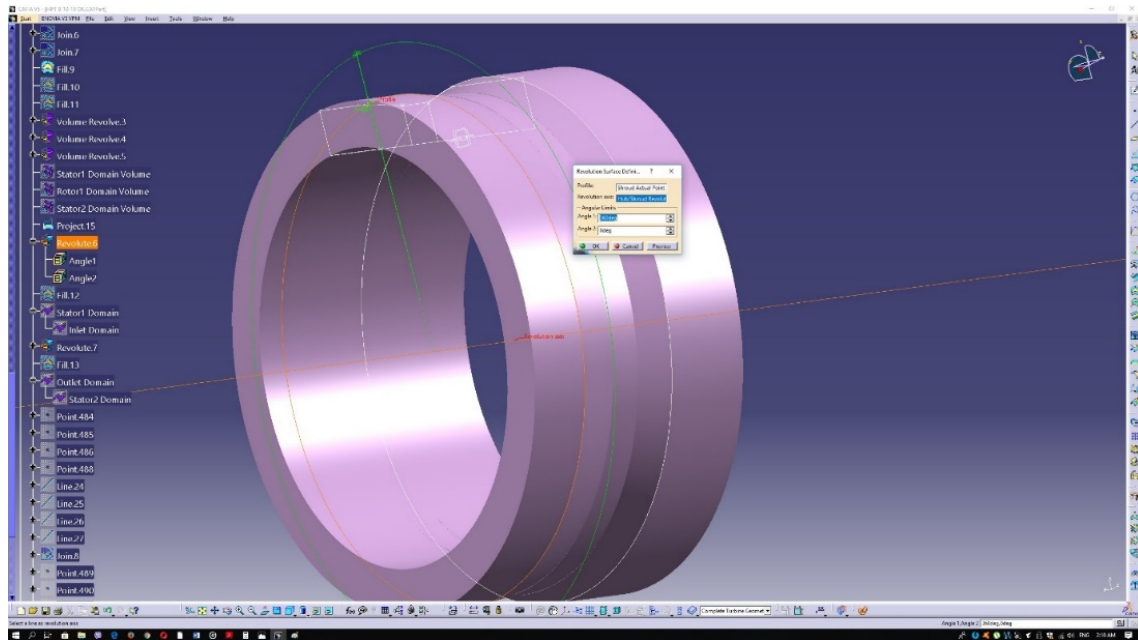


Figure 3.3.13: Circle from revolution.

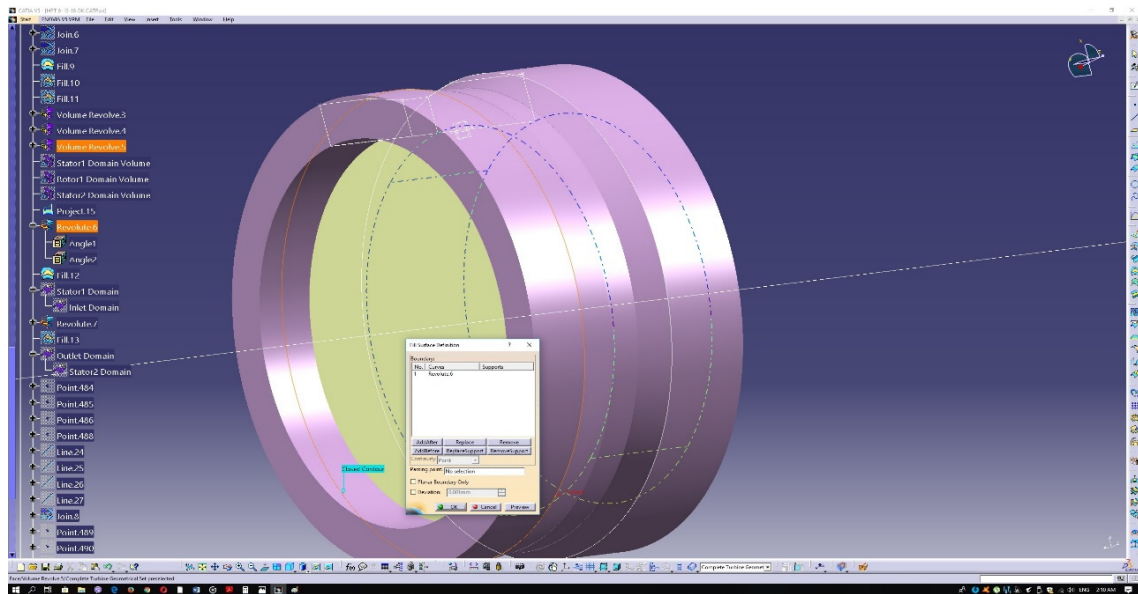


Figure 3.3.14: Circle fill.

The same applies for the second volume's domain. Now a Boolean subtraction should be implemented in order to remove the blades and vanes encompassed within the five volumes. To achieve that, the following path should be taken: "Insert" → "Volumes" → "Remove...". Then, on the emerging window the operators should be chosen, as shown in the following Figure 3.3.15.

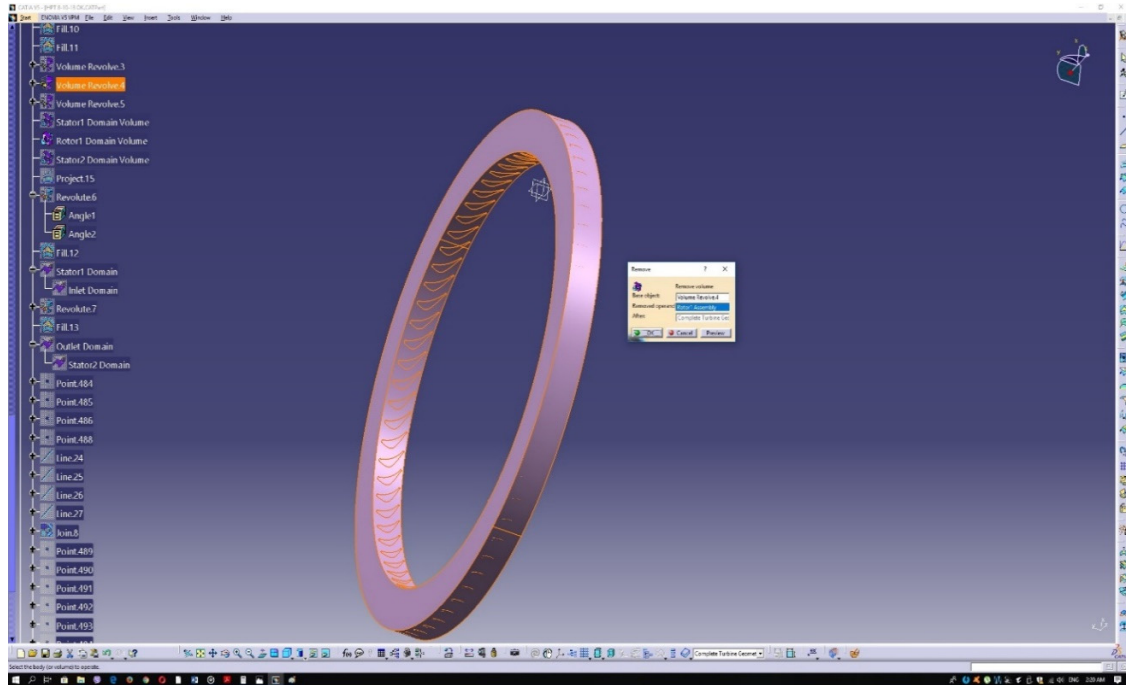


Figure 3.3.15: Boolean operation for the rotor.

As before, the same procedure applies for the first and second stators. One last step is required in order to complete the design process. Even though the turbine's actual domain is completed, one additional supporting volume should be added (to control the grid density at the rotor tip clearance region).

The corresponding volume should be a ring of relatively small thickness that will start outside of the rotor's domain and eventually merge with it in such a way that the rotor shroud and rotor blade tips are contained. To achieve that, an additional surface profile should be created. Said profile should have a rectangular shape, which will be subsequently revolved in order to produce the desired ring.

First, four points should be defined that will outline the rectangular segment. Those four points are to be connected with lines and have those lines joined in order to create a closed contour. The contour is then filled, creating the surface profile to be revolved. Then, the profile will be revolved around the common revolution axis, used in the steps above. The figures below depict the followed procedure.



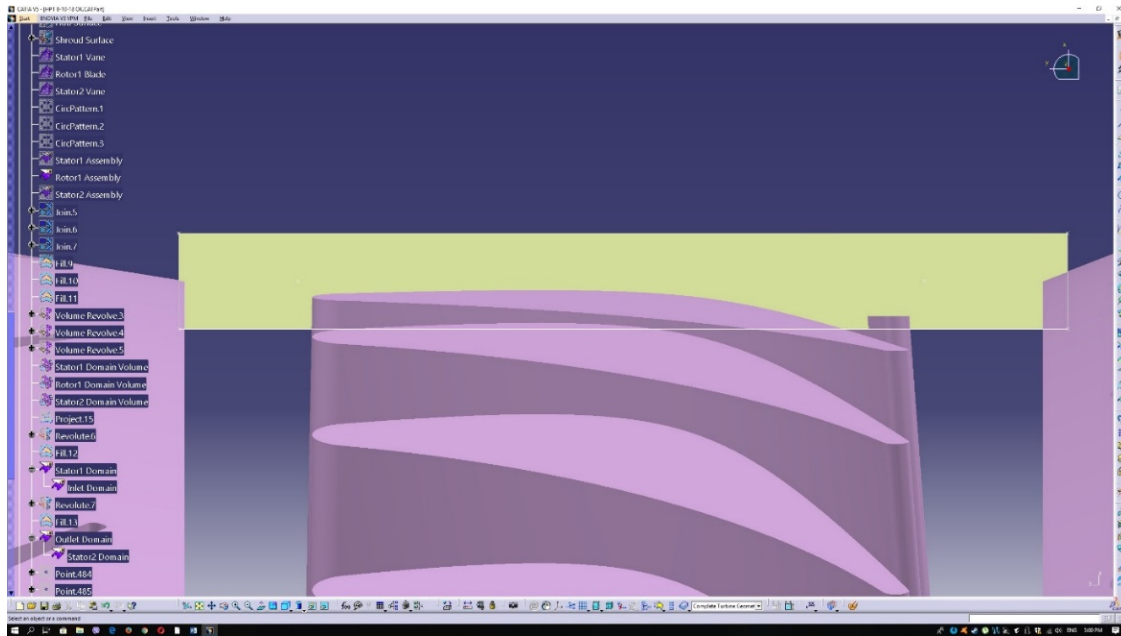


Figure 3.3.16: Profile for the supporting volume for the tip clearance region mesh control.

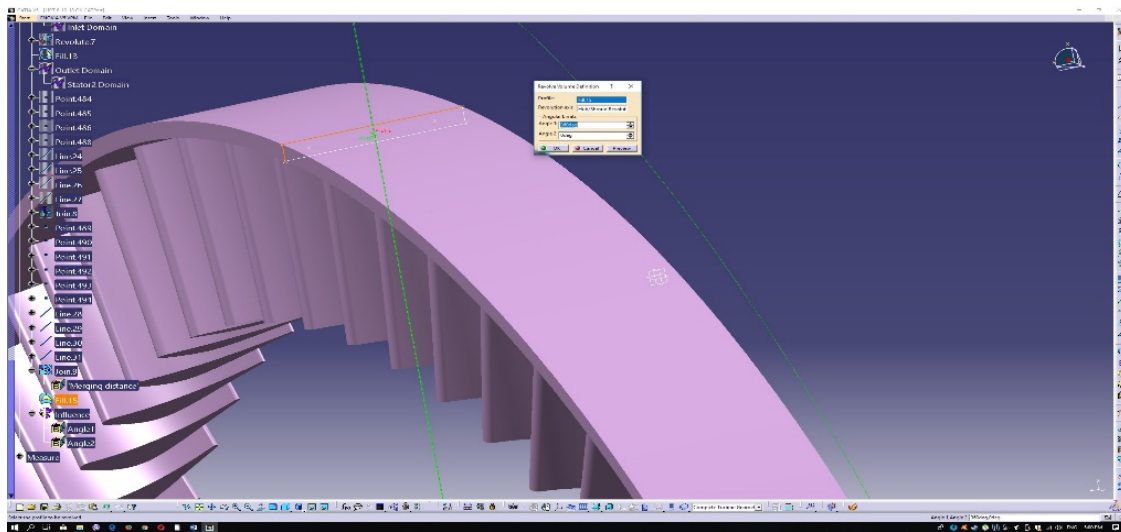


Figure 3.3.17: The supporting volume for the tip clearance region mesh control.

Finally, only the objects that are going to be studied in ANSYS CFX are to remain, while the others are to be hidden, as to avoid any unwanted elements making their way into the CFD analysis. The objects that should not be hidden, are the following: inlet volume, 1<sup>st</sup> stator volume after the Boolean operation, rotor volume after the Boolean operation, 2<sup>nd</sup> stator after the Boolean operation, outlet volume, tip clearance volume. The final result should be as in Figure 3.3.18.

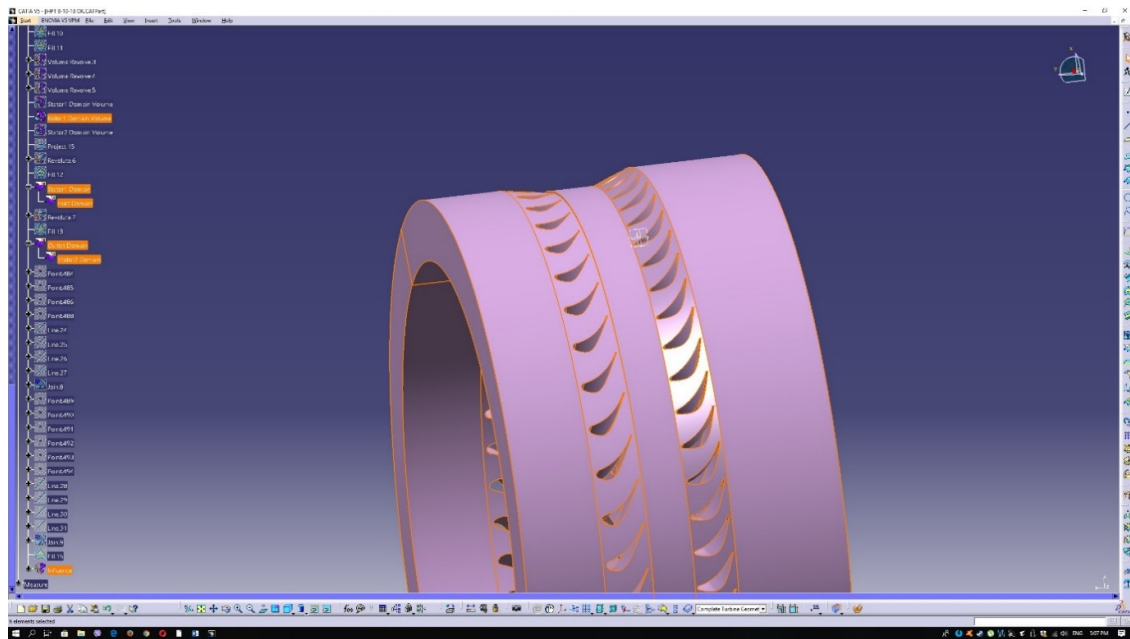


Figure 3.3.18: Final result of the turbine design. The highlighted objects should remain visible.

## Chapter 4: ANSYS 17.0 Geometry and Meshing Modules

### 4.1 Geometry Import and Handling

In order to make it easier for ANSYS 17.0 to recognize the input model the CATIA V5R20 output file should have a “step” format. So the final project, which was completed in the previous section, should be stored as an “.stp” file.

After opening the ANSYS 17.0, the CFX analysis system should be dragged onto the main section of the window. The CFX module consists of several different modules, namely: “Geometry”, “Mesh”, “Setup”, “Solution”, and “Results”.

Clicking on the first module the user is transferred to the “Geometry” interface. Using this interface the step geometry file can be imported, using the “Import” command. After the file is imported, the “Generate” button should be used in order to display the model. It can be seen that the model is comprised of six parts, namely the parts that were left visible before the generation of the step file in CATIA V5R20.

Since the parts are arbitrarily named, the first task is to name them intuitively, an important step for the meshing and setup to follow. The six major parts are named accordingly. For each part the inlet, outlet, hub, shroud, pressure/suction sides and trailing/leading edges should be defined.

To achieve that, the surfaces to be named should be right-clicked and then the “Named Selection” command should be used. When it comes to several parts under the same name, a multiple selection can be performed, either by clicking while having the Ctrl button pressed or by using the “Box Select” feature at the top left of the interface. The new surface clusters can either be named directly after the “Named Selection” command is utilized, or later by right clicking on them on the tree outline and using the “Rename” feature.

The following figures demonstrate the steps that should be taken in order to prepare the imported geometry for further analysis. It should be noted that Figure 4.1.3 depicts the recommended list of named selections that are to be created. As a final remark, it should be stated that creating named selections is not pivotal to the analysis that follows, as named selections can be implemented further on (meshing module), but still readily available and intuitive named selections make the whole process a lot easier.

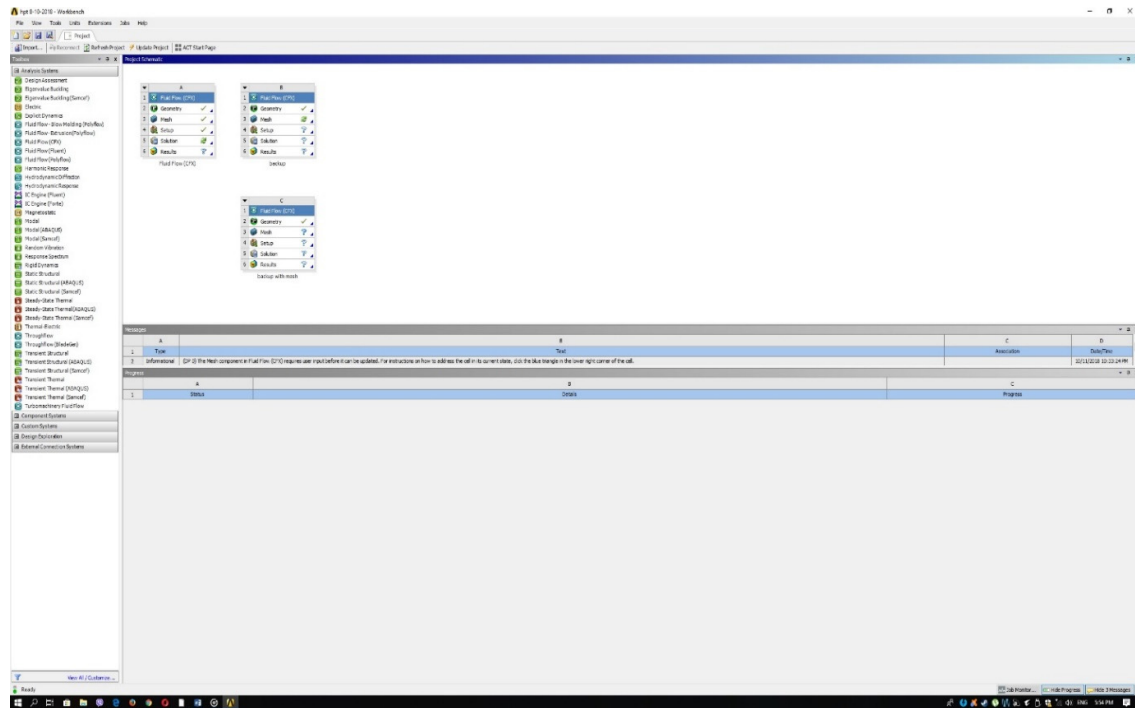


Figure 4.1.1: ANSYS initial interface.

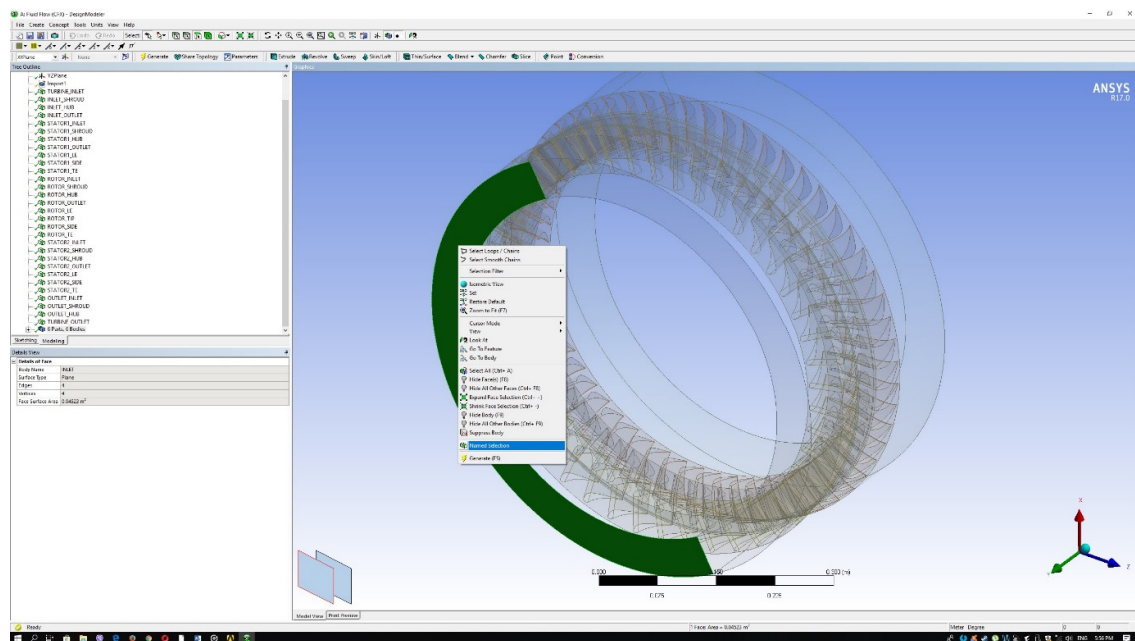


Figure 4.1.2: Named selection command.

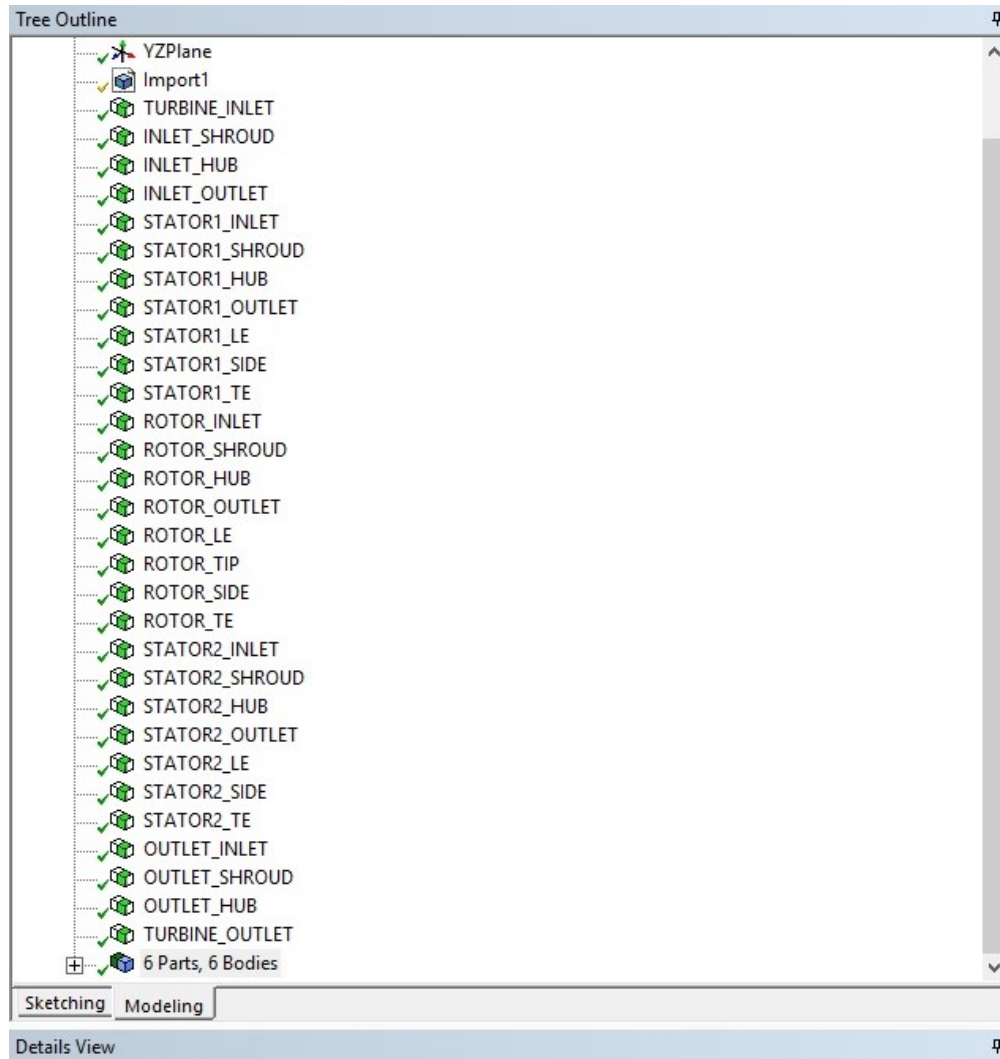


Figure 4.1.3: List of named selections.

The final step to be taken whilst in the Geometry module, is to set all six domains as fluid domains. This can be achieved by clicking on each of the six parts and in the “Details View”, section selecting “Fluid” on the “Fluid/Solid” selection segment. The figure below demonstrates the above step.

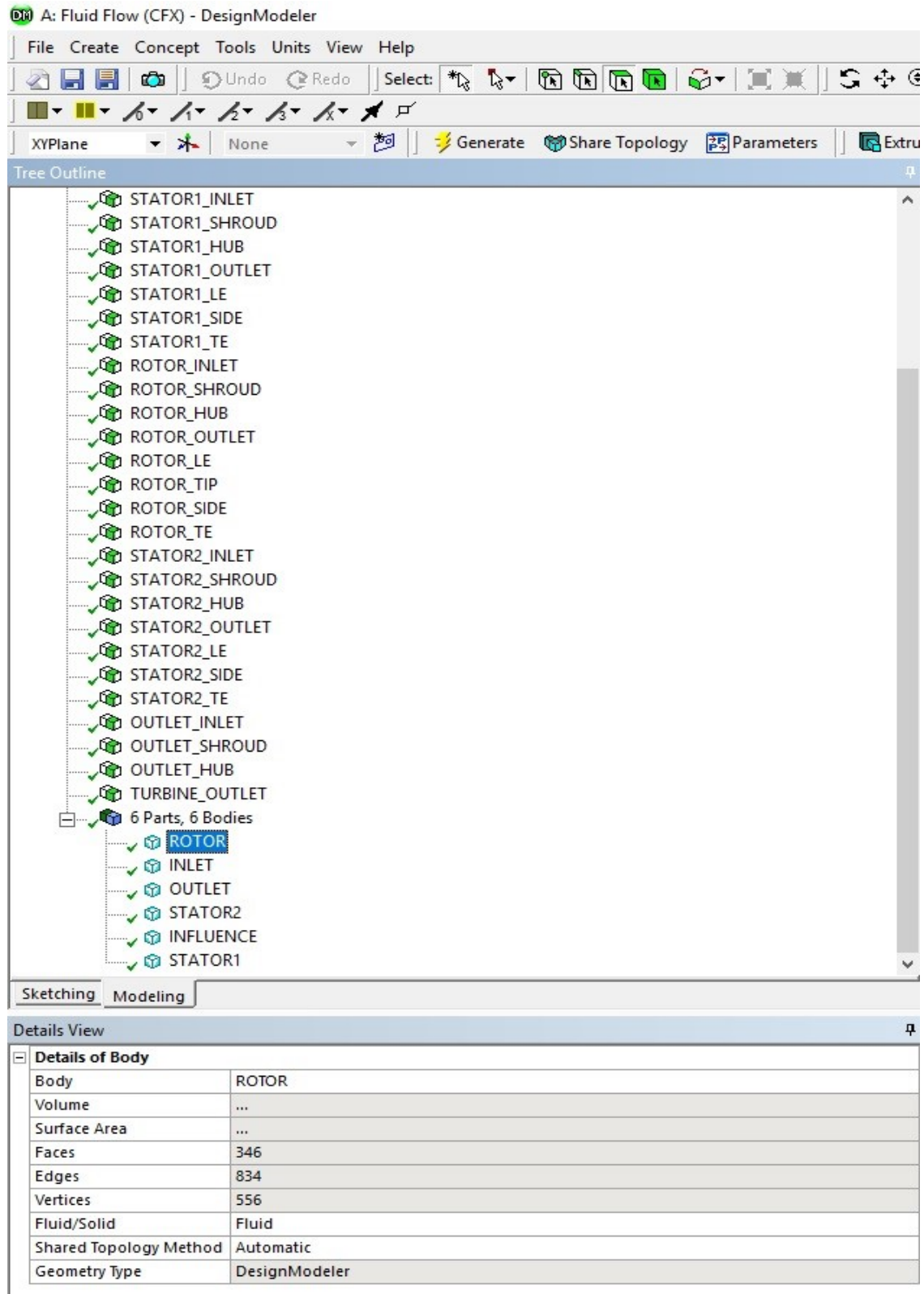


Figure 4.1.4: Fluid selection for the six domains.

## 4.2 Model Meshing

Now the model is ready to be meshed. In order to do that, the meshing module should be utilized. The meshing module is the one right below the geometry module. Once the model is ready to be meshed a green check-mark will appear next to the geometry module, meaning that the user is ready to move onto the next module.

Entering the mesh interface the user is greeted by the mesh tree outline on the top left and the mesh global settings on the bottom left. The global settings will be mostly left as is, since separate sizing and inflation rules will be given for each part and surface.

The stators' domains and the rotor's domain will be meshed using tetrahedrons (patch conforming method) while all of their solid surfaces, onto which boundary layers are going to form, will be meshed using inflation layers. The inlet and outlet domains will be meshed using hex mesh (multizone) since their geometry is relatively simple (swappable) and allows for such action. Same as above, an inflation layer will be implemented for all the solid surfaces.

The mesh for the rotor and stators will be very fine, as the flow in their respective passages is extremely complex. The mesh size for the outlet and inlet will be slightly less fine, with larger elements comprising it.

To size or to add inflation to the mesh one must simply right click on the "Mesh" option in the tree outline and then select "Insert" → "Sizing"/"Inflation", as shown in Figure 4.2.1.

To size the domains, after selecting the sizing feature, in the way described above, the "Element size" should be selected and then right below the desired size should be imported. The "Element size" method will be used for the stator domains. For the rotor domain, since the tip clearance area should be characterized by an even finer mesh, the sizing method used should be the "Body of influence". At the final stages of the model design, an extra "influence" volume was added. This volume will act as the body of influence, enacting upon the tip clearance area a very fine mesh, while leaving the rest of the rotor body intact. The mesh affected by the influence volume is going to be the one that belongs to the common volume of the rotor and influence domains. The surfaces belonging to said domains are to be sized as well. The same method applies here. The figures below graphically depict the sizing process.



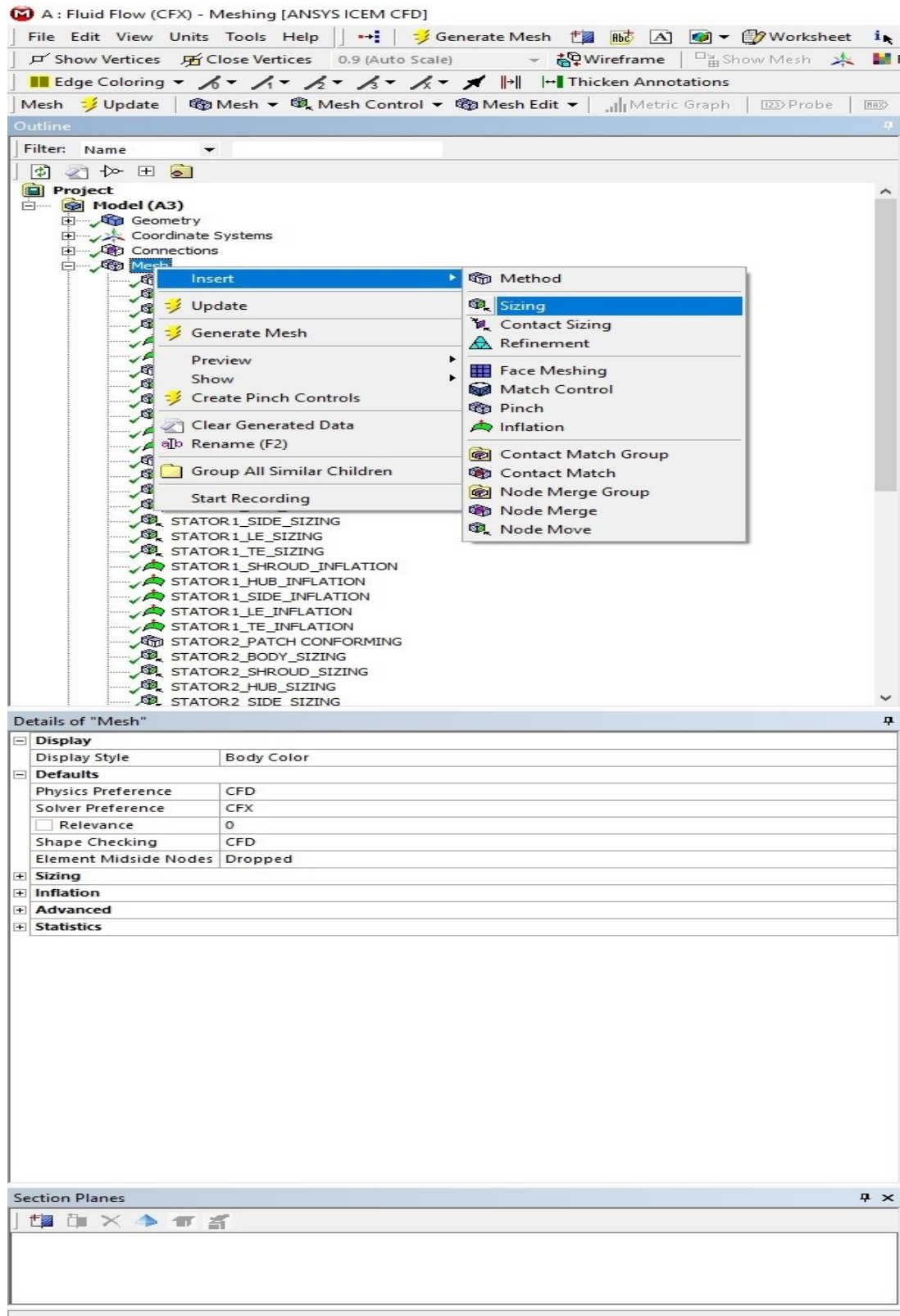


Figure 4.2.1: Sizing feature.



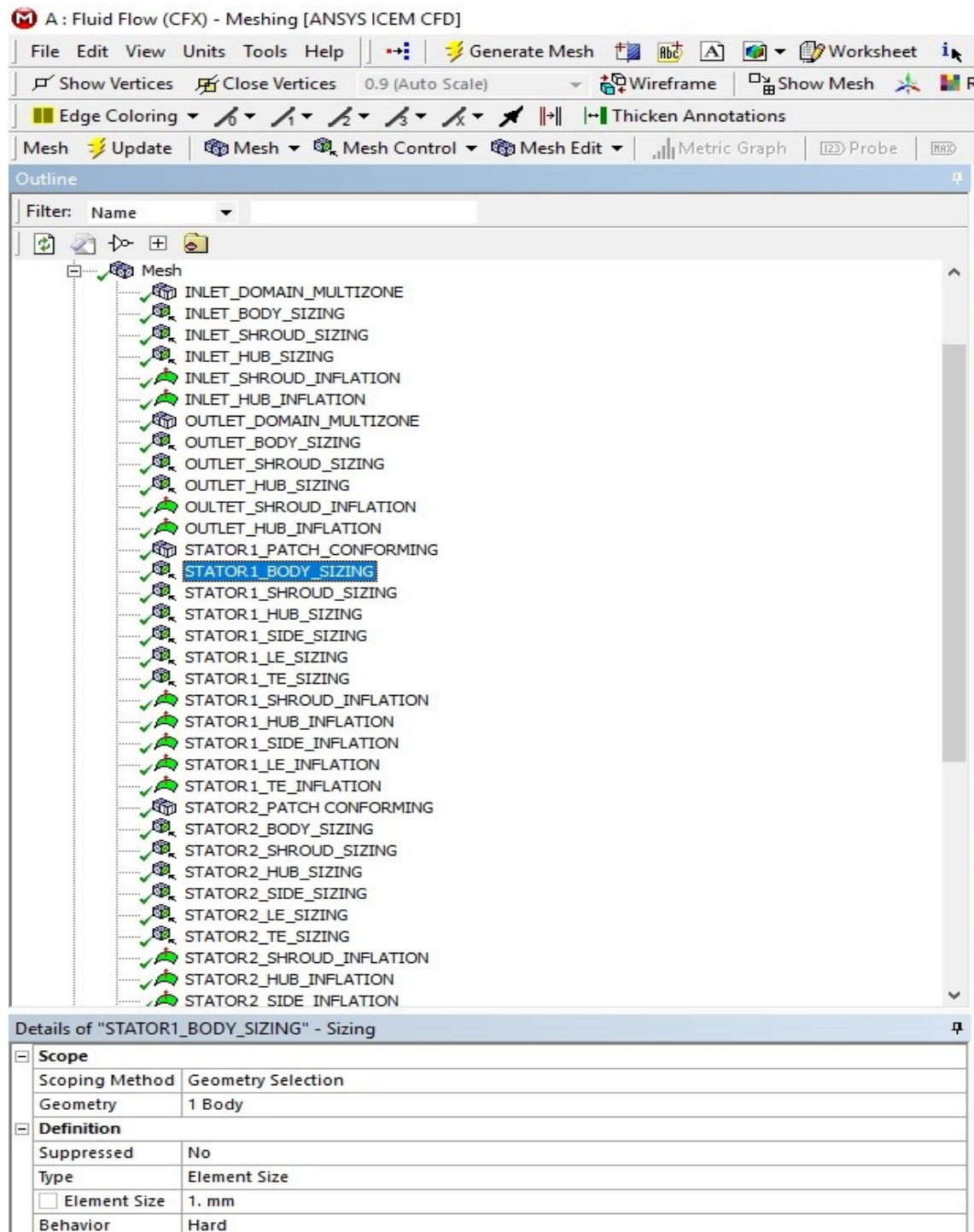


Figure 4.2.2: Body sizing using the Element Size method.

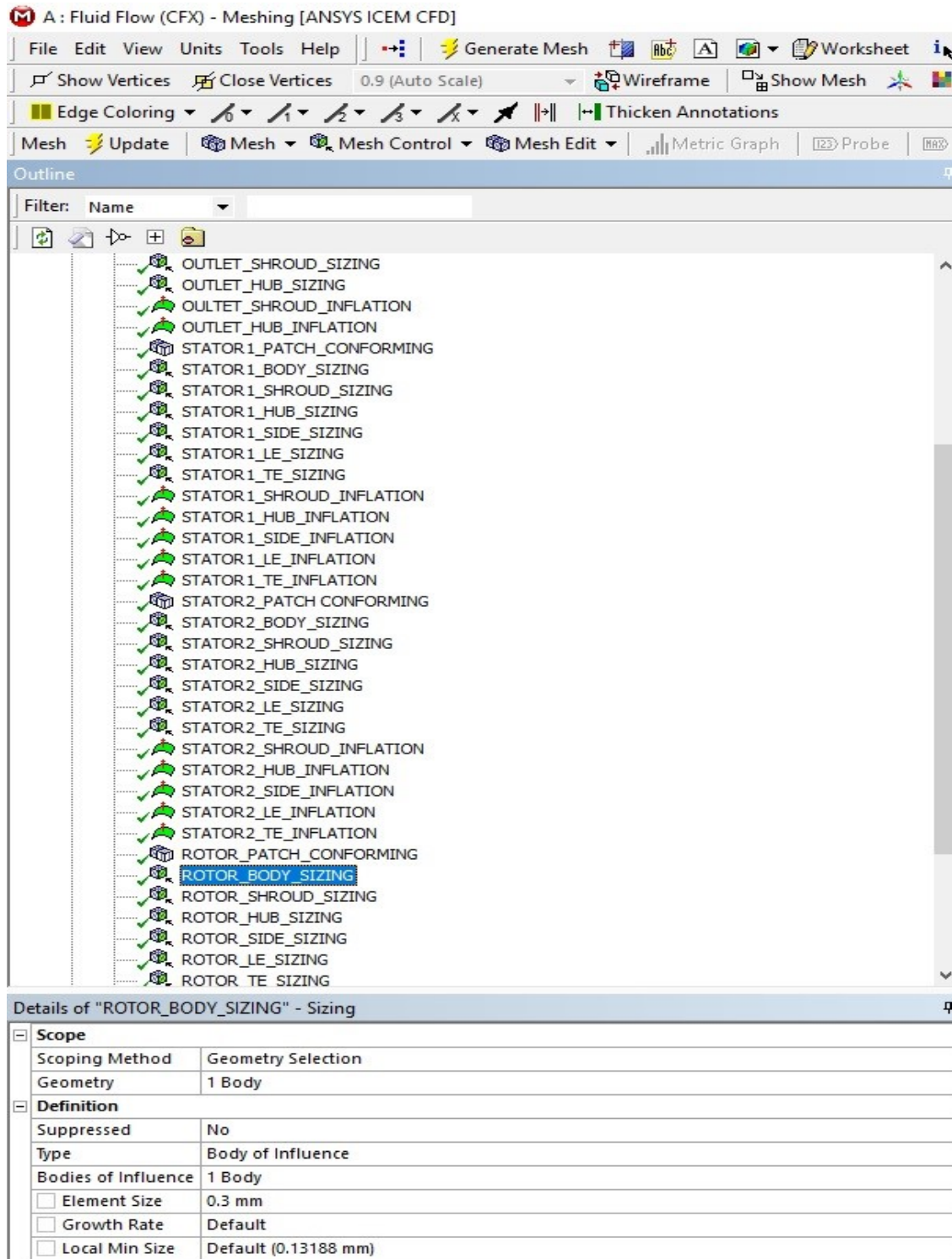


Figure 4.2.3: Body sizing (rotor) using the body of Influence method.

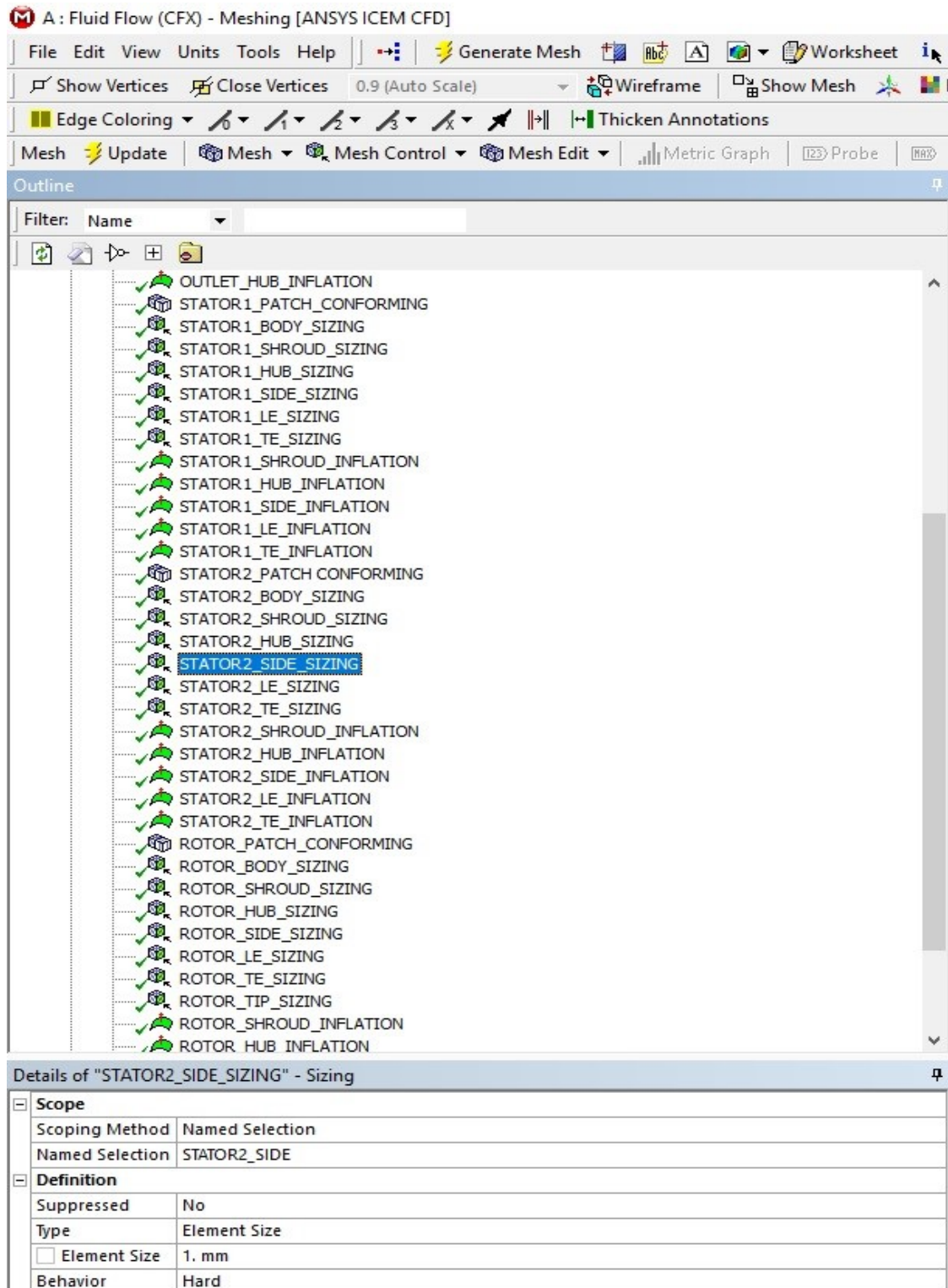


Figure 4.2.4: surface sizing using the Element Size method.

As far as the global settings are concerned, the “Max face size” and “Max tet size” will be set to 1 mm and 1.5 mm respectively, so that the unaffected rotor body (i.e. the rotor volume that was left unaffected from the body of influence) can be limited to the desired size. The following Figure 4.2.5 demonstrates the procedure.

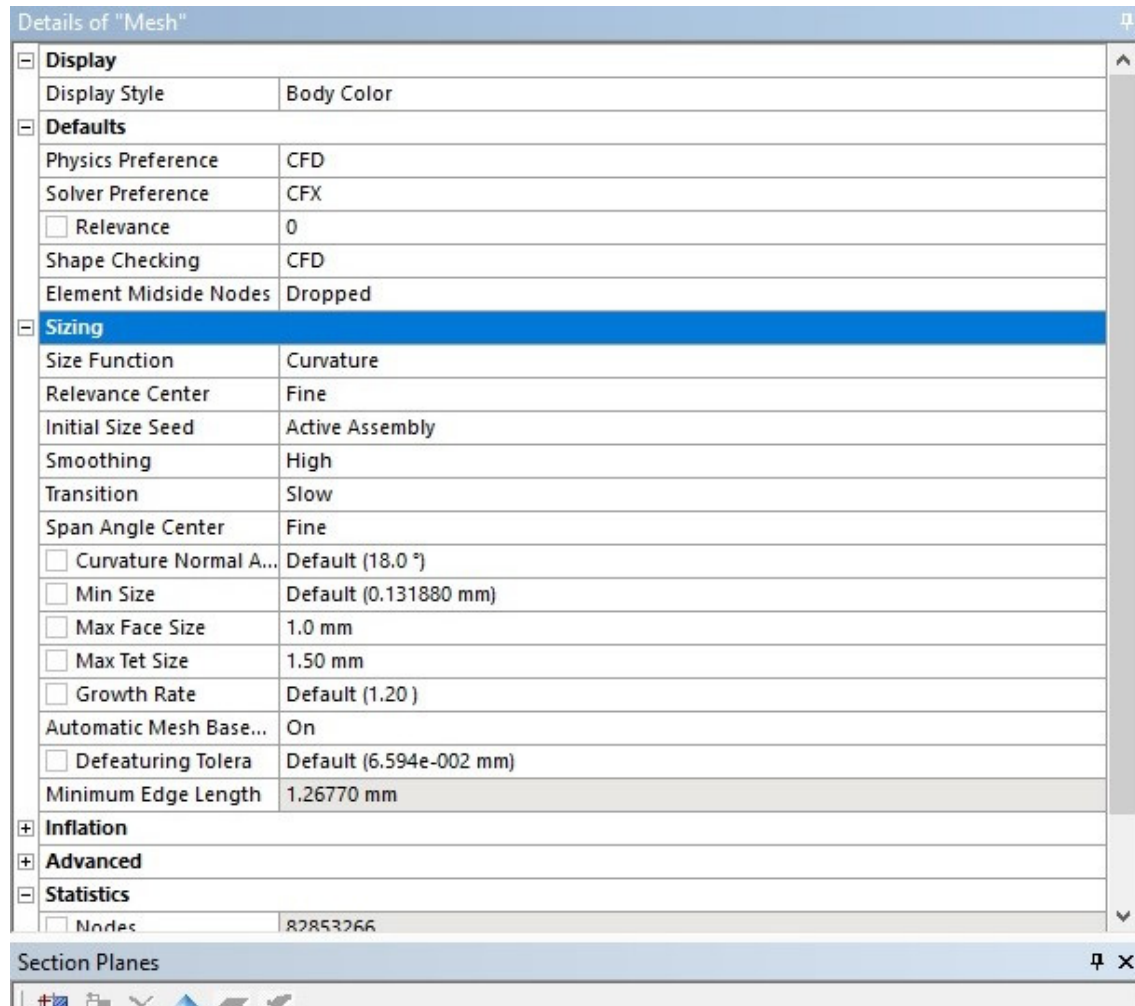


Figure 4.2.5: Global setup.

After the sizing of the bodies/surfaces, inflation layers are to be added to every solid surface of the model. The inflation method that will be uniformly used is the “First Layer Thickness”, where the thickness of the first layer is controlled by the user.

At this point, a concept needs to be discussed. The  $y_+$  value is a dimensionless wall distance for a wall bounded flow and can be defined as follows

$$y_+ = \frac{\rho \Delta y_1 u_t}{\mu} \quad (4.2.1)$$

$$v_\tau = \sqrt{\frac{\tau_w}{\rho}} \quad (4.2.2)$$

$$\tau_w = 0.5C_f \rho u^2 \quad (4.2.3)$$

$$C_f = \frac{0.058}{Re^{0.2}} \quad (4.2.4)$$

where  $\Delta y_1, u_\tau$  are the distance from the wall and the friction speed respectively [ANSYS CFX-Solver Theory Guide].

The  $y_+$  value is used to evaluate the near wall mesh. A small  $y_+$  value means that the mesh is close enough to the wall surface to evaluate the viscous sublayer of the boundary layer. The  $y_+$  value can only be calculated after the solver is finished, since only then an accurate depiction of the velocity flow field is available. Nevertheless, a thin first inflation layer insures favorable  $y_+$  values and adequate boundary layer representation. For this reason, the first layer thickness of the inflation mesh is chosen to be 0.001 mm for all the surfaces, except for the rotor tip and shroud, where the first inflation layer has set for 0.0005 mm thickness.

In order to induce an inflation mesh over a given surface, the user needs to right click on the “Mesh” feature of the tree outline, and insert an inflation mesh. After that, the domain into witch the inflation will be created should be chosen, as well as the “Boundary”, which, in essence, is the surface to be enclosed in the inflation mesh. The figure below depicts the setup for an inflation layer.



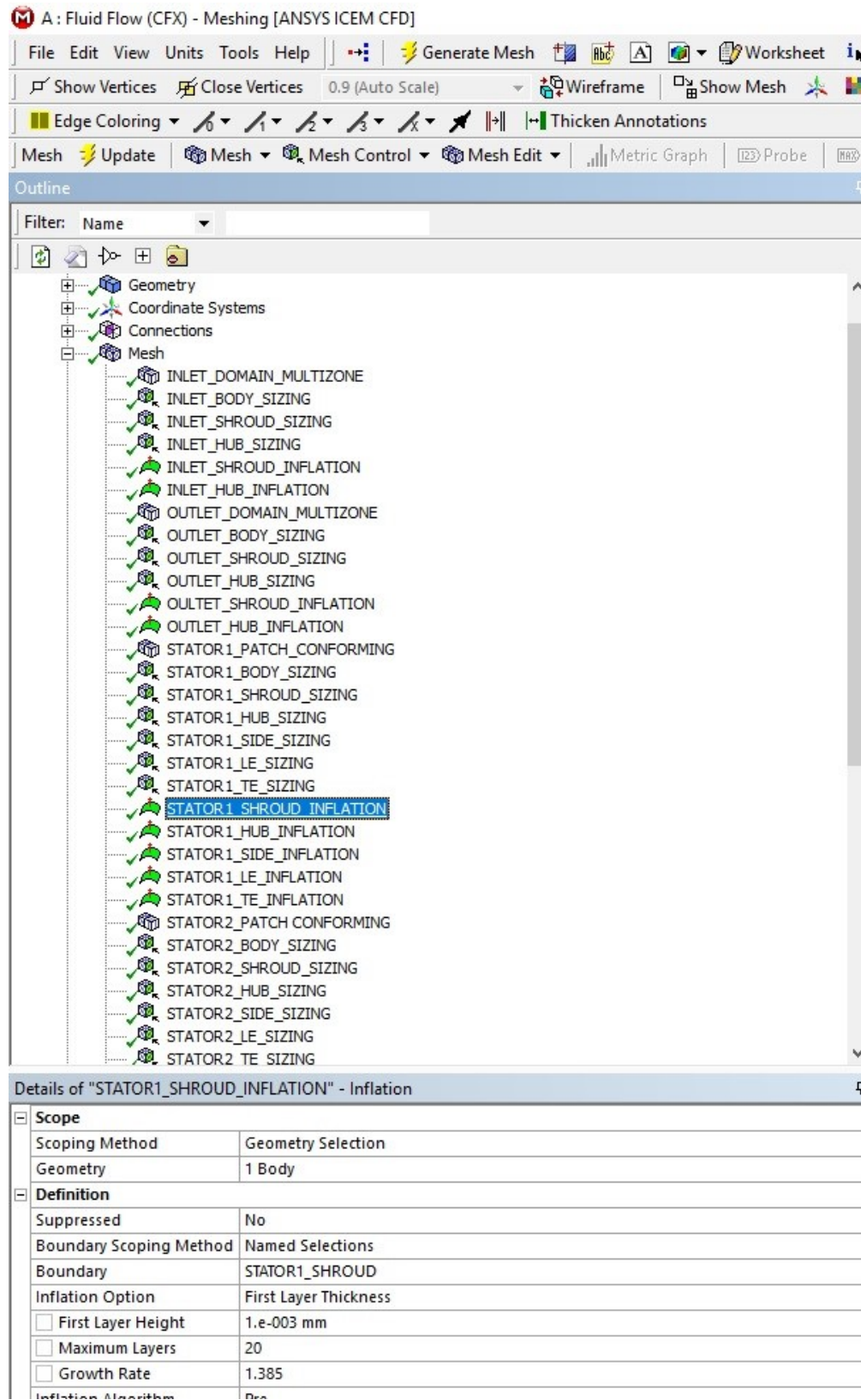


Figure 4.2.6: Inflation setup.

The tables that follow contain all the information for the sizing and inflation, needed to complete the model's mesh.

Part	Method	Size	Behavior
Stator1/2 Body/Hub/Shroud/Side	Element Size	3mm	Hard(Stator2)/Soft(Stator1)
Stator1/2 Side	Element Size	2mm	Hard(Stator2)/Soft(Stator1)
Stator1/2 Leading Edge	Element Size	1mm	Hard(Stator2)/Soft(Stator1)
Stator1/2 Trailing Edge	Element Size	0.5mm	Hard(Stator2)/Soft(Stator1)
Rotor Body	Body of Influence	0.35mm	-
Rotor Shroud	Element Size	3mm	Soft
Rotor Hub	Element Size	3mm	Soft
Rotor Side	Element Size	2mm	Soft
Rotor Leading Edge	Element Size	1mm	Soft
Rotor Trailing Edge	Element Size	0.5mm	Soft
Rotor Tip	Element Size	0.75mm	Soft
Inlet/Outlet Body/Shroud/Hub	Element Size	4mm	Hard

Table 4.2.1: Sizing information.



Part	Method	First Layer Height	Maximum Layers	Growth Rate
Stator1/2 Shroud/Hub/Side/Leading Edge/Trailing Edge	First Layer Thickness	0.01mm	15	1.45
Rotor Shroud/Tip	First Layer Thickness	0.0005mm	15	1.53
Rotor Hub/Side/Trailing Edge/Leading Edge	First Layer Thickness	0.001mm	15	1.45
Inlet/Outlet Shroud/Hub	First Layer Thickness	0.01mm	15	1.485

Table 4.2.2: Inflation information.

The definition of the above values, combined with the two meshing methods mentioned above (patch conforming, multizone), generates the mesh presented in Figures 4.2.7 – 4.2.9.

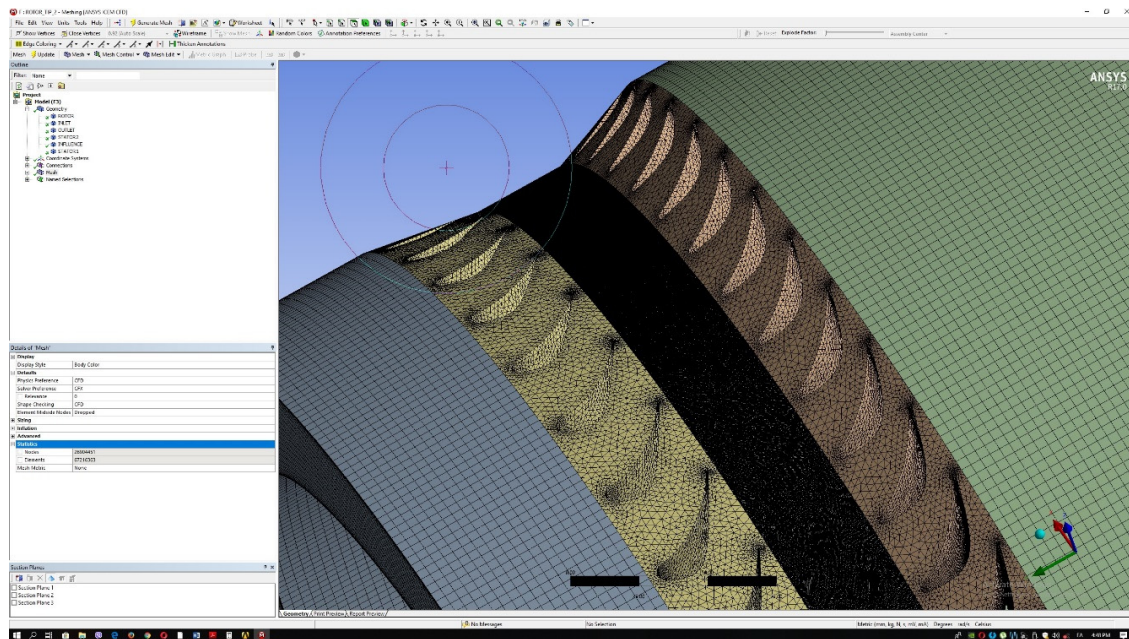


Figure 4.2.7: Mesh overview.

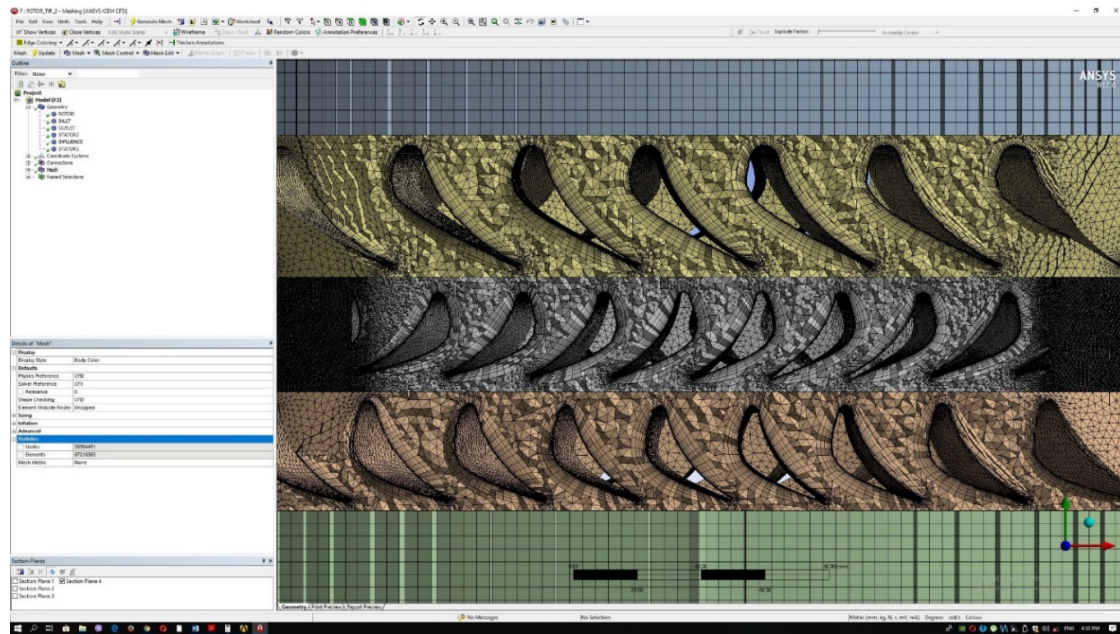


Figure 4.2.8: Inflation layers.

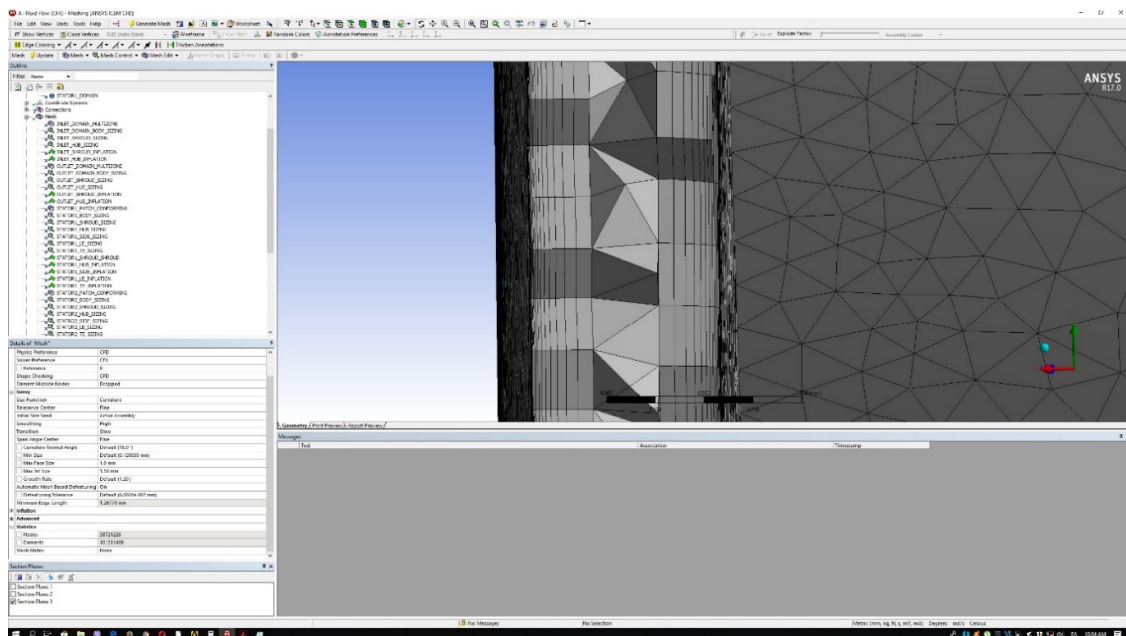


Figure 4.2.9: Rotor tip-shroud mesh (close-up).

The produced mesh consists of 26,904,451 nodes and 67,216,363 elements. Due to the magnitude of the mesh a 64GB RAM machine was used for the simulation.

## Chapter 5: Problem Setup and Boundary Condition Specification

### 5.1 Boundary Conditions Calculation

Boundary conditions are pivotal for the robustness of the simulation and the realization of valid results in CFX-Post.

The boundary conditions will be calculated using a 1D analysis of the flow-path through the engine, from inlet to turbine outlet. To achieve this the following assumptions should be made:

- The isentropic efficiencies of the individual components are estimated to be 0.85. That is the compressor and the turbine.
- The pressure loss coefficient of the combustion chamber is set to 0.05.
- The overall compression ratio of the fan/compressor is set to be 32:1, whilst each individual ratio is set to be 4 and 8 respectively.
- Formulas that follow were all taken from [El Sayed, 2017].

The following Figure 5.1.1 depicts the engine's cross section and the station numbering convention, used for each of the components exit and inlet.

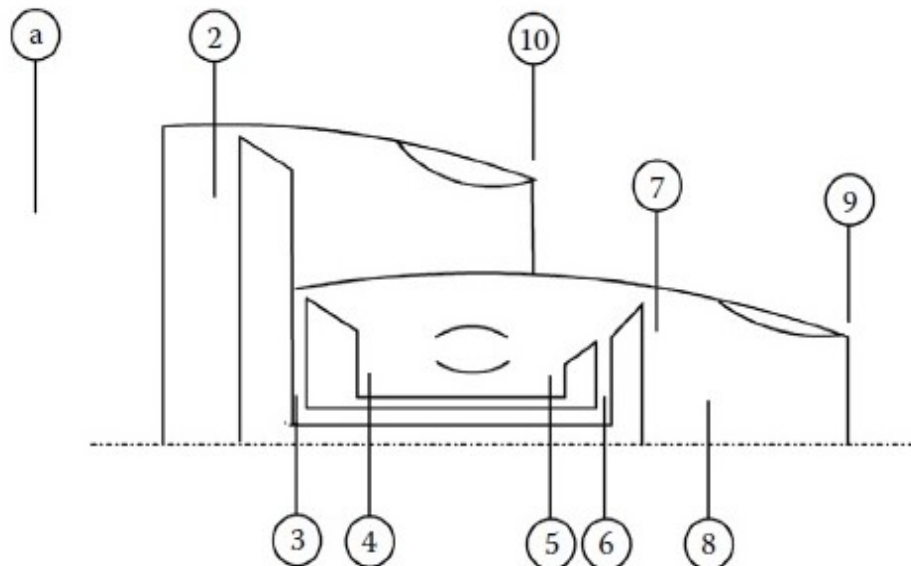


Figure 5.1.1 Numbered Engine Stations [El Sayed, 2017].

Ambient pressure and temperature are considered to be 101,325 Pa and 288 K respectively. Furthermore, the engines inlet is considered to be adiabatic, and no losses take place as flow travels from the aircraft's inlet to the fan inlet case.

Considering the above convention we have

$$P_a = P_{02} = 101,325 \text{ Pa}, \quad (5.1.1)$$

$$T_a = T_{02} = 288 \text{ K}. \quad (5.1.2)$$

Making use of the known fan's compression ratio, the pressure at the inlet of the high pressure compressor can be calculated as

$$P_{03} = \pi_f P_{02} = 405300 \text{ Pa}. \quad (5.1.3)$$

The corresponding temperature at the inlet of the high pressure compressor can be calculated as

$$T_{03} = T_{02} \left[ 1 + \frac{1}{n_f} \left( \pi_f^{\frac{\gamma-1}{\gamma}} - 1 \right) \right] = 452 \text{ K}. \quad (5.1.4)$$

Similarly with the fan, the compressor's exit pressure can be calculated by utilizing its known pressure ratio

$$P_{04} = \pi_{hpc} P_{03} = 3,242,400 \text{ Pa}. \quad (5.1.5)$$

The temperature at the compressor's exit will be the following

$$T_{04} = T_{03} \left[ 1 + \frac{1}{n_{hpc}} \left( \pi_{hpc}^{\frac{\gamma-1}{\gamma}} - 1 \right) \right] = 882 \text{ K}. \quad (5.1.6)$$

The pressure drop at the combustor can now be used and then

$$P_{05} = (1 - \Delta P_{cc} \%) P_{04} = 3,080,280 \text{ Pa}. \quad (5.1.7)$$

The turbine inlet temperature (TIT) is generally known beforehand. In this case the TIT was chosen to be 1623 K.

The pressure at the outlet of the high pressure turbine should now be defined. In order to achieve that, a power equilibrium should be set up on the combustor and the high pressure shaft.

$$\dot{m}_a C_{pc} T_{04} + \eta_{CC} \dot{m}_f Q_{LHV} = (\dot{m}_a + \dot{m}_f) C_{pg} T_{05}. \quad (5.1.8)$$

For the above, the fuel's LHV was set to 42,620 kJ/kg, as this is the JP-8 grade fuel heating value. The above now yields the following

$$\dot{m}_f = 2.4 \frac{kg}{sec}.$$

Now, the shaft power equilibrium is to be set up. It should be noted that the mechanical losses regarding the shaft are considered to be 5%.

$$\dot{W}_{HPT} = \frac{\dot{W}_{HPC}}{n_{shaft}}, \quad (5.1.9)$$

$$\dot{m}_a C_{pc}(T_{04} - T_{03}) = n_{shaft} \dot{m}_r C_{ph}(T_{05} - T_{06}). \quad (5.1.10)$$

When solved for  $T_{06}$  Eq. (5.1.10) yields

$$T_{06} = 1237 \text{ K}.$$

Now, it is possible to calculate the pressure at the exit of the turbine as

$$P_{06} = P_{05} \left[ 1 - \frac{1 - \frac{T_{06}}{T_{05}}}{n_{hpt}} \right]^{\frac{\gamma_g}{\gamma_g - 1}} \Rightarrow \quad (5.1.11)$$

$$P_{06} = 820,583 \text{ Pa}.$$

It is assumed that the 1<sup>st</sup> stage is responsible for approximately 65% of the total pressure drop within the turbine, therefore

$$\Delta P_{tot} = P_{05} - P_{06} = 2,259,696 \text{ Pa}.$$

This means that the pressure drop in the 1<sup>st</sup> stage is the following:

$$\Delta P_{stg1} = 0.65 \Delta P_{tot} = 1,468,803 \text{ Pa}$$

Thus, the pressure at the exit of the first stage is

$$P_{0stg1} = P_{05} - \Delta P_{stg1} = 1,611,476 \text{ Pa}.$$

The total pressure at the inlet of the 2<sup>nd</sup> stage stator is taken the same as the one at the exit of the 2<sup>nd</sup> stage stator (this is of course an approximation, since we have friction losses – especially inside the boundary layers – which decrease total pressure).

The total pressure at the inlet of the stator is approximately equal to the total pressure calculated at the exit of the 1<sup>st</sup> stage rotor, thus:

$$P_{0stg1} = P_{0str2exit} = 1,611,476 \text{ Pa}.$$

Assuming that the Mach number at the 2<sup>nd</sup> stg stator exit is approximately 0.85 (modern HPTs are transonic), then the static pressure at the 2<sup>nd</sup> stage stator exit, according to the isentropic compressible fluid tables should be:

$$P_{str2exit} = 0.62 P_{0str2exit} = 998,811 \text{ Pa}.$$



## 5.2 Simulation Setup in ASYS 17.0

Having calculated all the required values for the boundary conditions, the simulation setup needs to be initiated. After opening the “Setup” module of CFX system, the user has to define the rotating and the fixed walls and domains, as well as the interfaces between those domains.

The first step is to define the simulation as a steady state simulation. This can be achieved by clicking on the “Analysis Type” → “Options” → “Steady State”. In order to insert a new domain, one must select “Insert “→”Domain”, and after naming it appropriately, then to select the proper laws that define it. The figures below show a domain that was set-up for this particular simulation. It should be noted that if the governing rules of a domain are set, then every domain generated afterwards will be characterized by the same rule-set automatically.

The Inlet, Outlet, Stator1, Stator2 domains are set as stationary domains, whilst the Rotor domain is set as a rotating domain. The rotor turns at 13,000 *rpm* which needs to be defined in the domain setup section of the setup. For all domains, the SST turbulence model was selected and a moderate value of 5% turbulence was selected.

The interfaces between the stationary domains are set as “General Connection”, while the interfaces between the rotating and the stationary domains are set as “Frozen Rotor”.

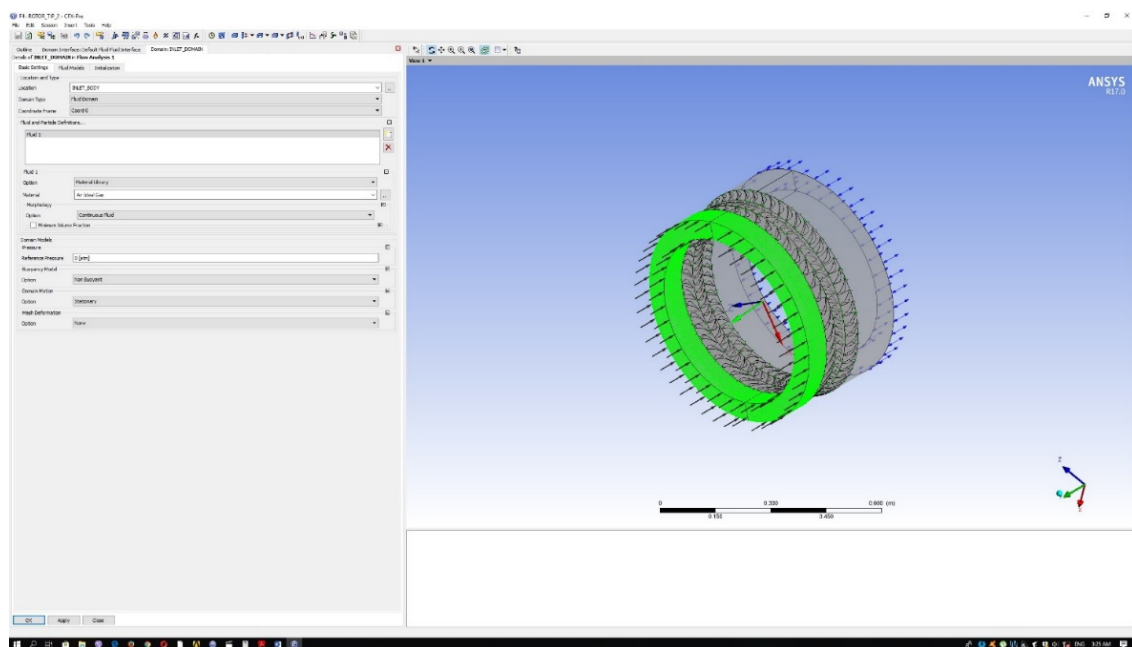


Figure 5.2.1: Domain basic setup.

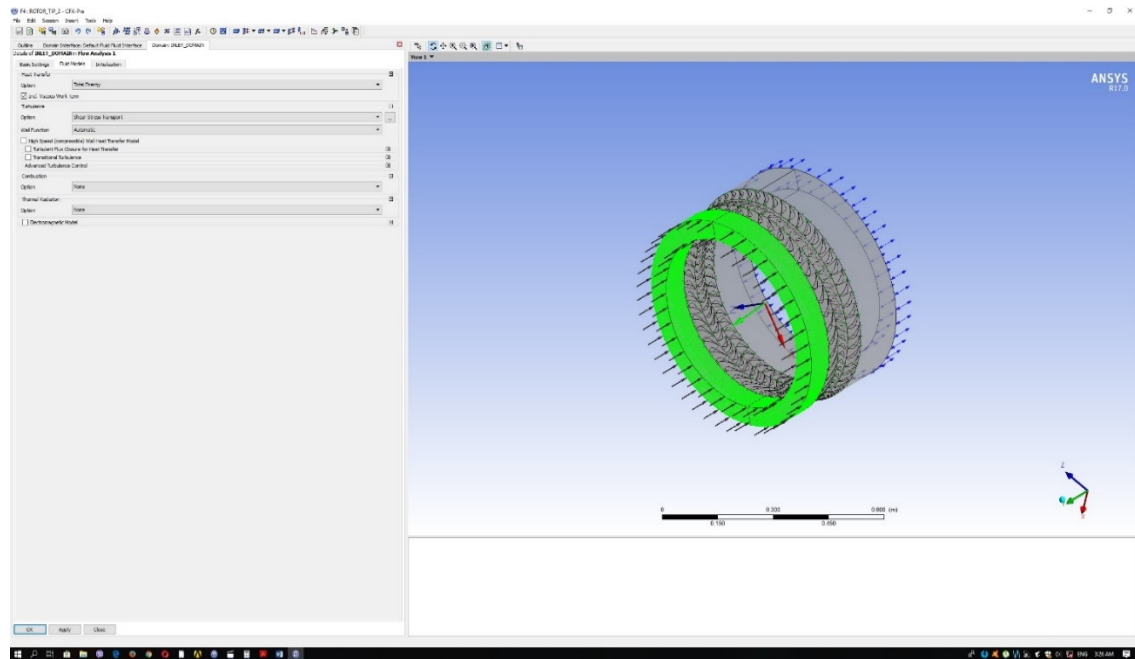


Figure 5.2.2: Domain fluid models.

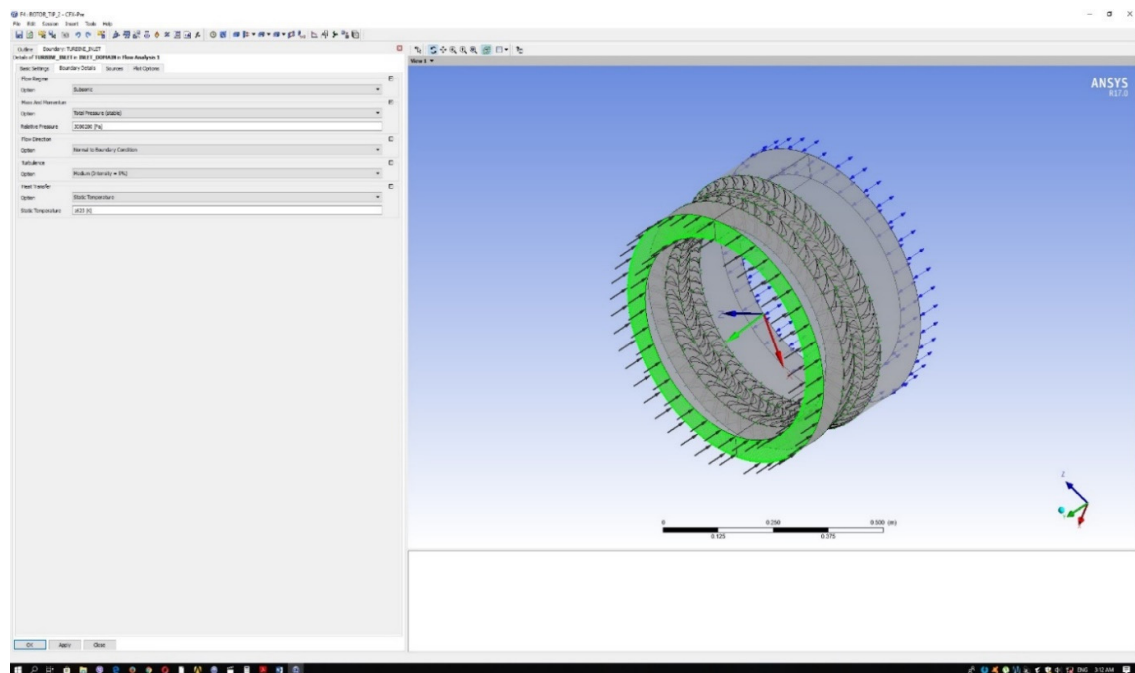


Figure 5.2.3: Inlet boundary conditions.



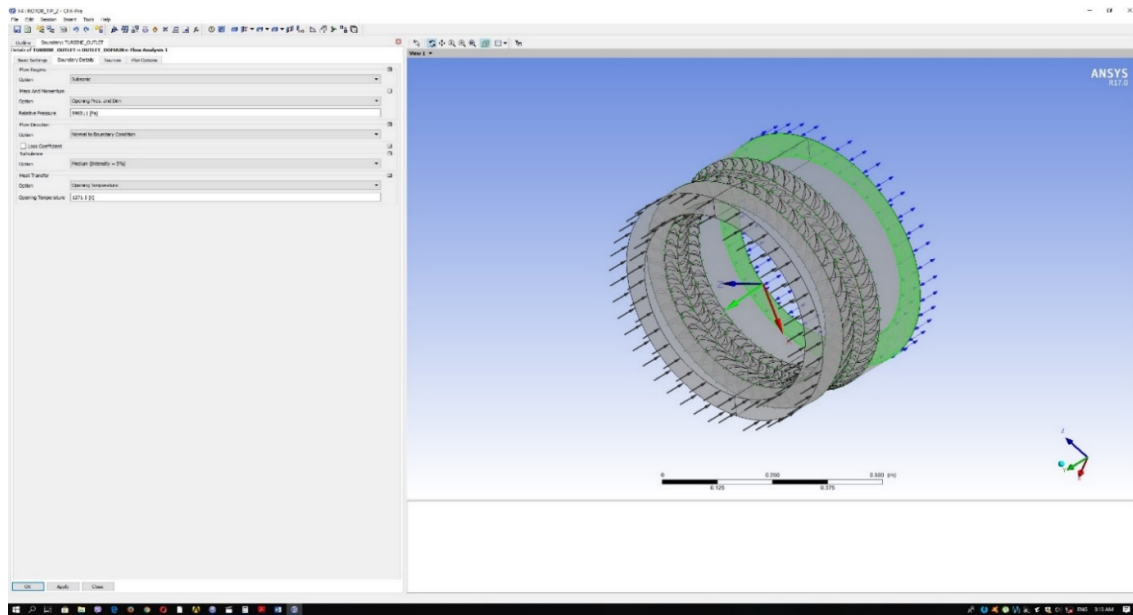


Figure 5.2.4: Outlet boundary conditions.

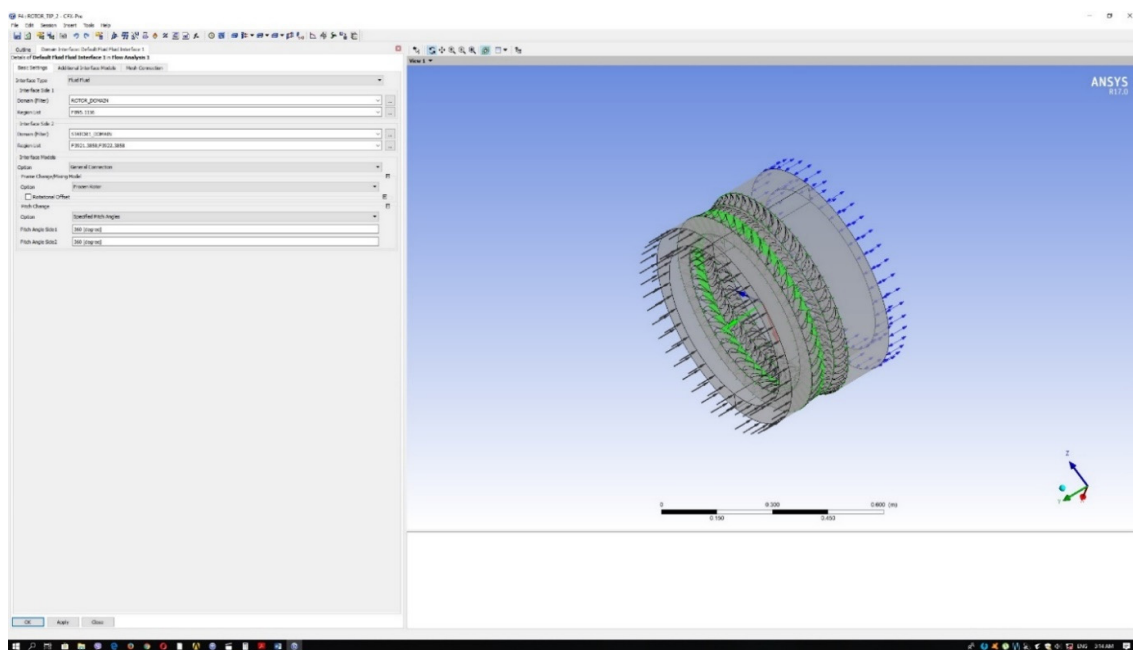


Figure 5.2.5: Frozen Rotor interface.

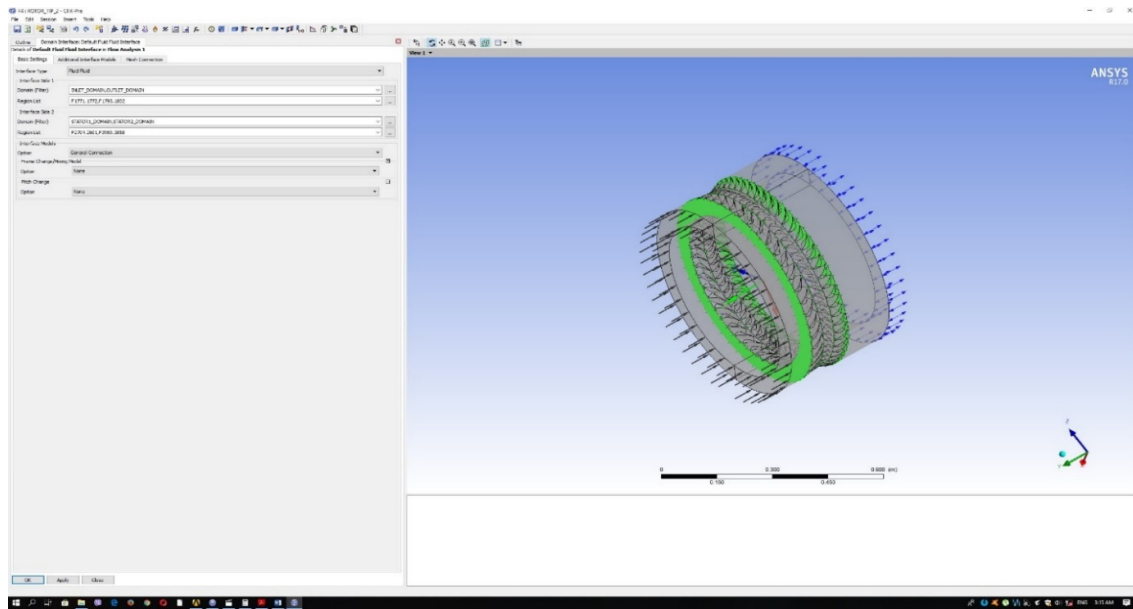


Figure 5.2.6: Stationary-to-stationary interface.

The solid walls are comprised of the shroud and hub surfaces and the blade and vane pressure, suction, leading edge, trailing edge and tip (for the rotor) surfaces. The walls that refer to the rotor domain should be set as rotating walls, with the exception of the rotor's shroud, which should remain stationary.

In order to achieve this, the Shroud wall of the rotor will be separately selected from the rest and will be set as a "Counter Rotating Wall", essentially rendering the shroud immobile. The rest of the rotor walls should be set as rotating walls with no further adjustments. The walls of the rest of the domains only need to have their bound characterized as "Wall", with no further adjustments.

Finally, the inlet and outlet of the turbine are to be defined alongside their respective boundary values. The turbine inlet is defined as an "Inlet", with a total pressure and static temperature set as boundary values. The turbine outlet is defined as an opening, with static pressure and total temperature as its boundary values.

The iteration number at the "Solver Control" was set to 300 iterations, while the convergence criteria are of "Residual Type" with a residual target value of  $1e-06$ .

## Chapter 6: Results Analysis

### 6.1 Results Extraction

Having the solution favorably converged, the “Results” module is now available to the user. To extract and evaluate results in a meaningful way, a plane was created at the mean diameter of the turbine. The plane crosses normally at least on blade and two vanes.

To achieve that, the user should select “Insert” → “Locations” → “Plane”. After that, a definition section opens up in the bottom left of the screen. The user should select a “parent” plane (XY, ZX, YZ) and then translate that plane on its respective translation axis, i.e. the Z-axis for the XY plane and so forth. The plane should be translated so that it will end up on the mean radius height.

Following the above step, the blading surfaces should be selected. In the “Outline” tab, the right surfaces should be selected from the “Mesh Region”, so that the blade/vanes are being traced normally by the generated plane. For each blade/vane the pressure surface, the suction surface and the leading edge surface should be selected.

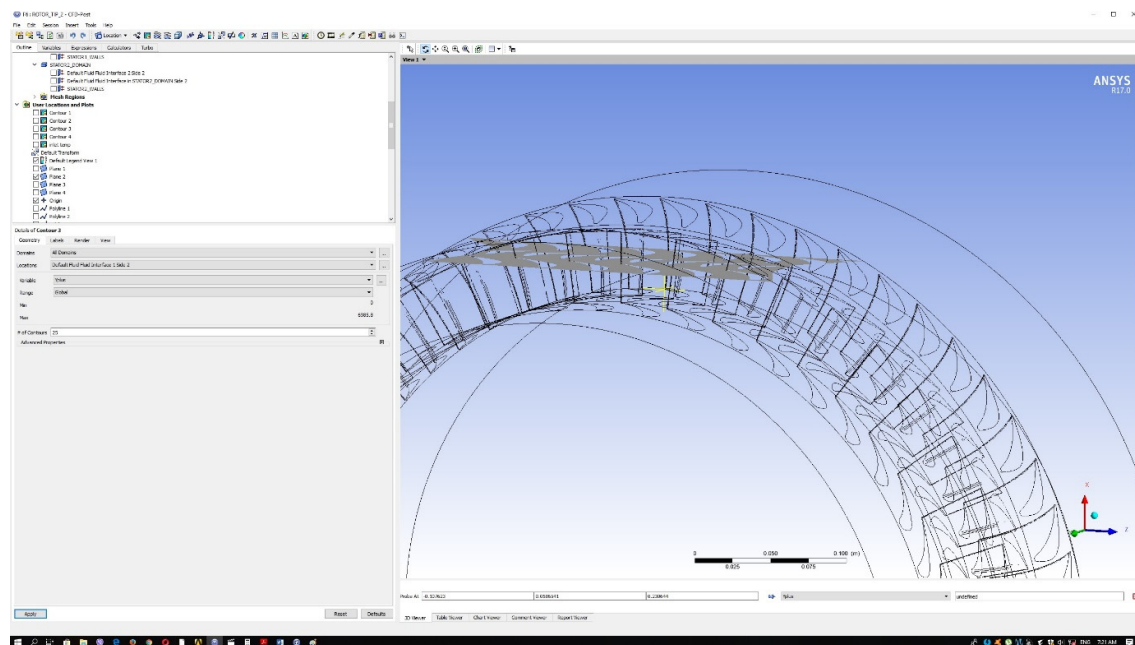


Figure 6.1.1: Plane at the turbine's mean diameter.

Using the above mid-plane, and the surfaces chosen prior from the “Mesh Regions” section, three triplets of polylines are selected, based on the traces produced from the intersection of the plane with each one of the surfaces of the blading. This will allow for a projection of the distribution of static pressure and temperature around the stator vanes and the rotor blade.

To achieve that, the “Polyline” feature should be selected from the “Locations” tab and on the definition section that will appear the “Boundary Intersection” method should be selected

from the drop down list. The generated plane and each from the selected surfaces from the “Mesh Region” list should be selected to intersect.

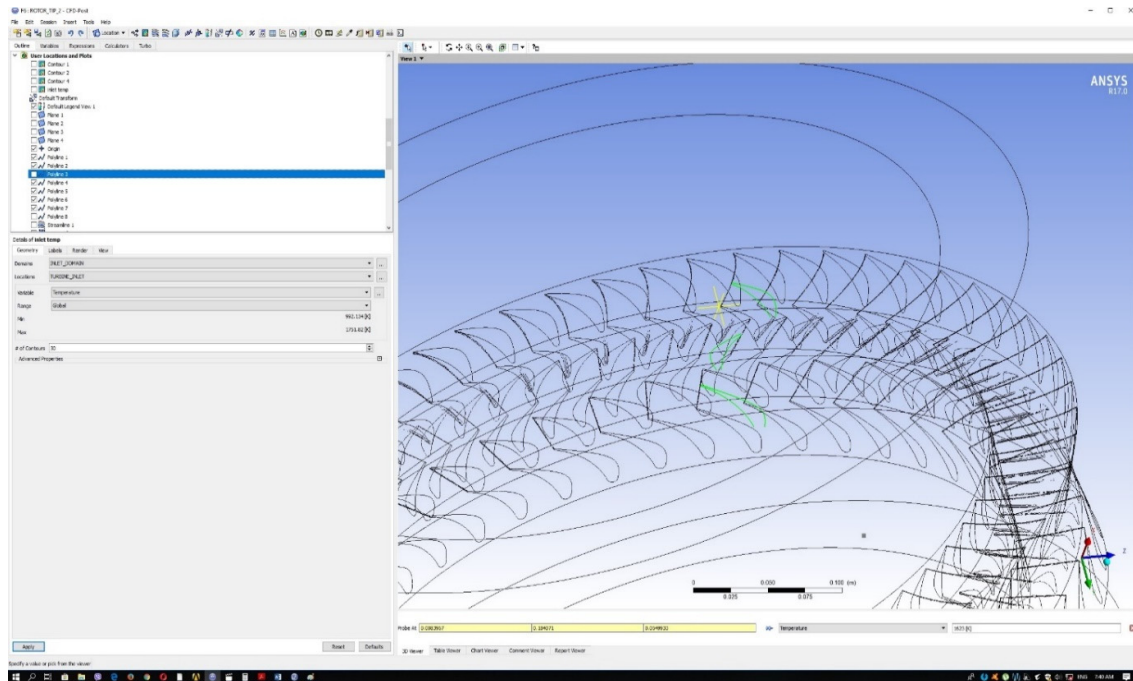


Figure 6.1.2: Blading polylines.

Additional polylines are drawn in a similar manner to provide chart information on the exit of the stators and the rotor. For this instance, a new plane should be created (as shown in Figure 6.1.3) that will eventually intersect with each one of the rotor and stator interfaces. Thus, a set of three polylines (radial in orientation) will be produced.

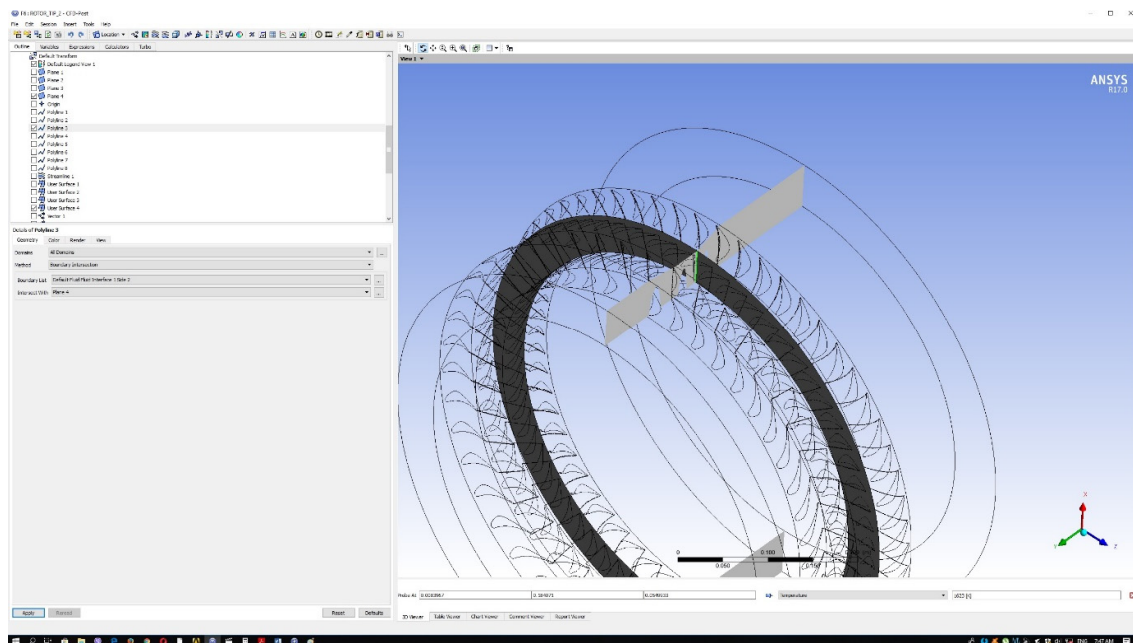


Figure 6.1.3: Radial polyline.

## 6.2 Results Evaluation

Having created the necessary geometries, the relevant charts can now be generated.

The following figures depict the static pressure distribution around the pressure and suction sides of each blade/vane.

To generate the charts, the icon “Chart” should be selected from the top of the window. In the “General” tab the user should add a title, in the “Data Series” tab the desired polylines are to be selected (alongside with their respective names), the X-axis of the chart will represent the axial direction (which is considered to be the Y direction in this simulation) and the Y-axis will represent the static pressure. It would be fair to also “trim” the chart by modifying the axis min and max boundaries. Plus, the X-axis should be inverted, since the origin point in this situation resides right between the second stage stator trailing edge and the second stage stator domain’s interface with the outlet domain

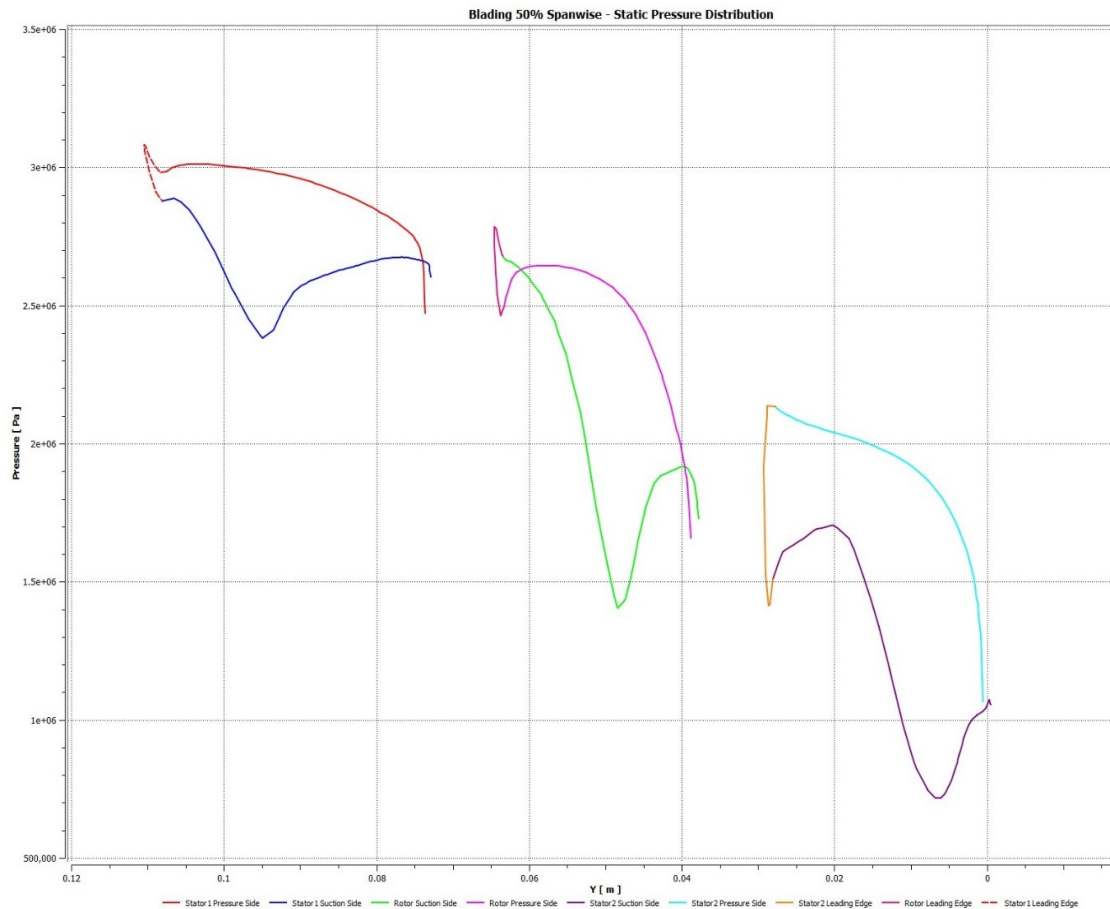


Figure 6.2.1: Blading 50% spanwise - static pressure distribution.

Since there is no experimental data on the simulated turbine, found results should be compared on a more general basis. Figure 6.2.2 below depicts a theoretical static pressure distribution around turbine bladings.

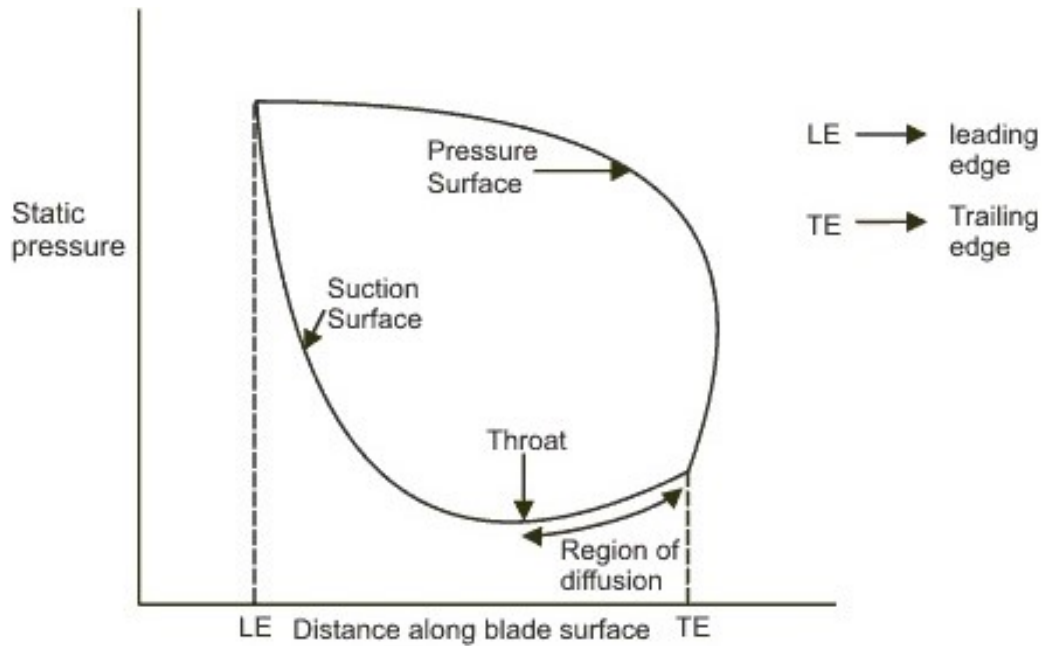


Figure 6.2.2: Theoretical pressure distribution around a turbine blade.

Following the above, a more realistic representation of what is to be expected is presented in Figure 6.2.3 [Mattingly, 1996].

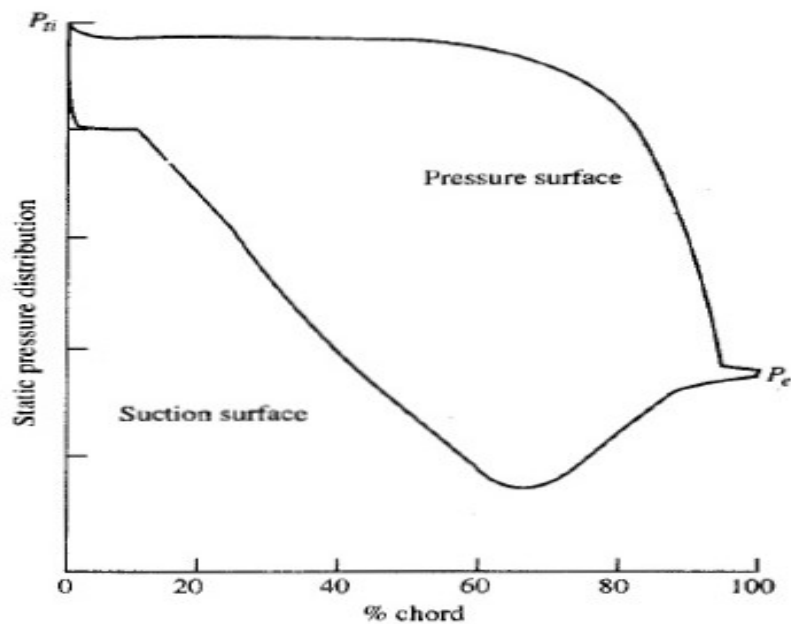


Figure 6.2.3: Static pressure distribution around a turbine blade [Mattingly, 1996].

A more detailed description of the effects of the boundary layer, as it travels through the suction side of the blade, can be found in the following Figure 6.2.4.



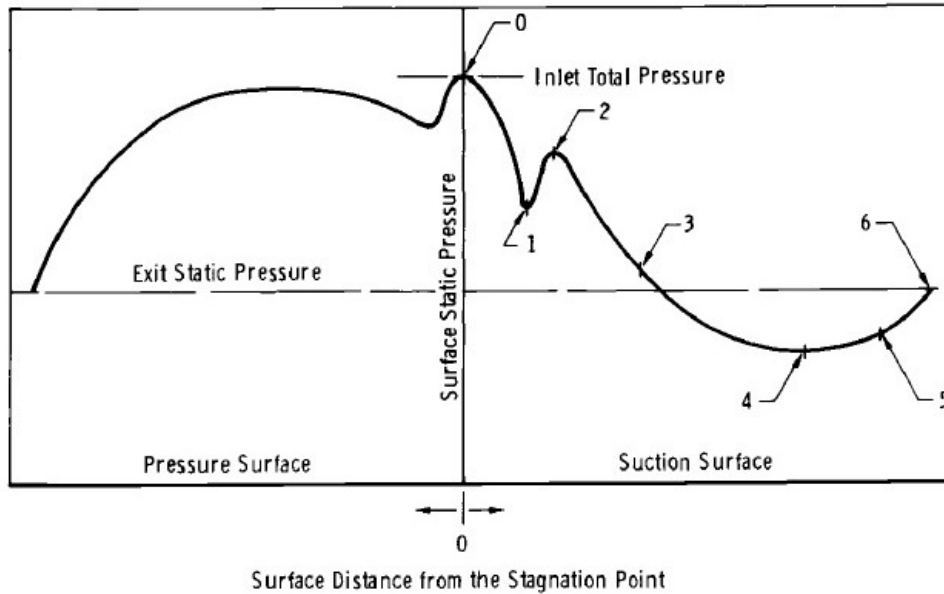


Figure 6.2.4: Detailed static pressure distribution [Oates, 1985].

As shown in the above figure, starting at stagnation point 0, the flow accelerates all throughout the leading edge circle, being laminar at the same time. A recompression occurs (which is depicted at points 1 to 2) and it is possible that a boundary layer separation will occur at point 1, due to the downstream adverse pressure gradient. After the separation a bubble forms that can reattach, now being fully turbulent. Now, the boundary layer accelerates strongly at point 2 and a re-laminarization is possible at point 3. Acceleration continues up until absolute minimum point 4 is reached, and a final recompression occurs. After point 4 there might be a similar separation of the boundary layer, forming a bubble that may or may not reattach fully turbulent. If the boundary layer reattaches, it will reach the trailing edge at point 6 or it might undergo turbulent separation at point 5 without reattachment [Oates, 1985]. The same phases can be seen on the resulting pressure distribution (Fig. 6.2.1), especially on the second stage stator.

Also, the corresponding temperature distribution around the blading surfaces was calculated (Fig. 6.2.5).



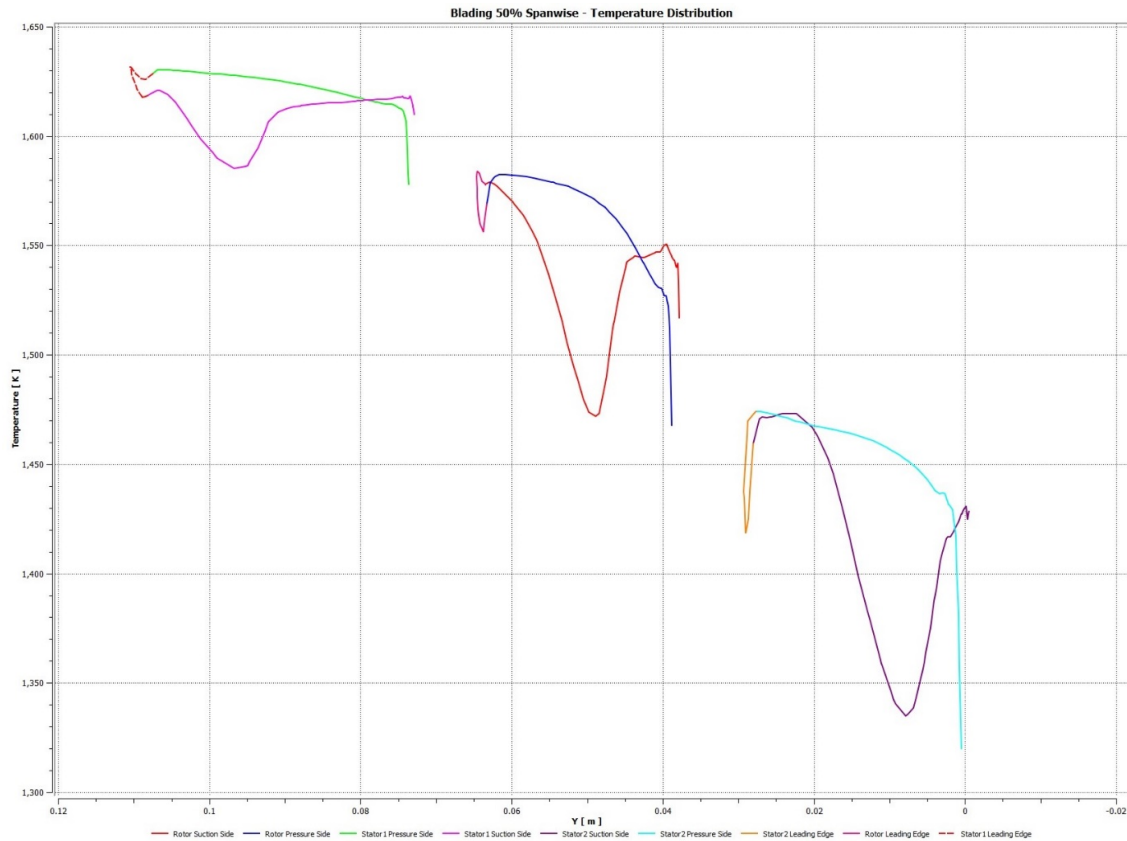


Figure 6.2.5: Blading 50% span-wise - static temperature distribution.

The exit static pressure distributions were also calculated (Fig. 6.2.6).

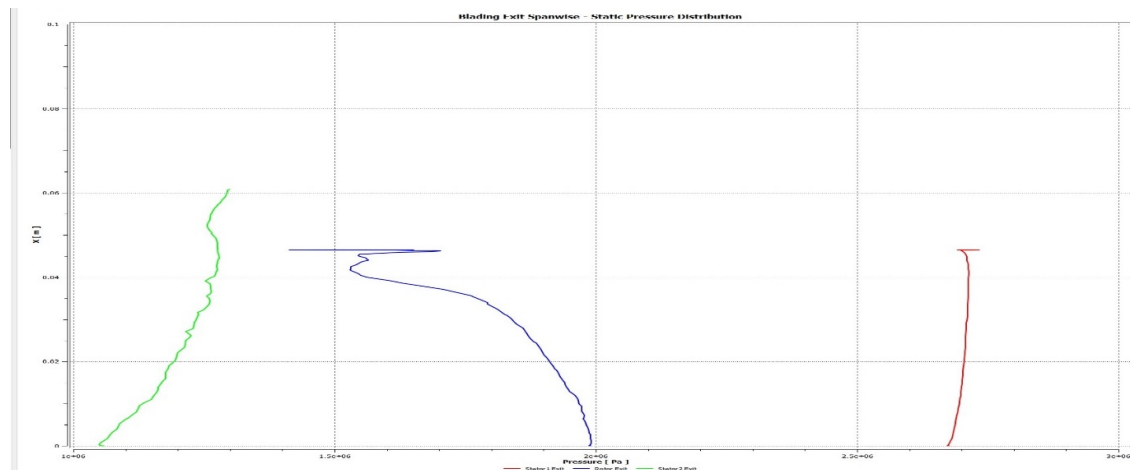


Figure 6.2.6: Blading exit; spanwise static pressure distribution.

It can be clearly seen, that at the rotor's exit occurs a significant static pressure loss, not in accordance to its neighboring stators. This phenomenon is caused by the tip clearance losses, i.e. the losses due to the gap between the rotor tip and the turbine shroud. The pressure gradient across the blade causes flow leakage through the clearance space, leading to pressure drop, turbulence and interference with the main flow [Boyce, 2002]. Due to the

leakage of the flow in the meridional direction at the blades' tip, a vortex is also being generated, detectable either by a pressure contour at the rotor's exit (the interface between the rotor and the second stage stator domain) or at the local velocity vector field. In general, vortices of the sort are due to the secondary vorticity vector, which itself is being produced by the turning of the vorticity vector, by the cascade [Dixon, 1998]. The figure below depicts a general outline of secondary flows within the blade passage [Moustapha, 2003].

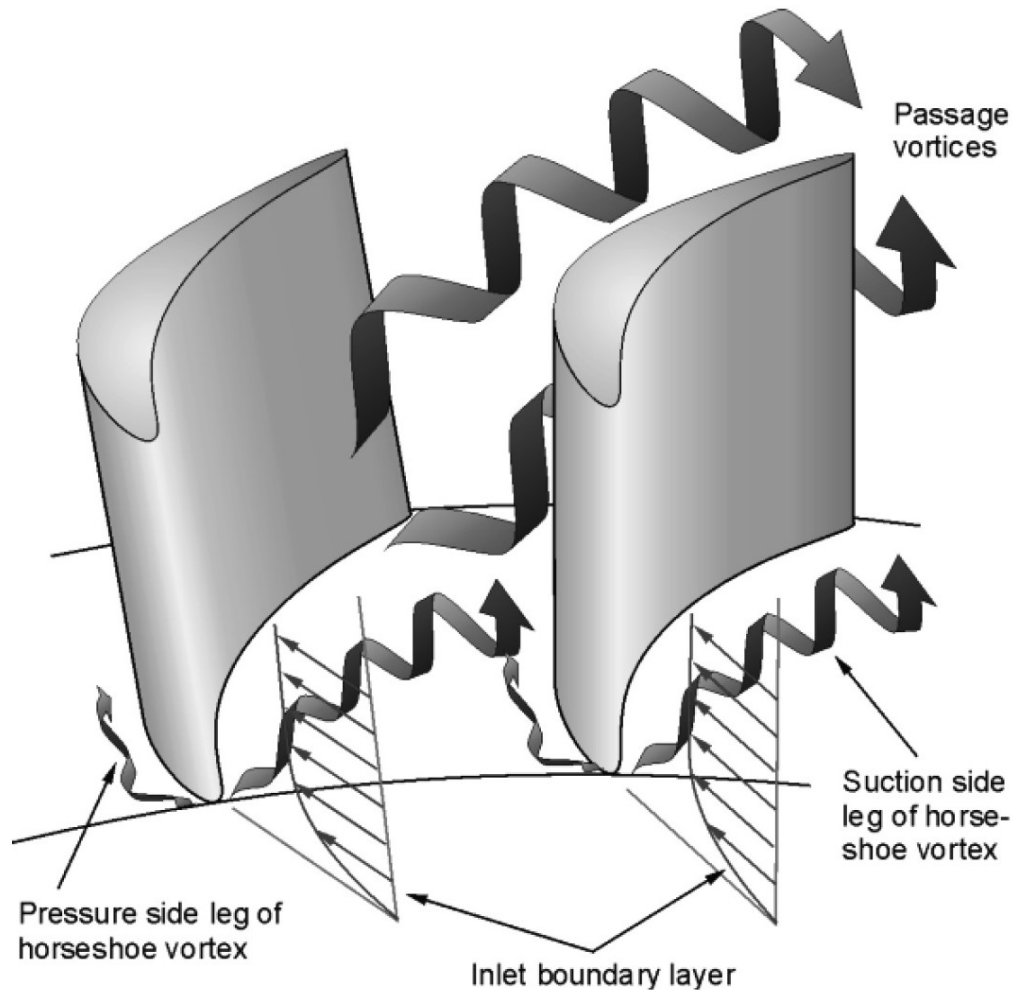


Figure 6.2.7: Outline of secondary flows within the blade passage [Moustapha, 2003].

What follows the above conclusions, is a visualization of the tip clearance vortex itself. It can be seen clearly, both in the velocity vector field and in the pressure iso-contour at the exit of the rotor. Furthermore, the vortex due to the secondary flows at the base of the blade passage is also visible, yet due to insufficient mesh density, is not accurately represented.

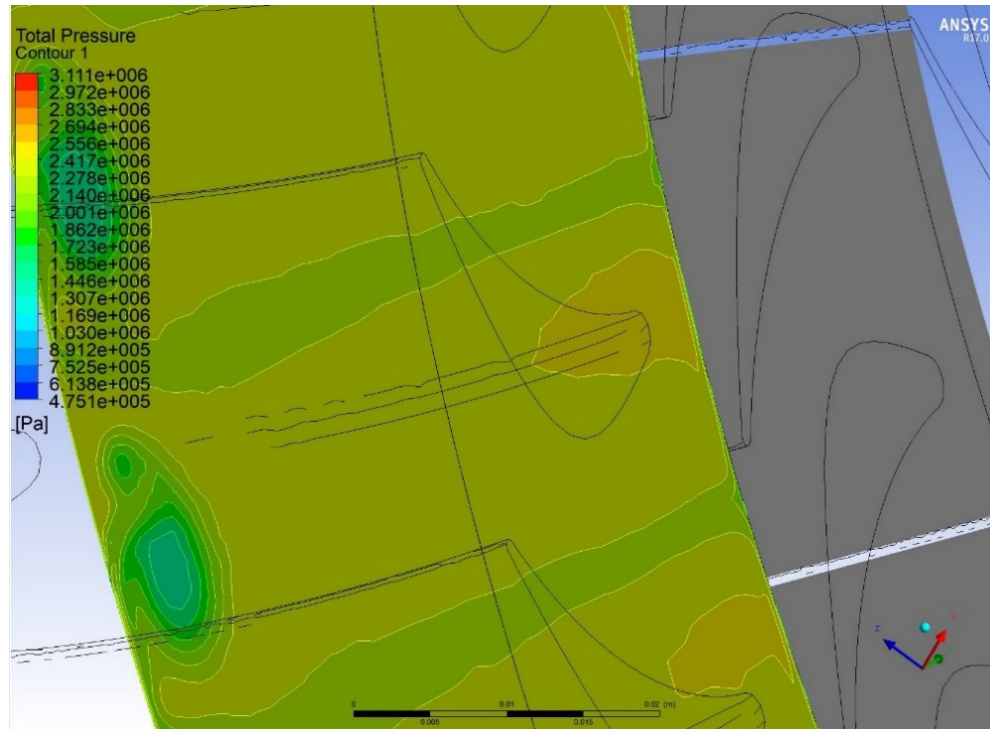


Figure 6.2.8: Total pressure iso-contours, depicting the tip clearance and secondary vortices.

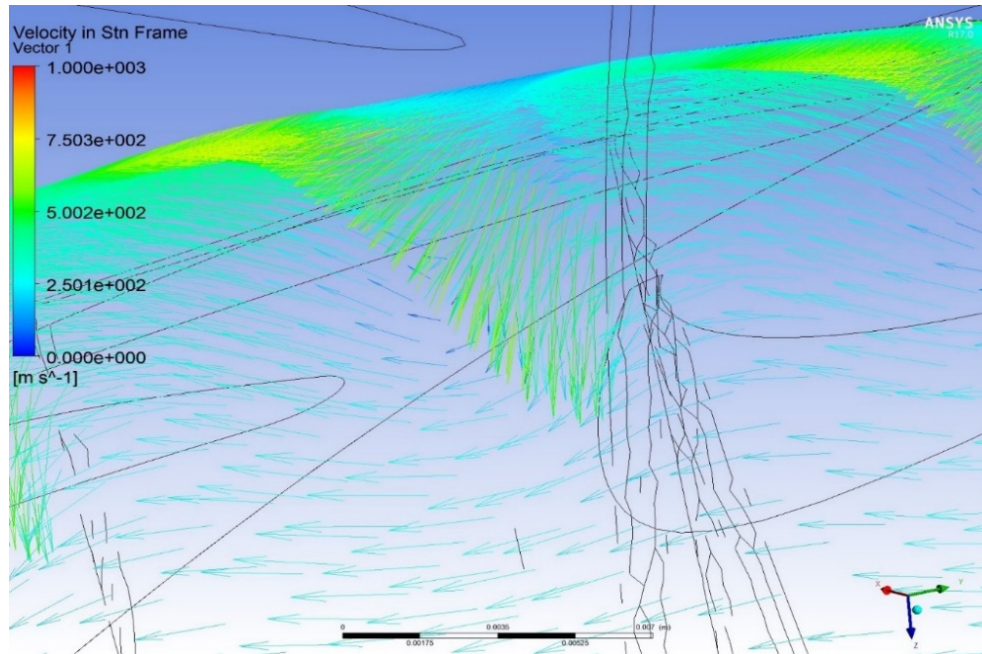


Figure 6.2.9: The tip clearance vortex, depicted in the form of a velocity vector field.

Finally, a Mach number, pressure and temperature (both static and total) distributions are depicted with the use of iso-contours on the mean radius plane created earlier. They are as follows.

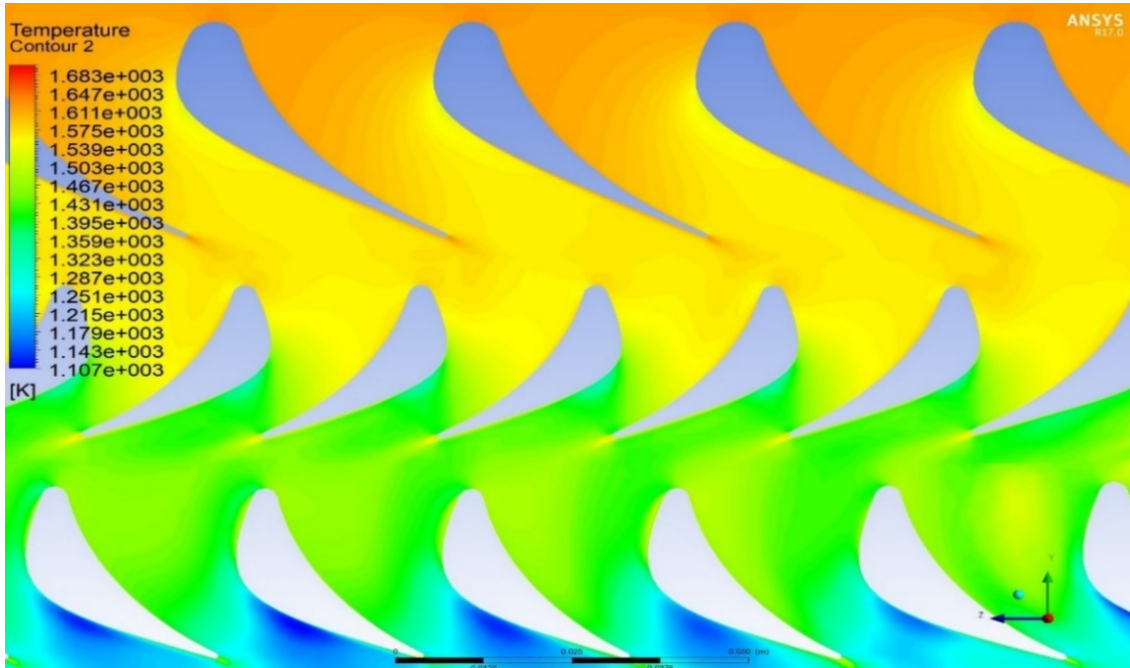


Figure 6.2.10: Temperature distribution in the mean radius level.

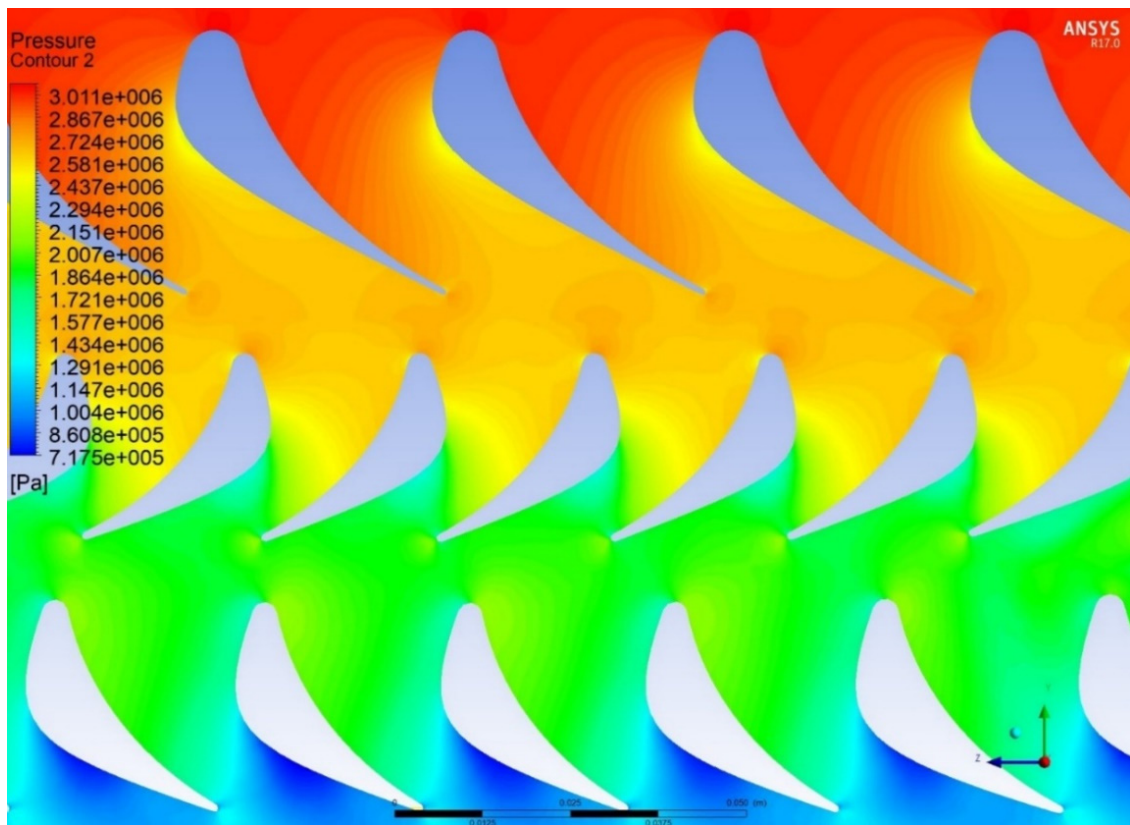


Figure 6.2.11: Pressure distribution in the mean radius level.



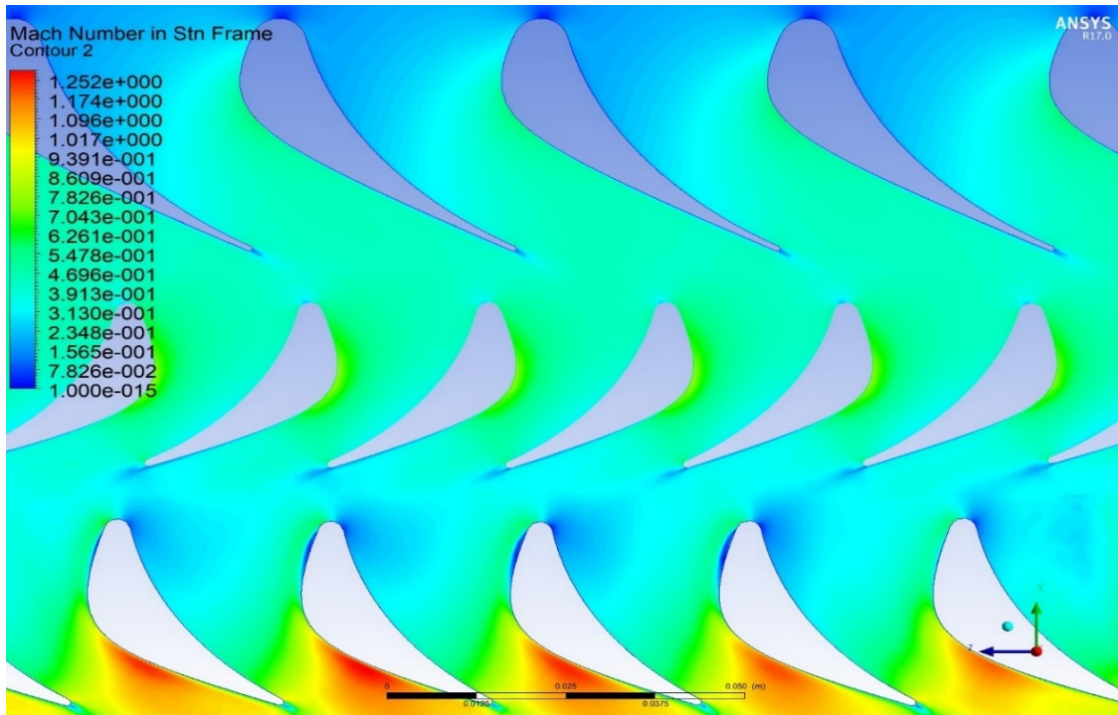


Figure 6.2.12: Mach number distribution in mean radius level.

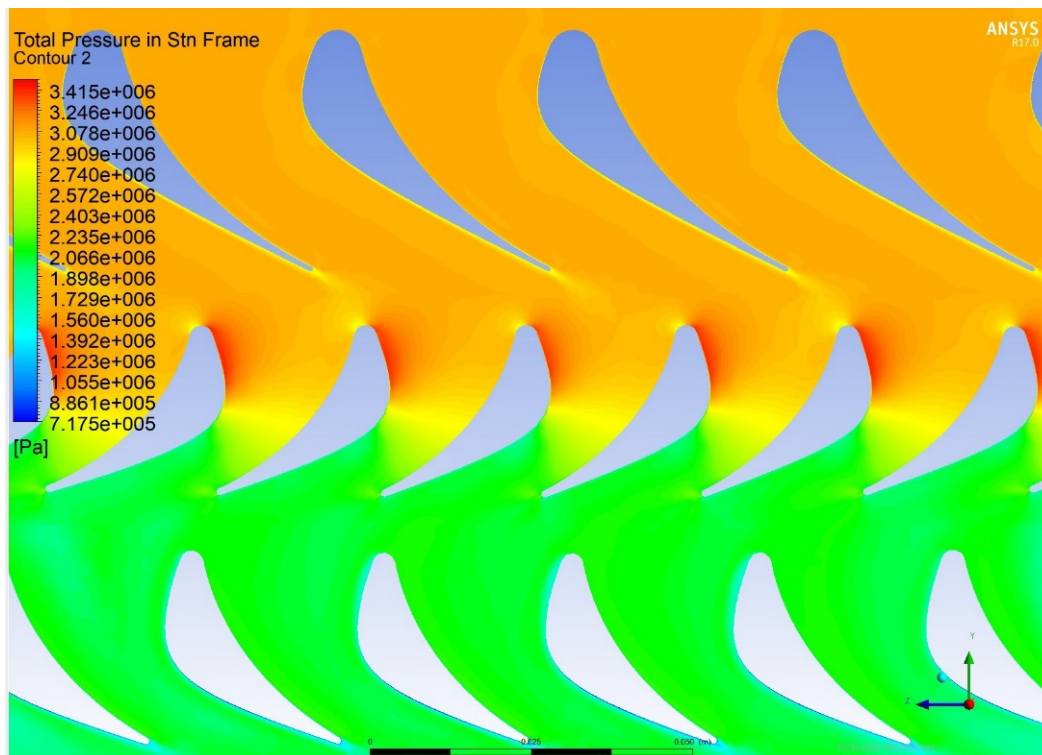


Figure 6.2.13: Total pressure in the mean radius level.

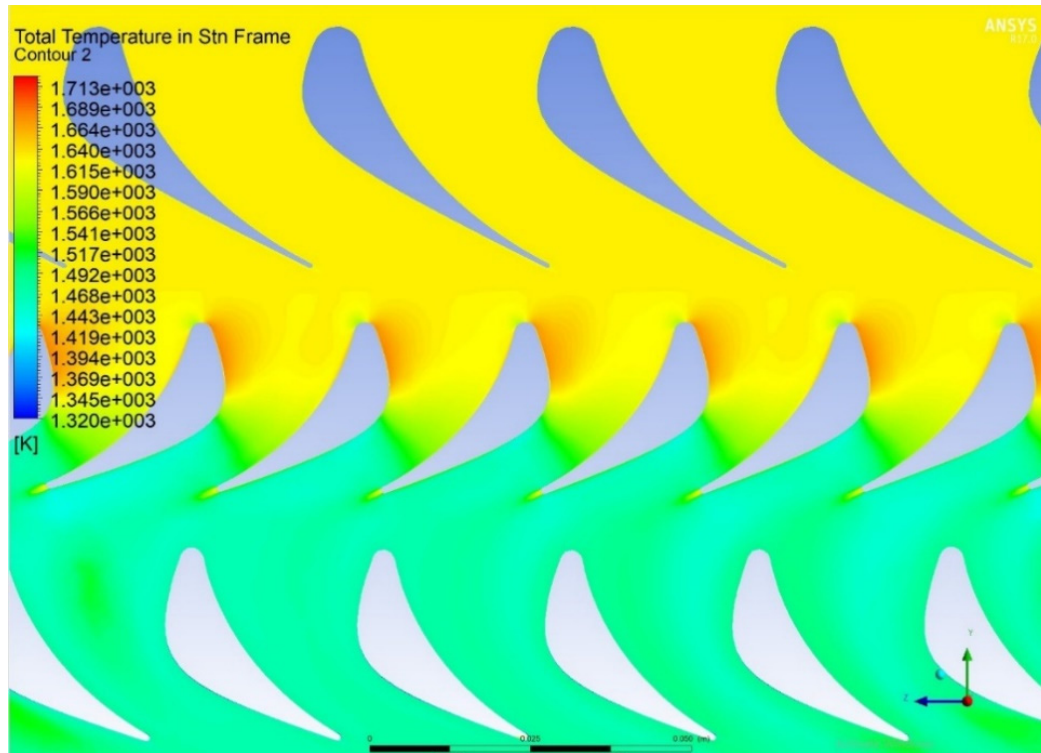


Figure 6.2.14: Total temperature in the mean radius level.

It can clearly be seen that the static temperature and pressure are declining in the axial direction, in accordance to the expected behavior of a fluid traveling through an axial turbine. More precisely, a certain amount of static pressure drop is achieved through the nozzle. The flow then passes through the rotor, where all the stagnation and static properties change [Lakshminarayana, 1996]. The total quantities still follow a decline, yet are preserved almost constant throughout the nozzles, since no energy is being added to the flow (although the friction losses decrease total pressure). The following Figure 6.2.15 demonstrates the change in static and total properties throughout a typical one and a half stage turbine, like the one studied in this work.

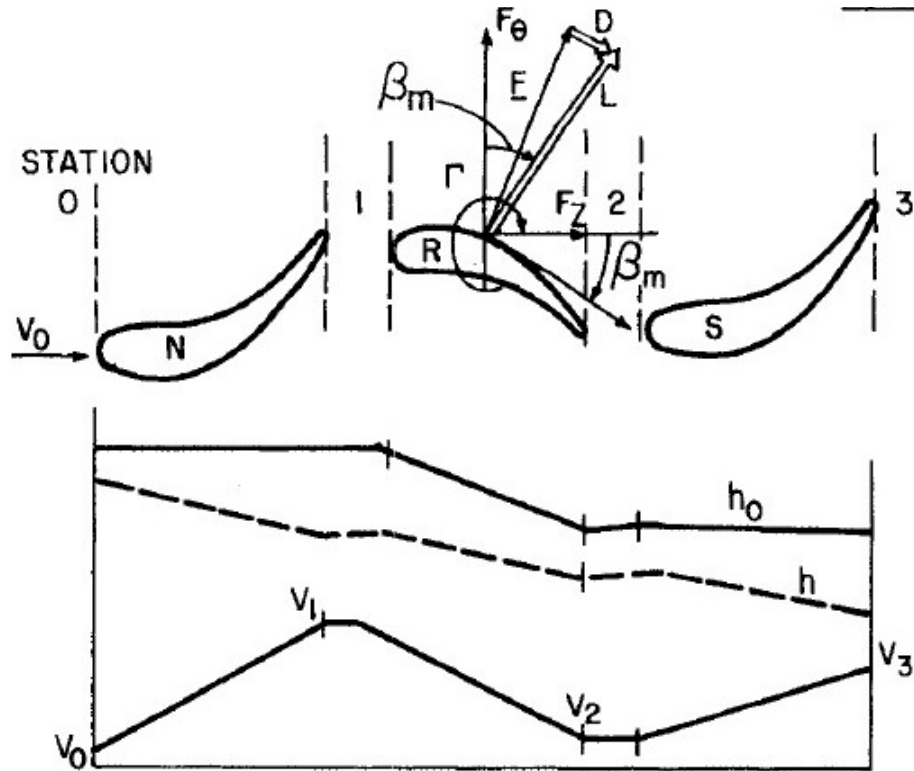


Figure 6.2.15 Total and static parameters variation in a one and a half stage turbine [Lakshminarayana, 1996].

The static and total temperatures and pressures follow the same scheme as the total and static enthalpy, depicted in the figure above [Lakshminarayana, 1996]. It can be seen that both total and static parameters are in accordance with the figure above.

Finally (Fig. 6.2.16), a comparison of the static pressure distribution is presented with results found in [Triantafyllou, 2010].



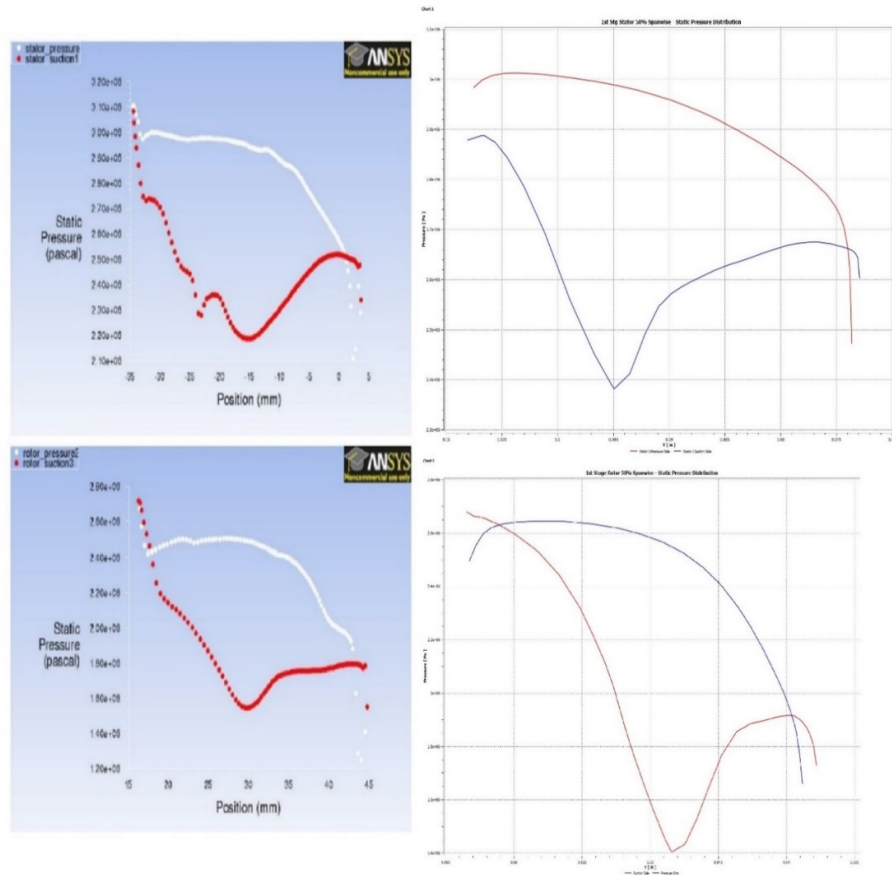


Figure 6.2.16: Static pressure distribution at 50% span-wise; comparison for the 1st stg stator (up) and the 1st stg rotor (down) [Triantafyllou, 2010].

### 6.3 Performance Parameters Calculation

First, it should be mentioned that notation has changed from denoting component inlet and outlet, to stage station notation.

There are several dimensionless parameters that can help evaluate the efficiency and the performance of an axial turbine. The basic parameters were listed in previous sections and are: the degree of reaction, the work coefficient, the flow coefficient, the isentropic efficiency and the velocity ratio. It should be noted that the calculations held herein, concern the 1<sup>st</sup> stage (stator and rotor), since usually such parameters are used to characterize turbine stages and not rotor or stator assemblies separately.

The degree of reaction of a stage shows the contribution of the rotor in the stage's total enthalpy drop, or in other words the fraction of stage expansion that occurs in the rotor [Cohen *et al.*, 1996]. Axial turbines can vary from 0% degree of reaction (impulse turbine) to 100% degree of reaction. Impulse turbines have none of their enthalpy drop in the rotor, and can be easily identified from their blades' geometry and the symmetry it characterizes them. Also, 50% reaction turbines have half of their enthalpy drop done in the rotor (and subsequently, the other half is being done in the stator) and have a distinct symmetry between their rotor blades and stator vanes, whilst the velocity triangles are symmetrical.

The degree of reaction can be calculated using the following [Person, 2015]

$$\Lambda = \frac{h_2 - h_3}{h_1 - h_3} \quad (6.3.1)$$

The subscript 1 implies the stage inlet, the subscript 2 implies the station between the stator and the rotor and the subscript 3 implies the stage outlet. To calculate the static enthalpies needed in Eq. 6.3.1 the "Function Calculator" feature in CFX-Post should be used. The "Function" is set to "ave" meaning average, since the average static enthalpy will be calculated for the: inlet to stator1 interface, stator1 to rotor interface, and rotor to stator2 interface. The static enthalpies in each of the above interfaces have been computed as

$$h_1 = 1.33304 \cdot 10^6 \frac{\text{J}}{\text{kg}},$$

$$h_2 = 1.28703 \cdot 10^6 \frac{\text{J}}{\text{kg}},$$

$$h_3 = 1.16463 \cdot 10^6 \frac{\text{J}}{\text{kg}}.$$

Applying the above values to Eq. 6.3.1, yields the following reaction degree

$$\Lambda \cong 0.72.$$

This means that a substantial expansion is being done in the stage's rotor. The above value is well within the normal range of degrees of reaction for modern turbines.

Following, is the calculation of the stage loading coefficient. The stage loading coefficient expresses the work capacity of the stage and is often called temperature drop coefficient [Cohen *et al.*, 1996]. It can be calculated using the following formula:

$$\psi = \frac{C_p \Delta T_o^{stage}}{U^2} \quad (6.3.2)$$

To calculate the stage total temperature drop, the same procedure should be followed: calculation of the average total temperature of the stages inlet (inlet domain to stator1 domain interface) and outlet (stator1 domain to rotor domain interface). The corresponding values are the following:

$$T_{o1} = 1631.67 \text{ K},$$

$$T_{o3} = 1465.99 \text{ K}.$$

The blade speed ( $U$ ) should also be defined. As stated earlier, the plane upon which the calculations are being conducted is the mean radius plane. Thus, the blade height is known. The rotational speed of the rotor was set during the simulation's setup and is equal to 13000rpm or 1361.3 rad/sec. Blade speed is calculated from the following:

$$U = \omega R, \quad (6.3.3)$$

$$U_{mean} = \omega R_{mean} = 359.4 \frac{m}{sec}. \quad (6.3.4)$$

Using the above values on Eq. 6.3.2, we get the following:

$$\psi = 1.57.$$

The above value is considered to be well within the normal range for modern turbines, since said range is approximately 1.3-2.2 [Mattingly, 1996]. At this point, it is worth noting that the stage loading coefficient can sometimes be expressed as follows

$$\psi_{NGTE} = \frac{C_p \Delta T_o^{stage}}{(1/2)U^2}. \quad (6.3.5)$$

Thus

$$\psi_{NGTE} = 2\psi. \quad (6.3.6)$$

The above expression of the loading coefficient is used by the United Kingdom's National Gas Turbine Establishment (NGTE) [El-Sayed, 2017]. In this Thesis the former is used.

The next dimensionless coefficient to be calculated is the flow coefficient. The flow coefficient is the ratio:

$$\varphi = \frac{C_a}{U} \quad (6.3.7)$$

In order to calculate it, a usual convention should first be made, that is the axial velocity throughout the stage remains constant [Dixon, 1998]

$$C_{a3} = C_{a2} = C_a = cst. \quad (6.3.8)$$

Then, a measurement of the absolute velocity should be taken at the exit of the first stage stator. The following figure shows the above:

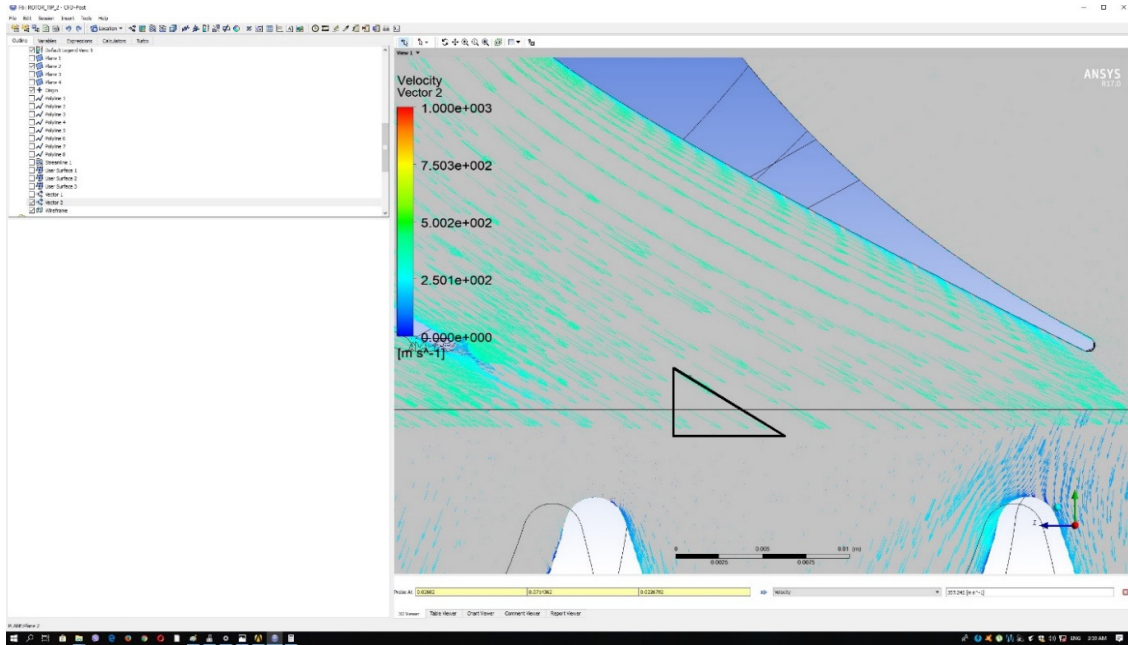


Figure 6.3.1: Absolute velocity at the stator's exit.

The absolute velocity at the stators exit was computed as

$$C_2 = 362 \frac{m}{sec}.$$

Then the orientation of the vector was calculated and found to be approximately  $57^\circ$ , measuring from the axial direction.

Having the above data, the axial velocity component can be calculated as

$$C_{a3} = C_{a2} = C_a = \cos\beta_2 C_2 = 197 \frac{m}{sec}.$$

Thus Eq. 6.3.7 yields the following:

$$\varphi \cong 0.55.$$

Again the flow coefficient's value is considered to be within the normal range of flow coefficients, that being 0.5-1.1 [Mattingly, 1996].

After the calculation of the degree of reaction, the stage loading coefficient and the flow coefficient, the total efficiency of the stage can be derived using Smith's charts [Smith, 1966]. The following Figure 6.3.2 depicts a Smith chart for several stage reaction degrees [Dick, 2015)].

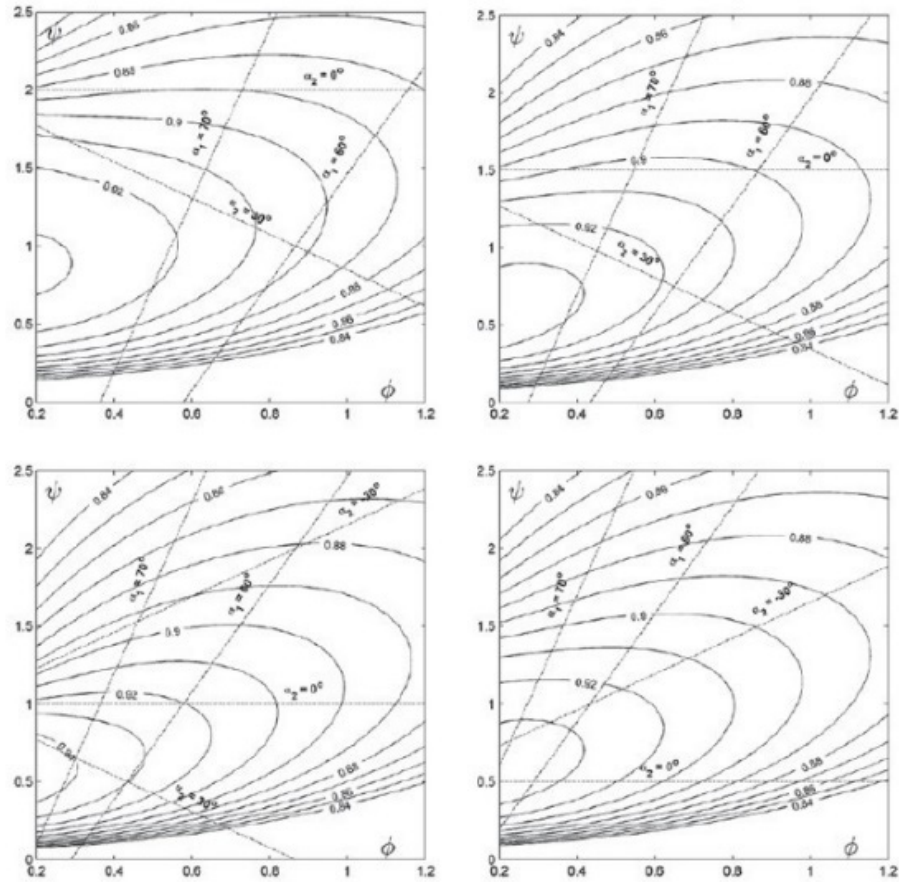


Figure 6.3.2: Smith charts for 0, 0.25, 0.5, 0.75 reaction [Dick, 2015].

Using the bottom right chart (0.75 reaction) in Fig 6.3.2, being the closest to the simulated turbine's stage reaction, we conclude that the efficiency of the turbine stage is:

$$\eta \cong 0.9$$

Again, the above value is within the efficiency limits for modern turbine stages, them being 0.89-0.94 [El-Sayed, 2017].

The velocity ratio can also be calculated. The velocity ratio is usually used by turbine designers in conjunction with the stage loading coefficient and is given by the following formula [Mattingly, 1996]:

$$VR = \frac{1}{\sqrt{2\psi}} \quad (6.3.9)$$

Knowing the stage loading coefficient from before, the velocity ratio for the stage is:

$$VR = 0.564$$

The normal values of a modern stage velocity ratio are ranging from 0.5-0.6 [Mattingly, 1996]. This implies that the simulated stage's velocity ratio is within the normal range.

Finally, the isentropic efficiency of the stage will be tackled. The isentropic efficiency can be given from the following formula [Cohen et al., 1996]

$$\eta_{is} = \frac{1 - \frac{T_{o3}}{T_{o1}}}{1 - \left(\frac{P_{o3}}{P_{o1}}\right)^{\frac{\gamma-1}{\gamma}}} \quad (6.3.10)$$

Total temperature and pressure are calculated in CFX-Post in the same manner as the previous averaging calculations. The values are the following:

$$T_{o1} = 1631.26 \text{ K},$$

$$T_{o3} = 1521.54 \text{ K},$$

$$P_{o1} = 3.07762 \cdot 10^6 \text{ Pa},$$

$$P_{o3} = 2.14223 \cdot 10^6 \text{ Pa}.$$

Using Eq. 6.3.10 yields

$$\eta_{is} \cong 0.82.$$

The value is close to what was used earlier in the boundary conditions calculation section, which was 0.85.

Finally, the static temperature drop in the stage was calculated, again by averaging the temperatures at the stages inlet and outlet and was found to be:

$$\Delta T_{stage} = 167.67 \text{ K}.$$

According to the literature, aero engines usually have a stage temperature drop in the range of 140 – 200 K [El-Sayed, 2017].

## 6.4 Stage Losses Calculation

Following, are the calculations for the stage losses, based on the Ainley-Mathieson data model [Ainley et al., 1951]. Said model produces two loss coefficients for the rotor and the stator. These coefficients have to include the following, in order to give a complete depiction of the stage losses at the rotor and the stator:

- Profile losses, associated with boundary layer growth around the blade profile, including separation losses due to adverse conditions generated by extreme angles of incidence, or high inlet Mach numbers.
- Annulus losses, caused by the boundary layer growth on the walls of the annulus (i.e. the hub and shroud inner walls).
- Secondary flow losses, which rise whenever a boundary layer is turned due to the existence of a nearby curved surface.
- Tip clearance losses, that occur because near the rotor blade tip the flow does not follow the intended path, thus not contributing its quota to total work output and at the same time interacting with the endwall boundary layer and the main flow.

In the Ainley-Mathieson model the above four contributors are condensed into three loss coefficients:

$Y_p$ , representing the total losses due to the blading's profile.

$Y_s$ , representing secondary and annulus losses.

$Y_k$ , representing tip clearance losses. This coefficient usually refers to rotor blades, since, in their majority, stator vanes are shrouded.

The secondary/annulus loss coefficients are being calculated as a sum since it can be quite difficult to distinguish the two, while the profile loss coefficient is calculated separately. At the end, all the coefficients are summed and the loss coefficient is calculated [Cohen et al., 1996].

First the stage's stator loss coefficient will be calculated. For the profile loss coefficient, the Ainley-Mathieson model uses an interpolation formula, based on cascade data from tests on nozzle blade profiles, and impulse blade profiles. If a blade profile is in between the two the interpolation formula is being used alongside the graphed cascade test data. The interpolation formula goes as follows:

$$Y_p = \{Y_{p(\beta_2=0)} + \left(\frac{\beta_2}{\beta_3}\right)^2 [Y_{p(\beta_2=\beta_3)} - Y_{p(\beta_2=0)}]\} \left(\frac{t/c}{0.2}\right)^{\beta_2/\beta_3} \quad (6.4.1)$$

The  $Y_{p(\beta_2=0)}$ ,  $Y_{p(\beta_2=\beta_3)}$  coefficients correspond to the profile loss coefficients of nozzle and impulse blading respectively. The angles refer to inlet and outlet gas angles. The above notation is used for the rotor. In the stator's case all that is needed to be done is to switch said angles.

The following figures provide the means of evaluating  $Y_{p(\beta_2=0)}$ ,  $Y_{p(\beta_2=\beta_3)}$  as a function of the solidity of the blading [Cohen et al., 1996].



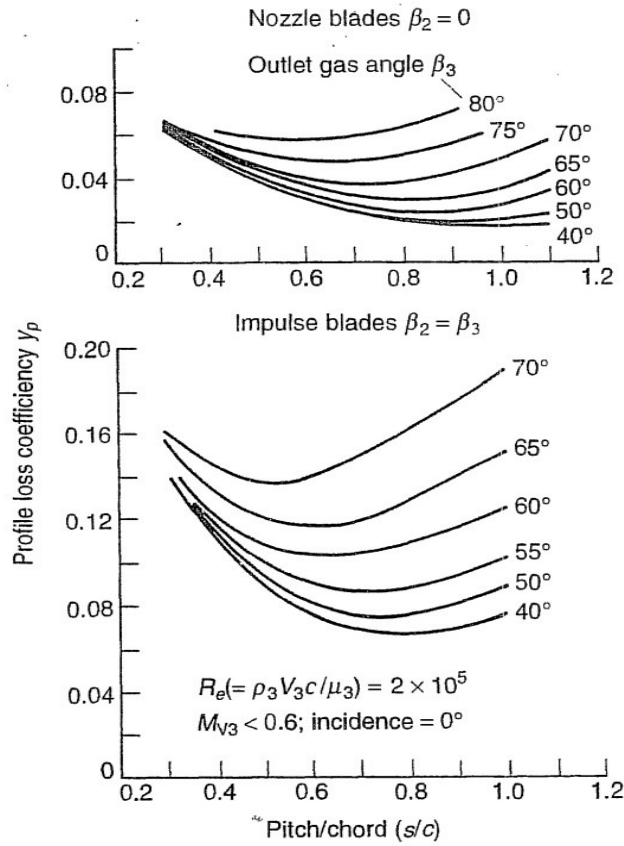


Figure 6.4.1: Profile loss coefficients for nozzle and impulse blading [Cohen et al., 1996].

In case that the blading at hand is neither impulse nor nozzle type, then Fig. 6.4.1 is utilized along with Eq. 6.4.1. In case that the blading at hand falls in either of the above categories, the profile loss coefficient can be directly evaluated from the charts.

As can be seen from Eq. 6.4.1 the stators solidity, the inlet and outlet angles, and the maximum thickness to chord ratio are needed for the calculation of the profile loss coefficient. Said interpolation is valid for thickness to chord ratios of up to 0.25. Below are the stator's and rotor's physical characteristics:

$$(t/c)_R \cong 0.25,$$

$$(t/c)_{s1} \cong 0.23,$$

$$(t/c)_{s2} \cong 0.26,$$

$$(s/c)_R \cong 0.64,$$

$$(s/c)_{s1} \cong 0.66,$$

$$(s/c)_{s2} \cong 0.65.$$

To take the above measurements, the initial model in CATIA V5R20 was utilized, using the "Measure" feature of the software.

The outlet gas angle of the first stage stator was previously calculated and found to be  $57^\circ$ . As extra measure, the following formulas will be used, expressing the inlet and outlet angles as a function of stage loading, degree of reaction and flow coefficient [Cohen *et al.*, 1996]:

$$\tan\beta_3 = \frac{1}{2\varphi} \left( \frac{1}{2}\psi + 2\Lambda \right) \quad (6.4.2)$$

$$\tan\beta_2 = \frac{1}{2\varphi} \left( \frac{1}{2}\psi - 2\Lambda \right) \quad (6.4.3)$$

$$\tan\alpha_3 = \tan\beta_3 - \frac{1}{\varphi} \quad (6.4.5)$$

$$\tan\alpha_2 = \tan\beta_2 + \frac{1}{\varphi}. \quad (6.4.6)$$

Plugging the reaction, stage loading, and flow coefficient values in the above equations, we get the following

$$\begin{aligned} \beta_3 &= 52.6^\circ, \\ \beta_2 &= -21.05^\circ, \\ \alpha_2 &= 57^\circ. \end{aligned}$$

Judging from the CFX-Post results, as well as the boundary conditions set earlier, we assume that

$$\alpha_1 = 0^\circ.$$

Since the inlet gas angle for the first stage stator is 0, the chart on Fig. 6.4.1 can be directly utilized, thus

$$Y_{ps1} \cong 0.03.$$

To evaluate the sum of the secondary/annulus and tip clearance loss coefficient, the following formula should be used

$$Y_s + Y_k = \left[ \lambda + B \left( \frac{k}{h} \right) \right] \left[ \frac{C_L}{s/c} \right]^2 \left[ \frac{\cos^2 \beta_3}{\cos^3 \beta_m} \right]. \quad (6.4.7)$$

Again, rotor notation is being used in Eq. 6.4.7. For the nozzle,  $\alpha_2$  and  $\alpha_1$  are used.

The  $B$  coefficient refers mainly to tip clearance losses. and since the vanes are shrouded, such losses can be assumed to be non-existent. Thus,  $B = 0$ .

The  $\lambda$  coefficient can be extracted from the following chart (Fig. 6.4.2) [Cohen *et al.*, 1996].

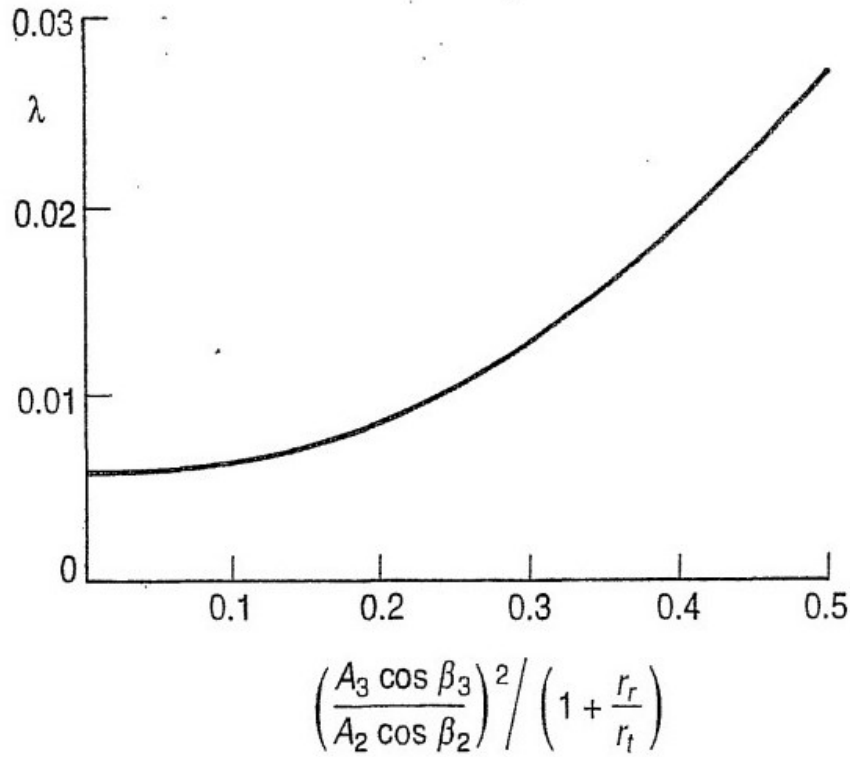


Figure 6.4.2:  $\lambda$  coefficient function [Cohen et al., 1996].

From the above chart it can be deduced that  $\lambda$  is dependent on the root-to-tip radius ratio, as well as flow acceleration, which is represented by the normal to the flow area at inlet and outlet [Cohen et al., 1996]. This means that first the quantity represented in the  $x$ -axis of the above chart should be calculated.

The area ratio was computed with the aid of CFX-Post's area function calculator, the inlet and outlet angles of the first stage stator are known and the root radius is also known. For the tip ratio the mean value was calculated. Thus, the  $x$ -axis quantity was calculated to be 0.345. This gives us a  $\lambda$  coefficient of approximately equal to 0.015.

Next the  $C_L$  quantity needs to be determined as

$$C_L = 2 \frac{s}{c} [(\tan \beta_3 + \tan \beta_2) \cos(\beta_m)], \quad (6.4.8)$$

$$\beta_m = \arctan \left[ \frac{\tan \beta_3 - \tan \beta_2}{2} \right]. \quad (6.4.9)$$

Dealing with  $\beta_m$  first we get

$$\beta_m = 37.5^\circ.$$

This allows to use Eq. 6.4.8 in order to calculate the lift coefficient as

$$C_L = 1.611.$$

Now all quantities are available and Eq. 6.4.7 can be utilized

$$Y_s + Y_k = 0.0476.$$

Thus, the loss coefficient for the stator is as follows

$$Y_{s1} = (Y_s + Y_k)_{s1} + Y_{ps1} = 0.0476 + 0.03 = 0.0776.$$

At this point it should be mentioned that the above procedure is reliable for blading with trailing edge thickness to chord ratio of 0.02. In case the blades deviate from this value, a correction factor is applied to the overall pressure loss coefficient.

Using again CATIA V5R20 to conduct the measurements we conclude that:

$$\left(\frac{t_{TE}}{c}\right)_{s1} = 0.012.$$

The stator vane differs from the normal value of 0.02. The following chart (Fig 6.4.3) gives the correction factor that should be applied.

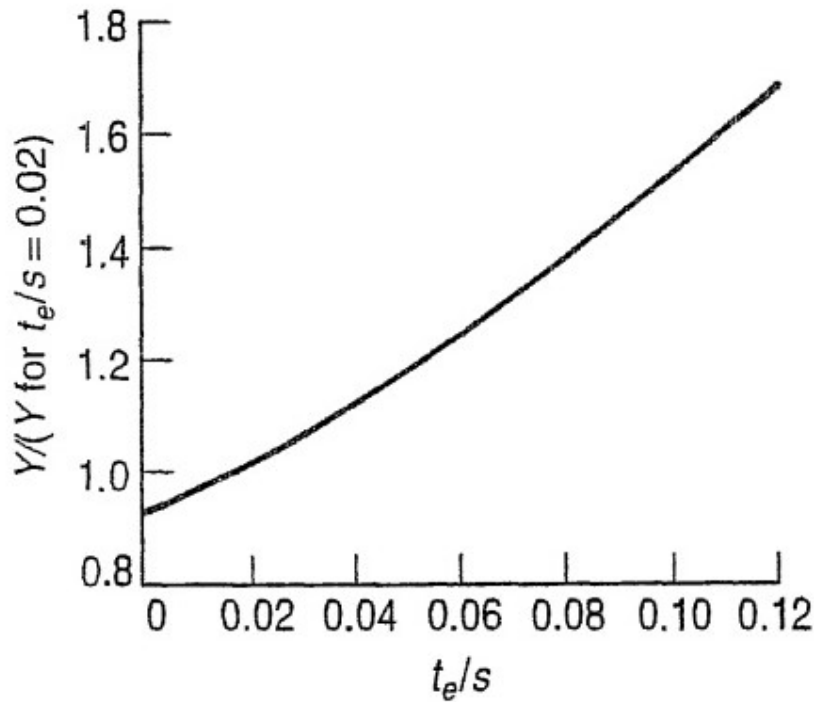


Figure 6.4.3: Correction factor for blades for varying TE thickness to chord ratio [Cohen et al., 1996].

Using the value calculated, we get a correction factor=0.95. Thus,

$$Y_{s1corrected} = 0.07372.$$

For the rotor, the same procedure applies. Since the rotor case does not fall within the nozzle blade or the impulse blade category, Eq. 6.4.1 should be utilized. The solidity of the rotor, as well as the gas outlet angle, have already been calculated. Using the above two, the  $Y_{p(\beta_2=\beta_3)}$  and  $Y_{p(\beta_2=0)}$  can be derived from Fig. 6.4.1 as

$$Y_{p(\beta_2=0)} = 0.03,$$

$$Y_{p(\beta_2=\beta_3)} = 0.09.$$

Plugging these values into Eq. 6.4.1 yields the following

$$Y_{pr} = 0.043.$$

Now, the secondary/annulus and tip clearance loss coefficients are to be calculated. This time the  $B$  constant is non-zero, since the rotor has a tip clearance. The  $B$  constant is 0.5 for blades with radial tip clearance and 0.25 with shrouded blades with side clearance [Cohen et al., 1996]. The figure below (Fig. 6.4.4) depicts the above.

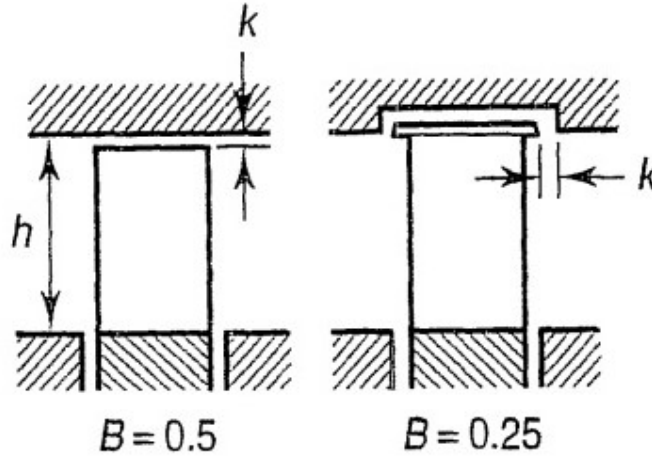


Figure 6.4.4:  $B$  coefficient variation [Cohen et al., 1996].

In our case, the rotor has a radial tip clearance, thus  $B = 0.5$ . The rest of the quantities in Eq. 6.4.7 are evaluated in the same way as for the stator, thus

$$C_L = 0.901,$$

$$\lambda = 0.01.$$

Then, the sum of the secondary/annulus – tip clearance losses can be calculated as

$$(Y_s + Y_k)_r = 0.0435.$$

This means that the overall pressure loss coefficient in the rotor is

$$Y_r = (Y_s + Y_k)_r + Y_{pr} = 0.0865.$$

Correcting the above for 0.0285 TE thickness-to-chord ratio, we get

$$Y_{r\text{corrected}} = 0.095.$$

This means that the total losses in the stage are equal to

$$Y_{\text{stage}} = 0.16872.$$

The following Figure 6.4.5 encompasses all the loss mechanisms in a stage, as well as their respective values.

<b>Turbine Loss Values in the Overall Stage</b>	
<b>Loss Mechanics</b>	<b>Loss (%)</b>
Profile	2–4
Endwall	1 1/2–4
Secondary flow	1–2
Rotor incidence	1–3
Tip clearance	1 1/2–3
Wheel disc	1–2

Figure 6.4.5: Stage losses [Boyce, 2002].

From the figure above, we conclude that the overall losses (not including the wheel disc; rotor incidence is included in profile losses [Cohen *et al.*, 1996]) range from 8% to 16%. This puts our losses on the higher end of the spectrum, yet still very close to normal values. This is mainly because the turbine is working at off-design conditions; this should also be the reason of the large computed value of the reaction degree of the stage.

## 6.5 Conclusion, Further Work Motivation

Having tested the simulated results of the turbine's operation against the expected ranges of dimensionless parameters for modern turbines, we can conclude that said turbine falls well within the normal operating range, although it was simulated for an operating point which is not the design one.

This gives confidence in the exploitation of the model for further work. More specifically, the introduction of particles in the flow field can be used as a means of evaluating erosion phenomena that are bound to occur, due to contaminated fuel or ingested ambient air. This will allow for the estimation of erosion rates, based on simulation information such as impingement angle, particle diameter etc. [Finnie, 1960].

Furthermore, due to limited computational resources, specific model domains can be suppressed. This means that certain domains can be rigorously studied with the use of a much more dense mesh, yielding more accurate results.

## References

1. G.C. Oates, *Aerothermodynamics of aircraft engine components*, American Institute of Aeronautics and Astronautics, 1985.
2. E. Dick, *Fundamentals of Turbomachines, Fluid Mechanics and Its Applications*, Springer Netherlands, 2015.
3. A.F. El-Sayed, *Aircraft Propulsion and Gas Turbine Engines*, CRC Press, 2017.
4. D.J. Dusa, W. Tabakoff, "Analytical method for designing turbine nozzle partitions", *AIAA Journal of Aircraft*, 1(1), 1964.
5. R.H. Aungier, *Turbine aerodynamics: axial-flow and radial-inflow turbine design and analysis*, ASME Press, 2006.
6. J.D. Mattingly, *Elements of Gas Turbine Propulsion*, Mc-Graw-Hill, 1996.
7. H. Cohen, G.F.C. Rogers, H.I.H. Saravanamuttoo, *Gas turbine theory*, Addison Wesley Longman, 1996.
8. K. Hünecke, *Jet Engines Fundamentals of Theory, Design and Operation*, Zenith Press, 1997.
9. M.P. Boyce, *Gas Turbine Engineering Handbook*, ASME USA & IDGTE U.K., Gulf Professional Publishing, 2002.
10. Z. Zou, S. Wang, H. Liu, W. Zhang, *Axial Turbine Aerodynamics for Aero-Engines, Flow Analysis and Aerodynamics Design*, Springer, Singapore 2018.
11. G.N. Koini, S.S. Sarakinos, I.K. Nikolos, "A software tool for parametric design of turbomachinery blades", *Advances in Engineering Software*, 40(1), pp.41-51, 2009.
12. J. Person, *1D turbine design tool validation and loss model comparison: Performance prediction of a 1-stage turbine at different pressure ratios*, MSc Thesis, KTH, School of Industrial Engineering and Management, 2015.
13. I. Finnie, "Erosion of Surfaces by Solid Particles", *Wear*, 3(2), pp. 87-103, 1960.
14. S.F. Smith, "A Simple Correlation of Turbine Efficiency," *Journal of Royal Aeronautical Society*, 1965.
15. D.G. Ainley, G.C.R. Mathieson, *A Method of Performance Estimation of Axial-Flow Turbines*, Aeronautical Research Council, London, 1951.
16. ANSYS CFX-Solver Theory Guide.
17. B. Lakshminarayana, *Fluid Dynamics and Heat Transfer of Turbomachinery*, John Willey and Sons, 1996.
18. W. Wiberg & N. Anton, *Aerodynamic design of a gas turbine rotor blade for the KTH test turbine*, Lunds Universitet, 2013.
19. T. Triantafillou, *Computational Investigation of the Effect of Sand Particles Ingestion on a military High Pressure Axial Turbine*, MSc Thesis, Cranfield University, School of Engineering, 2010.



20. [www.quickmath.com](http://www.quickmath.com), 2018.
21. S.L. Dixon, *Fluid Mechanics, Thermodynamics of Turbomachinery*, Butterworth-Heinemann, 1998.
22. H. Moustapha, M.F. Zelesky, N.C. Baines, D. Japikse, *Axial and radial turbines*, Edwards Brothers Incorporated, Vermont, 2003.